DEGRADATION OF TBC SYSTEMS IN ENVIRONMENTS RELEVANT TO ADVANCED GAS TURBINES FOR IGCC SYSTEMS

by

Nathaniel Allan Bohna

BS, Pennsylvania State University, 2001

MS, Pennsylvania State University, 2003

Submitted to the Graduate Faculty of

the Swanson School of Engineering in partial fulfillment

of the requirements for the degree of

Doctor of Philosophy

University of Pittsburgh

2017

UNIVERSITY OF PITTSBURGH

SWANSON SCHOOL OF ENGINEERING

This dissertation was presented

by

Nathaniel Allan Bohna

It was defended on

March 14, 2017

and approved by

Gerald H. Meier, PhD, Professor
Department of Mechanical Engineering and Materials Science

Ian Nettleship, PhD, Associate Professor
Department of Mechanical Engineering and Materials Science

Lei Li, PhD, Assistant Professor
Department of Chemical and Petroleum Engineering

Dissertation Director: Brian Gleeson, PhD, Professor
Department of Mechanical Engineering and Materials Science

DEGRADATION OF TBC SYSTEMS IN ENVIRONMENTS RELEVANT TO ADVANCED GAS TURBINES FOR IGCC SYSTEMS

Nathaniel Allan Bohna, PhD

University of Pittsburgh, 2017

Plasma sprayed (PS) thermal barrier coatings (TBCs) are used to provide thermal insulation for the hottest components in gas turbines. Zirconia stabilized with 7wt% yttria (7YSZ) is the most common ceramic top coat used for turbine blades. The 7YSZ coating can be degraded by the buildup of fly-ash deposits which can arise from the fuel source (coal/biomass) used in the combustion process in gas turbines. Fly-ash from the integrated gasification combined cycle (IGCC) process can result from coal-based syngas and also from ambient air which passes through the system. TBCs are also exposed to harsh gas environments containing CO_2, SO_2, and steam. As presented in this thesis, degradation from the combined effects of fly-ash and harsh gas atmosphere can severely limit TBC lifetimes.

It is well established that degradation at very high temperatures (≥1250°C) from deposits consisting of the oxides CaO-MgO-Al_2O_3-SiO_2 results from extensive liquid silicate infiltration into the porous top coat of the YSZ. This infiltration causes early failure resulting from chemical and/or mechanical damage to the ceramic layer. Damage resulting from liquid infiltration, however, is not typically considered at relatively lower temperatures around 1100°C because liquid silicates would not be expected to form from the oxides in the deposit.

A key focus of this study is to assess the mode and extent of TBC degradation at 1100°C in cases when some amount of liquid forms owing to the presence of K_2SO_4 as a minor ash constituent. Two types of liquid infiltrations are observed depending on the principal oxide (i.e., CaO or SiO_2) in the deposit. The degradation is primarily the result of mechanical damage, which results from infiltration caused by the interaction of liquid K_2SO_4 with either the CaO or SiO_2. The TBCs used in this work are representative of commonly used coatings used in the hottest sections of land-based gas turbines. The specimens consist of 7YSZ top coats deposited on superalloy (Rene' N5 and PWA 1484) substrates that had been coated with NiCoCrAlY bond coats. Two different top coats are studied: conventional low-density 7YSZ, and also dense vertically cracked coatings.

The specific mechanisms of liquid infiltration resulting from CaO and SiO_2 are studied by conducting isothermal exposures followed by detailed characterizations. The resulting consequences on cyclic lifetimes are also determined. Further, the cyclic lifetimes are studied in several gas atmospheres to examine the combined effect of deposit and gas atmosphere on TBC lifetime.

This work identifies a TBC degradation mechanism which had previously not been considered. It will be clearly shown that deposit-induced attack of TBCs can be highly detrimental at an intermediate temperature like 1100°C.

TABLE OF CONTENTS

LIST OF TABLES

LIST OF FIGURES

PREFACE

I would like to thank my advisor, Professor Brian Gleeson, for his guidance and expertise. I am also grateful for the contributions of Professor Gerald Meier. I am thankful for all that I have learned from them and for their patience in helping me complete this work. I would like to also express my gratitude to the rest of my committee, Professor Ian Nettleship and Professor Lei Li, for the time which they dedicated to helping me complete this dissertation.

I owe a special thanks to Thomas Gheno for his mentorship and incredible level of dedication to this project. This work would not exist without his efforts. I also received tremendous support from other members of the group, especially Satia Soltanattar and Juan Manuel Alvarado Orozco.

The funding for this work was provided by NETL-UTSR. Praxair Surface Technologies (PST) was the industrial partner for this work. PST generously provided all the samples (both free-standing YSZ coatings as well as complete TBCSs) and also provided characterization data.

Among the many friends and colleagues who have supported me in my pursuit of a PhD, few have been more significant than Jim Crawford. One could not ask for a better teacher, friend, and colleague. But, more importantly, my parents have always been my most passionate supporters. I would not have accomplished this without their constant support and encouragement. I have relied heavily on their help and they have never let me down, and for that I am grateful.

1.0 INTRODUCTION

The large-scale use of coal in generating electricity has led to the development of technologies that can improve efficiency and cleanliness of using coal-derived fuels [1]. Even with those improvements, coal-derived power generation has declined [2, 3] over the past 5-10 years, at least in part as a result of stricter environmental regulations. The recent increase in shale gas extraction has facilitated a shift to natural gas fired power plants in the United States as an alternative to coal. However, the large coal reserves that still exist create an interest in using coal in a manner that can compete with natural gas in efficiency and pollution levels [4]. This has led to the development of Integrated Gasification Combined Cycle (IGCC) plants as an alternative use of coal for electricity production. These plants have the potential to operate with reduced emissions of particulates and CO_2 [5] compared to conventional coal-fired power plants.

Power generation using an IGCC process uses land-based gas turbines as the primary source of electricity generation. Since the inception of gas turbines, the need for higher efficiency has prompted a continuous increase of operating temperatures, eventually exceeding the capabilities of the metallic materials typically used as structural components. This has led to the development of thermal barrier coatings (TBCs) [6], which consist of a ceramic topcoat and a metal bondcoat applied to a single-crystal, nickel-base superalloy substrate. TBCs are used on

turbine components in the hottest sections, and these components are subjected to harsh atmospheres containing CO_2, SO_2, and steam at high temperatures. They can also be subjected to the buildup of deposits in the turbine.

The source of deposits in an IGCC process can be from the syngas, air-borne dust passing through the turbine, combustion by-products, or reaction of syngas with metallic components in the system[7]. Because of a large air:fuel ratio used in combustion, the bulk composition of fly-ash deposit is primarily influenced by the composition of atmospheric dust ingested through the turbine. Fly-ash deposits primarily consist of CaO, SiO_2, and Al_2O_3 [5, 7]. Some minor constituents (sulfates and sulfides) can also result from the syngas, which is commonly derived from coal, biomass, and/or petcoke [8]. These sulfur-containing species are typically present in fly ash as K_2SO_4 [9] and Na_2SO_4, from the initial fuel source, as well as FeS [7, 10] from reaction of syngas with metallic components in the system.

The oxide constituents of fly ash are similar to CaO-MgO-Al_2O_3-SiO_2 (CMAS) deposits which have been widely studied in aero-engine applications at temperatures ≥1250°C where significant liquid silicate infiltration causes TBC degradation and early failure. TBC components in land-based turbines, however, are exposed to relatively lower temperatures around 1100°C where detrimental effects of deposits on TBC components are not as well understood. The roles of minor constituents such as K_2SO_4 and FeS are also not well understood because they are typically not considered in deposit-induced failure studies of TBCs. The purpose of this thesis is to identify early failure mechanisms of TBCs as a result of fly-ash deposits including minor constituents K_2SO_4 and FeS. Deposit-induced degradation was also studied in harsh gas atmospheres containing CO_2, SO_2, and water vapor to identify any combined effects from deposits and gas atmospheres. This

thesis provides fundamental understanding of TBC failure as a result of fly-ash deposits in gas atmospheres relevant to IGCC systems.

This work is divided into two main parts: deposit-induced degradation of TBC topcoats, and effects of that degradation on TBC lifetimes. The degradation of the topcoat material was studied using isothermal exposures of zirconia stabilized with 7wt% yttria (7YSZ), which is the most commonly used material for the ceramic top coat in a TBC. Experimental results were used to identify specific deposit chemistries which can infiltrate the YSZ and change its mechanical properties. In the second part of the thesis, the detrimental effects of those deposits on TBC lifetime were examined through thermal cycling in various gas atmospheres. This thesis shows that deposits can damage TBCs and cause early failure at 1100°C, a temperature that is not typically considered relevant in deposit-induced early failure studies.

2.0 LITERATURE SURVEY

2.1 FOSSIL FUEL POWER GENERATION AND USAGE

Fossil fuels are used in nearly 70% of electrical energy production in the United States. Historically much of the fossil fuel energy was based on coal, primarily from pulverized coal power plants. At its peak coal was responsible for a little over 50% of electricity production [11]. Recently, however this percentage has dropped as a result of many coal-fired power plants being shut down and fewer new ones built. They are being replaced predominantly by natural gas fired power plants. Although the overall percentage of fossil fuel power generation has remained constant (and is predicted to do so for several decades), natural gas is predicted to overtake coal as the larger contributor in fossil fuel power by the year 2040 [11]. The switch to natural gas is primarily due to three factors: 1. Competitive natural gas prices, 2. Greenhouse gas concerns and increasing environmental regulations, and 3. High construction costs associated with coal-fired power plants. Despite these trends, it is predicted that coal will continue to provide around one third of the nation's electricity for several decades [1].

The use of fossil fuel is often affected by political and environmental policies. This is mainly due to the large amount of greenhouse gases in the environment believed to be caused by the large-scale use of fossil fuels for energy production [12]. Thus, the removal of CO_2 is an important requirement for the continued use of coal as a source of energy [1]. Unfortunately, post-combustion CO_2 removal is energy intensive because of the low concentration of CO_2 in the flue gas [12]. Another option is oxy-fuel fired plants which utilize combustion in oxygen rather than air, a process which results in a CO_2-rich gas from which CO_2 capture is made easier. Oxy-fuel combustion, however, is considered expensive and remains largely an un-proven technology [12].

In order for coal to remain competitive with natural gas as a source of energy in the future, new methods of utilizing it in power production must be developed [1]. In addition to oxy-fuel technology, other methods such as advanced-ultra supercritical (A-USC) and integrated gasification combined cycle (IGCC) processes have recently been explored. Each method has advantages and disadvantages, but IGCC power generation is the most proven of these technologies [1, 13]. IGCC power plants have been operating in the U.S. for around 20 years without carbon capture capabilities. These plants are capable of relatively high efficiencies (>50%) compared to pulverized coal and lower CO_2 emissions (20% less than pulverized coal). This technology offers the potential for low emissions and cost effective CO_2 capture. If increasing environmental regulations are enforced on power plants in the future, IGCC could become a competitive source for coal-based electrical energy [1].

2.2 IGCC PROCESS

The IGCC process, like other combined cycle power generation methods, takes advantage of steam which is generated from the primary combustion turbine and generates additional electricity using a steam generator [14]. In addition to this, the IGCC process also utilizes steam generated by the gasification process itself to generate electricity via the steam turbine. Figure 1 shows the layout of an IGCC process [15].

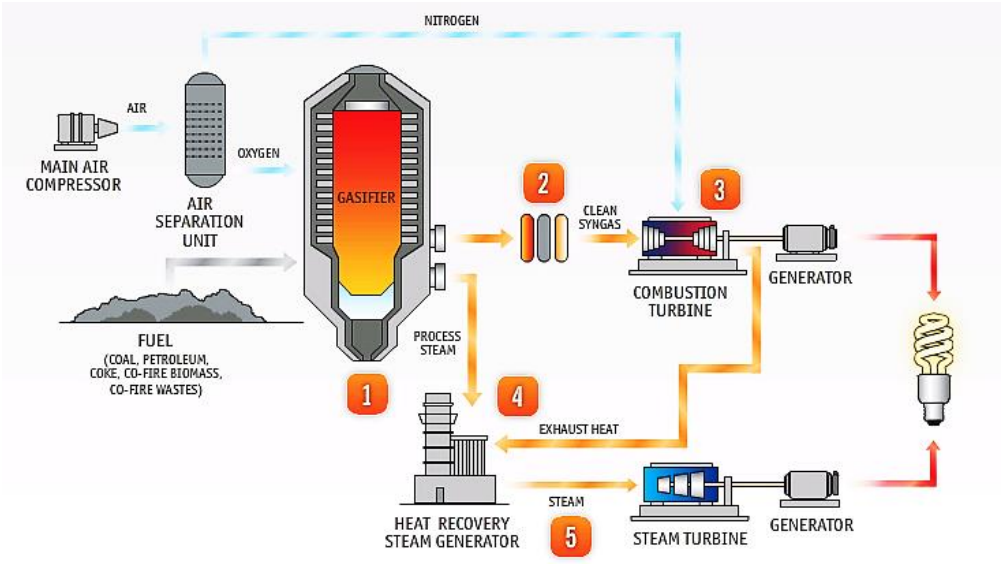

Figure 1: Overview of the IGCC Process [15].

The combustion turbines which are used in the IGCC plants are powered by a synthetic gas, or syngas, which can be produced by a number of organic materials such as coal, biomass, petroleum coke, or some blended mixture of several of these [16]. This is similar to a combustion turbine which is powered by natural gas. There has been much interest in syngas produced by coal because of its low cost and high availability. Unfortunately, the full potential of IGCC plants has not yet been realized. This is mostly due to high capital costs at startup and low availability [17]. The high capital costs will likely be reduced as more IGCC plants are implemented and the relevant technologies developed further. The low availability of these plants, however, is primarily caused by ash from the gasification process that becomes entrained in the syngas and causes fouling further downstream in the system [18]. Most ash fouling occurs in the chillers which cool the syngas before particulate removal. Although it is a problem for availability in the system, it should be noted that the IGCC process overall produces approximately half the solid waste of a conventional pulverized coal plant [5].

A coal-based IGCC plant is a fundamentally different process compared to a conventional pulverized coal power plant [7]. A conventional coal-fired power plant uses the combustion of pulverized coal to generate steam which produces electricity. The combusted coal is fed through the system, and pollutants (CO_2, NOx, sulfur) are typically cleaned from the hot flue gas at the exhaust stack [14]. These pollutants in an IGGG plant can be cleaned from the syngas before it reaches the combustion turbine. This is done at relatively low temperatures where the partial pressures of pollutants are high, making their removal much more efficient [5, 17, 18]. The power cycle of an IGCC plant is based on a Brayton cycle, rather than the Rankine cycle which is utilized by conventional coal-fired plants. This makes IGCC fundamentally different from conventional

coal-fired plants, and more similar to conventional natural gas fired plants. Natural gas based turbines, however, cannot be used efficiently in IGCC plants without modifications to account for the lower heating value of syngas as compared to natural gas [14]. Comparisons in efficiency and availability, however, between IGCC and natural gas combined cycle (NGCC) plants are often made because of their similarities, even though they are fundamentally based on entirely different fuel sources. IGCC plants are not yet as efficient as NGCC plants, mainly because of the gasification process.

Gasification is a chemical process where organic matter is converted to a synthetic gas under high temperature (~1500°C) and pressure (30-80 bars) in a reducing environment [18]. A great deal of research has been conducted on the gasification process itself, which has been utilized in other areas for several decades. There are three main types of gasifiers being used: fixed bed, fluidized bed, and entrained flow gasifiers. Each type has its own benefits and drawbacks, but the entrained flow slagging type gasifier has become the most commonly used for coal based IGCC plants [17]. Mineral matter in the gasifier is condensed onto the gasifier walls as liquid slag which runs down to the bottom of the gasifier and out to a liquid quench. A great deal of effort is put into ensuring that the liquid slag has a low enough viscosity to run down the walls of the chamber. Additional measures can be taken to ensure proper slag viscosity, but these modifications to the gasification process are made at the cost of efficiency and syngas heating capacity [17]. Some mineral matter is volatized and becomes entrained in the syngas as fly-ash. The fly-ash typically has a different chemical composition than the slag, and it is desirable to have the fly-ash stick to the slag and leave through the bottom of the gasifier. However, some of the fly-ash inevitably leaves the gasifier with the syngas and contributes to fouling further

downstream in the process. Efficiency is reduced during gasification mainly because some chemical energy is lost to heat as some fuel is partially combusted at slagging temperatures[5]. Also, additional work is required to generate oxygen.

Hot syngas (comprised of H_2, H_2O, CO, CO_2) leaves the gasifier and is sent to a cooler where it is cleaned of impurities at relatively low temperatures (300°C) [7, 14, 19]. Fouling due to fly-ash in the cooler is the main cause of down time in the IGCC process [5]. Fly-ash composition can vary depending on operating conditions and the type of coal used in gasification. High rank bituminous coal is typically used in entrained flow gasifiers because of its lower ash content and higher overall efficiency, compared to sub-bituminous and lignite coals [5, 19]. Some volatile species (Na, K, Cl, S) can be entrained in the syngas and eventually lead to the formation of oxides and sulfates in later stages. In many cases the formation of the sulfates and oxides occurs during shutdown. An additional component often found in fly-ash is FeS, which is partly due to the reaction between iron in the tubing and the syngas [19].

The components in the IGCC system can be subjected to harsh environments. Each stage of the process has different operating conditions which can include high temperatures, high pressures, and potentially corrosive atmospheres. Materials have to be designed to maintain structural integrity while operating in these environments, but they must also be protected from corrosion and oxidation. Environmental coatings have been developed to protect materials and prolong their useful lifetimes.

2.3 THERMAL BARRIER COATINGS

High temperature materials have been used extensively in turbines for power generation and jet propulsion. The need for higher operating temperatures, and thus higher efficiencies, has led to the development of nickel-based superalloys for components in the hottest sections of the turbine. Commonly used alloys such as PWA 1484 and Rene N5 are ϒ-ϒ' superalloys which are designed to withstand creep and fatigue at high temperatures (up to around 1000°C). Excellent mechanical properties at high temperatures are achieved both from precipitation of cuboidal ϒ'-Ni_3Al and solid solution strengthening of the ϒ-Ni matrix [20]. Recently, the operating temperatures have reached a point beyond the melting temperature of the superalloy, necessitating the use of thermal barrier coatings (TBCs) [6]. TBCs are commonly used on rotating blades and stationary vanes to protect the underlying metal substrate. The purpose of the TBC is to protect the underlying substrate and reflect radiant heat away from the turbine blade [21]. The thermal gradient provided by the TBC, along with back side cooling from the interior of the blade, ensures that the metal substrate is kept at a safe operating temperature. This lowering of the metal surface temperature can extend the alloy lifetimes by reducing creep, thermal fatigue, and oxidation rates. The TBC is comprised of a ceramic coating which has low thermal conductivity and a high strain tolerance [22]. The use of TBCs and back side cooling of the blade

has allowed the use of high efficiency engines operating in temperature ranges exceeding 250°C above the melting temperature of the superalloy [23].

The thermal cycle for TBCs used in power generation and jet aircraft engines (the two primary areas of in interest) are very different and can result in varying failure mechanisms[6]. The main problem with the use of TBCs is that failure immediately follows delamination and spalling of the ceramic coating. This top coat is not “self healing” and does not form a new protective coating. Thus TBC failure is typically sudden and catastrophic, and the use of TBCs is limited by a reliable mechanism of predicting TBC lifetime [24].

2.3.1 TBC Overview

The thermal barrier coating system shown in Figure 2 is constructed of three layers: (1) the bond coat attached to the substrate, (2) a thermally grown oxide (TGO) on the bond coat, and (3) a top coat. Each of the layers above the substrate needs to exhibit good adherence to the other layers around it. These layers also need to exhibit minimal coefficient of thermal expansion (CTE) mismatch with the substrate in order to avoid detrimental stresses upon thermal cycling [25, 26].

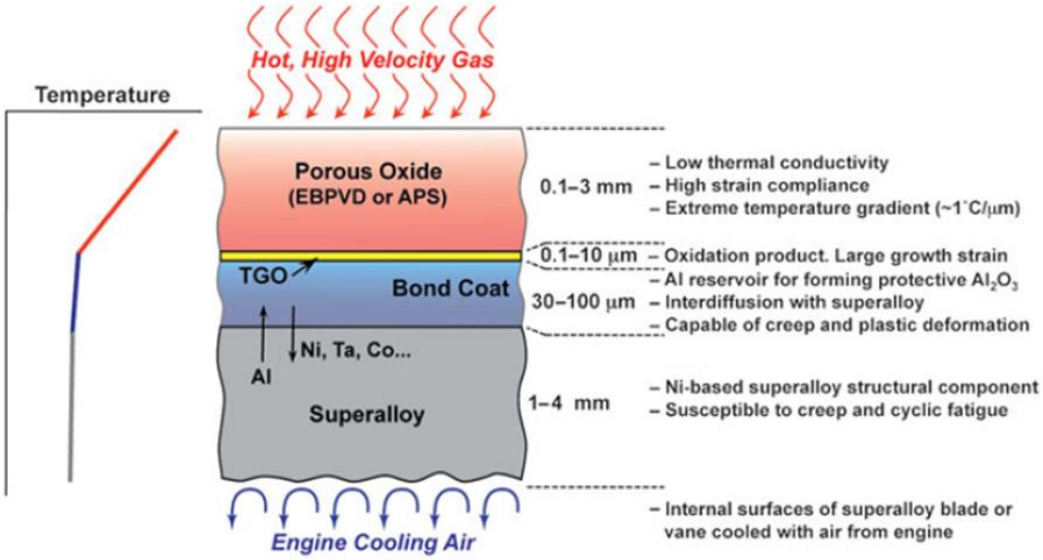

Figure 2: Overview of the TBC system [21].

2.3.2 The Bond Coat

The bond coat layer plays two critical roles in the TBC system: it provides an adherent bond between the ceramic top coat and the substrate, and it also provides corrosion and oxidation resistance [24, 27]. The large CTE mismatch between the top coat and metal substrate would lead to failure in thermal cycling. Oxidation resistance is provided by the growth of a thermally grown oxide (TGO) between the bond coat and ceramic top coat. At high temperatures (>1000°C), alumina (α-Al_2O_3) is used because of its slow growth rate and superior thermodynamic stability. The substrate, which is designed for its excellent mechanical properties, is not a good

alumina-forming alloy. The addition of aluminum necessary to form continuous alumina would adversely affect its mechanical properties. The bond coat, however, does not have any substantial structural requirements and thus can contain the necessary aluminum concentration to form α-alumina [27]. The ability of the bond coat to grow and maintain Al_2O_3 is an important requirement for durability of the system. Transient oxides other than Al_2O_3, and other allotropes of Al_2O_3 (such as θ-Al_2O_3) can have detrimental effects on the system durability. Two types of bond coats are most commonly used in TBC systems: diffusion aluminide coatings, and plasma sprayed overlay coatings[23]. An example of each is shown in Figure 3 [27].

Diffusion aluminide coatings, based on the intermetallic compound β-NiAl, are typically formed by pack cementation. In this process, a part is immersed in a powder mixture and heat treated. The resulting diffusion coating forms (depending on the activity of the pack), either by inward diffusion of aluminum into the substrate, or by outward diffusion of nickel away from the surface [27]. In either case, the β-NiAl phase contains the necessary aluminum reservoir to form the important alumina layer [24]. The addition of platinum to the diffusion aluminide coating by electroplating a layer of Pt prior to the diffusion aluminizing greatly improves scale adhesion [23]. The Pt provides enhanced diffusion of aluminum into the substrate and improved oxidation properties of the aluminide coating [27]. The platinum aluminide coating can either be single phase (Ni,Pt)-Al, or double phase (Ni,Pt)-Al+$PtAl_2$ [27]. Diffusion coatings exhibit a strong inter-diffusion with the substrate and can suffer from the formation of secondary reaction zones and brittle phases [24, 27].

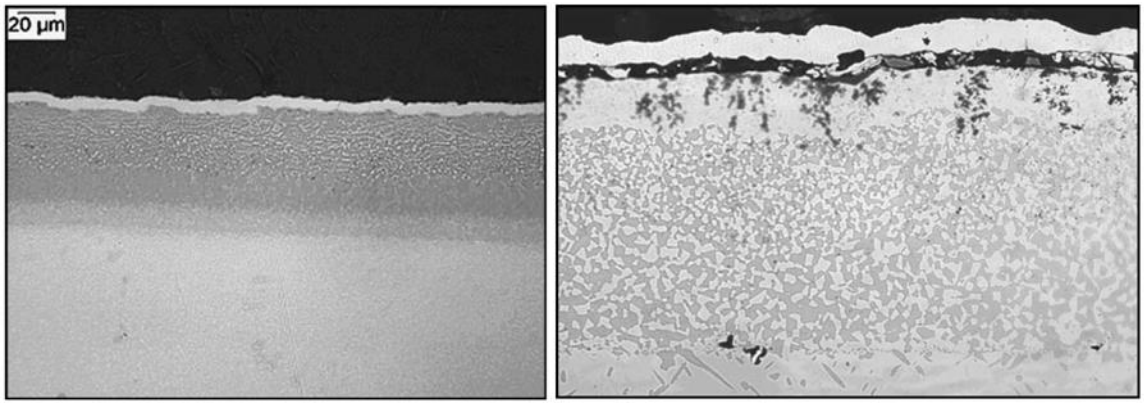

Figure 3: (a) Two phase platinum aluminide diffusion coating, and (b) MCrAlY overlay coating, showing depletion of dark β-phase from alumina growth [27].

Overlay coatings are more independent from the substrate and allow more precise control of chemistry [23, 27]. Plasma spray coatings are commonly used in TBC applications. An argon-shrouded plasma spray can be used to minimize oxygen pickup (below 0.1wt%) in the coating [27]. Overlay coatings used in TBCs are commonly of the MCrAlY type, where M = Ni, Co or both [23]. A NiCoCrAlY bond coat, for example, can be made with 8-12 wt% aluminum to form the continuous alumina layer. The alumina scale formation depends on the activity of aluminum in the metal. The microstructure generally consists of two phases: β-NiAl+Ɣ-Ni. The β -NiAl phase provides the necessary aluminum reservoir to form the TGO, and the fcc Ɣ-Ni phase increases the mechanical properties (ductility and thermal fatigue strength) of the coating [27].

Reactive elements (Y, Hf, Zr) are used in the overlay coating to improve oxide scale adherence [23]. The beneficial effects of yttrium are partly attributed to protrusions of yttria "pegs" into the bond coat that create a mechanical adherence between the two layers. It is also thought that yttria helps scale adhesion by the gettering of sulfur impurities that otherwise

degrade the oxide adhesion [27]. Too much yttrium, however, can result in the formation of intermetallic phases which can oxidize preferentially [23].

2.3.3 The YSZ Topcoat

Zirconia (ZrO_2) has been used extensively in structural applications for several decades due to the fact that it can be stabilized with other oxides in order to control its mechanical properties [28]. It has been used extensively in TBCs because of its low thermal conductivity. The most commonly used ceramic for TBC top coats is zirconia that is partially stabilized with yttria (Y_2O_3). The yttria stabilized zirconia (YSZ) coating exhibits low thermal conductivity, relatively high coefficient of thermal expansion (CTE), excellent adhesion to the Al_2O_3 layer, and high strain tolerance [6, 24, 25]. The YSZ top coat must also demonstrate resistance to delamination upon thermal cycling. The addition of 6-8 wt% yttria, commonly referred to as 7YSZ, has become the most widely used material for TBC applications. This is partly as a result of its superior durability in thermal cycling, as shown in Figure 4.

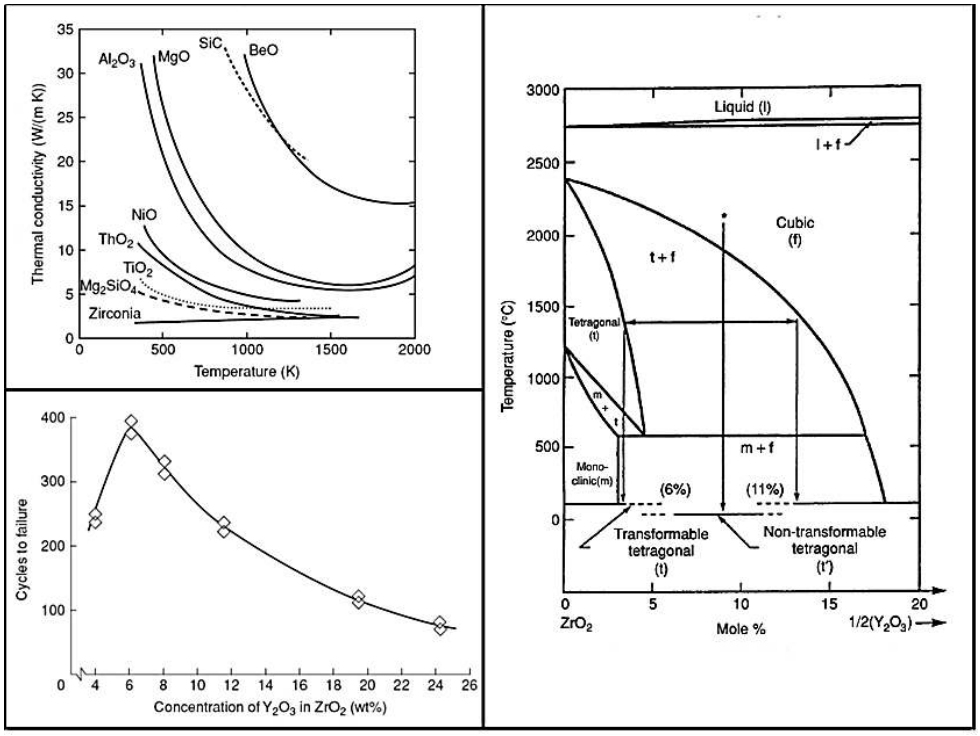

Figure 4: (a) Thermal conductivity of ZrO_2 compared to other materials, (b) a portion of the ZrO_2-Y_2O_3 phase diagram and (c) cycles to failure as a function of Y_2O_3 [29].

The portion of the ZrO_2-Y_2O_3 phase diagram in Figure 4 shows the relevant phases for TBC applications. The three phases at temperatures of interest for current TBC requirements (~1100°C) are the tetragonal (t), cubic (c), and monoclinic (m) phases. The addition of around 7-wt% Y_2O_3 (~4-mol%) results in a metastable phase in the two-phase region between t and c which is labeled non-transformable t' phase. (Here it lies at ~8-mol% because mol% is shown as $YO_{1.5}$.) At 1100°C, the 7YSZ should separate into a Y-lean tetragonal phase and a Y-rich cubic phase, and upon cooling the tetragonal phase would transform into the monoclinic phase as it crosses over the To (t/m) line [30]. Below this line, the monoclinic phase is stable. This phase change occurs

at relatively low temperatures, and is accompanied by a volume change of around 4% which generally results in catastrophic failure of the YSZ. The separation into t and c phases does not happen, however, because cation diffusion in the YSZ matrix is very slow. The sluggish kinetics of the phase separation results in the retention of the 7YSZ composition on cooling to room temperature. Hence the t' structure can be retained upon cooling to low temperatures, and the t→m transition suppressed [31]. The single phase t' will have the same composition (7YSZ) as the high temperature two phase (t+c) composition. If the YSZ is held at higher temperatures (~1500°C), the phases will eventually separate out and the tetragonal will transform to monoclinic upon cooling as it crosses over the To (t/m) line [26]. However, at current operating temperatures of 1000°C the kinetics are too slow for this to be a primary mode of TBC failure, and TBCs typically fail as a result of other mechanisms. These other mechanisms involve deposit induced attack, moisture related degradation, and failure related to bond coat oxidation. Interaction with certain deposits, for example, can leach some Y_2O_3 from the YSZ, thereby lowering composition into the tetragonal field and making the YSZ susceptible to the t→m transition upon cooling [32].

At low temperatures, YSZ obtains its resistance to crack propagation with transformation toughening [28]. Transformation toughening is the result of t→m transformation being induced by the stress around a propagating crack tip. The energy absorbed by the change in crystal structure enhances the fracture toughness. (i.e., Some t→m locally toughens the material and stops crack propagation.) The volume expansion associated with the t→m transition creates a compressive stress locally at the crack tip. This local compression helps stop further propagation of the crack [33]. This transition occurs for YSZ with relatively low yttria content, below the

To(t/m). Transformation is proportional to the amount of undercooling below the To(t/m) line where the tetragonal phase is metastable with respect to the equilibrium monoclinic phase [30]. Low Y_2O_3 content creates a larger driving force for the transition[28]. If the Y_2O_3 content is too low, however, the detrimental t→m transition will occur (away from the crack tip) upon cooling. There is a tradeoff between obtaining good transformation toughening (low-yttria) and avoiding monoclinic phase upon cooling (relatively high-yttria). A yttria content of 2-3mol% (4-6wt%) is optimal [28].

Transformation toughening cannot be responsible for the high-temperature toughness of 7YSZ used in TBCs. At these elevated temperatures, the tetragonal phase is more stable than monoclinic and there will not be any driving force for the transformation to monoclinic [31]. It is generally believed that ferroelastic toughening is primarily responsible for the high temperature toughness demonstrated in 7YSZ [31, 33]. This toughening mechanism involves re-orienting domains (tetragonal grains) in the presence of an applied stress. As the stress exceeds a critical coercive stress, the domain reorientation provides energy absorption similar to that of transformation toughening at low temperatures. This change between two equilibrium states does not involve a change in crystal structure (as opposed to transformation toughening). Ferroelastic toughening only occurs with the tetragonal phase, and thus at higher temperatures, the T_o(c/t) temperature is of interest [34]. (i.e., it is important to stay below this line where the tetragonal phase is more stable.) Because transition to cubic does not occur until very high temperatures, this toughening mechanism is very important for high temperature applications [33]. Although this is considered the primary mode of high-temperature toughening, it should be

noted that over long enough times for significant partitioning of yttria into tetragonal and cubic phases, transformation toughening can also play a secondary role upon cooling.

Two common techniques have been widely used to deposit the YSZ top coat layer of TBCs: the air plasma spray (APS) process and electron beam chemical vapor deposition (EB-PVD) [35]. The two processes are fundamentally different in that the t' phase in EB-PVD grows directly from the vapor phase, whereas in APS coatings it evolves from the transformation from a liquid phase as it cools across the To(c/t) curve. These differences result in different microstructures in the two types of YSZ [28]. An APS coating is characterized by a "splat" morphology and horizontal cracks which run parallel to the substrate. The surface of the substrate is rough, which leads to undulations at the interface of the YSZ and the TGO. This surface roughness helps the adherence between the bond coat and YSZ. In contrast, the EB-PVD top coat morphology is characterized by a columnar structure and a relatively smooth substrate surface [25]. TBCs with APS coatings are generally cheaper to produce and can be applied to much larger surfaces, making them the preferred top coats for land based turbines. The different YSZ structures lead to varying properties. The APS TBCs tend to have a lower thermal conductivity due to the splat morphology and overall lower density [27]. The EB-PVD coatings exhibit a superior strain tolerance and erosion resistance due to the columnar structure. The rough surface of the APS top coat compared to the planar EBPVD interface also affects failure mechanisms which will be discussed in another section. The dense vertically cracked (DVC) TBC is a variation of the APS top coat which incorporates a dense YSZ body, but produces vertical cracks similar to that of the EB-PVD coat [25]. The DVC top coat offers some advantages (and disadvantages) of each of the other two top coats. Micrographs showing typical morphologies of all three top coats are shown in Figure 5.

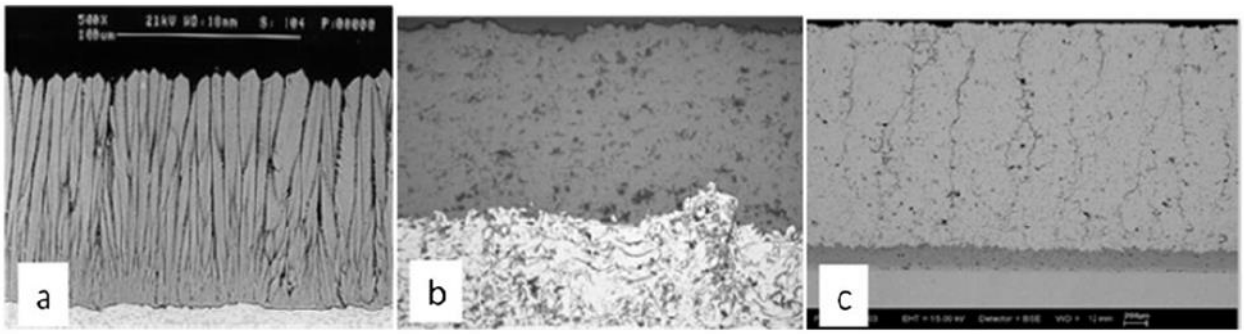

Figure 5: Comparison of (a) EBPVD, (b) APS, and (c) DVC ceramic top coats [24].

Recent studies have demonstrated the effectiveness of a top coat which is deposited using a solution precursor plasma spray (SPPS) method [36, 37]. This method is similar to APS coatings, which are created by injection of a powder into a plasma stream to form the initial liquid coating. The SPPS method, however, is done by injecting liquid drops into the plasma stream rather than dry powder. Ceramic top coats made with the SPPS method can be tailored to incorporate other oxides in solid solution to make them resistant to some deposit-induced attack [38]. Although the method has been demonstrated in working TBC systems, it has not been widely implemented by the industry and the conventional APS and EB-PVD top coats currently dominate the market as the widely used top coats in turbines for aeroengines and land-based engines.

2.3.4 Failure Mechanisms in TBCs

Failure mechanisms can vary for APS and EB-PD TBCs due to the different top coat and bond coat structures [25, 39]. Failure is typically associated with TGO growth and usually occurs at or near the TGO [40]. Different modes of failure associated more with the YSZ top coat can be observed, however, in the presence of particulates and other contaminates in the TBC environment [41-43]. TBC lifetime depends on factors such as maximum operating temperatures, temperature gradients experienced in operations, thermal cycling, and deposit-induced attack [25].

TBCs typically fail when cracks form and propagate in the top coat, causing the YSZ to delaminate and spall off. Since the TBC is not self-healing, once the spalling has occurred the life of the TBC is over [23]. Figure 6 summarizes the most common failure mechanisms which lead to the spallation of the YSZ layer in a TBC. They are classified into two broad categories: intrinsic mechanisms which arise from factors within the TBC system, and extrinsic mechanisms which arise from external factors [44].

As the scale thickens due to thermal exposure, stresses are formed between the bond coat and the ceramic top coat. Stresses also result from the CTE mismatch between the TBC layers and the superalloy substrate. These stresses contribute to eventual TBC failure, and in the absence of other environmental factors (such as deposit-induced attack) the eventual TBC failure occurs at or near the TGO. Delamination of the TBC typically occurs either in the top coat near

the TGO, within the TGO itself, or at the TGO/bond coat interface. Failure which occurs at or near the TGO after thermal cycling is classified as an intrinsic failure mechanism.

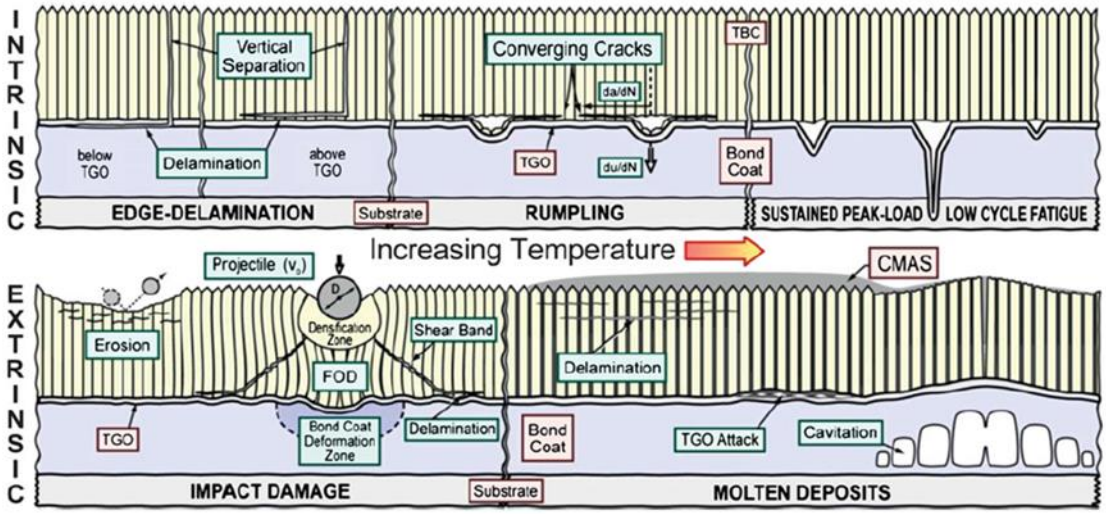

Figure 6: TBC failure mechanisms [45].

Intrinsic failure mechanisms are those which arise from strain misfits between TBC layers during thermal cycling [44]. They are primarily due to mechanisms which are intrinsic to the system itself. Extrinsic failure mechanisms result from damage produced by foreign objects. These types of failures are inherently different from intrinsic failure mechanisms in that they are the result of a "top-down" attack which originates on the TBC top coat, rather than a delamination originating from within the TBC [44]. Failure due to extrinsic mechanisms can dramatically shorten the lifetime of TBCs. This type of failure generally falls into two categories:

erosion or foreign object damage (FOD), and degradation caused by Calcia-Magnesia-Alumino-Silicate (CMAS) deposits which are molten at high temperatures [41, 46]. Erosion is the result of foreign particles such as sand or particles which have broken loose from other components in the system. These particles hit the YSZ and cause small cracks which propagate near the surface leading to delamination. Erosion is typically faster in APS top coats than in EB-PVD top coats because of the horizontal boundaries which separate splats. FOD failure is similar to erosion except that it generally involves larger objects. FOD damage results in larger scale damage and can lead to cracks all the way down to the TGO[42].

2.3.5 Stress in TBCs

Stresses develop from thermal cycling and typically result in delamination near the YSZ/TGO interface[47]. Plasma sprayed top coats tend to experience cracking and delamination farther into the YSZ (away from the TGO). Delamination in EB-PVD TBCs (with MCrAlY bond coats), in contrast, typically occurs along the TGO/bond coat interface [25]. This difference is primarily a result of the horizontal splat boundaries in APS coatings which allow for easy crack initiation and propagation [48]. Cracking in plasma sprayed TBCs will usually extend across the peaks of the undulated interface, and delamination occurs when these cracks coalesce. Delaminated top coats are often characterized by some attached TGO where cracks extend through the TGO at these peaks [25]. Therefore, energy release rate of cracks which propagate through some regions of TGO can also be a factor in the delamination [39].

Figure 7 highlights general principles which govern stress as well as crack formation and propagation at undulations in the YSZ/TGO interface [25]. Initially, the TBC experiences in-plane compressive stress upon cooling due to CTE mismatch with the substrate. The interface attempts to alleviate this stress through deformation of the bond coat, which also causes out-of-plane tensile stress normal to the interface. Cracks eventually form as a result of TGO growth after thermal exposure. The location of crack formation can vary depending on thermal history, but the cracks generally originate from imperfections or defects. Eventually cracks grow and coalesce to cause large-scale delamination.

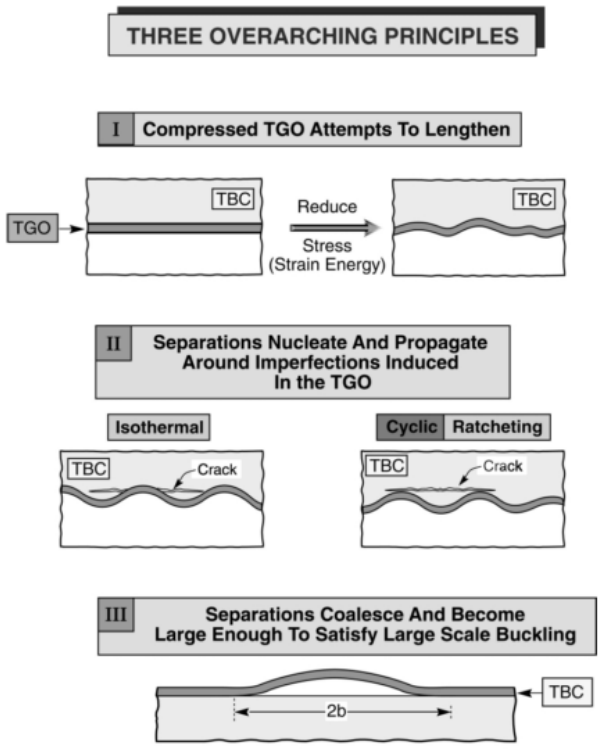

Figure 7: Overarching principles affecting TBC delamination[25].

The driving force behind TBC delamination is the release of elastic strain energy stored in the coating [45]. Delamination typically occurs in one of two ways: edge delamination or buckle-driven delamination near the middle of a specimen [49]. The occurrence of either type of delamination shown in Figure 8 can be affected by factors such as TBC processing parameters, operating conditions, and defects at the YSZ/TGO interface [25, 49].

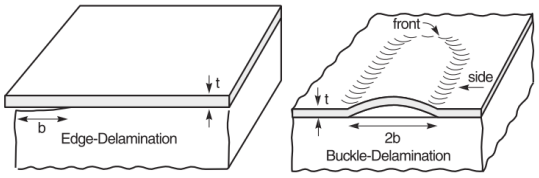

Figure 8: Two types of TBC top coat delamination[49].

The misfit stress, σ, from thermal expansion coefficient (CTE) mismatch between any thin film and underlying substrate is given by the equation

$$\sigma = E\frac{\Delta\alpha\Delta T}{1-\upsilon} \tag{2-1}$$

where E is the modulus of elasticity of the film, Δα is the difference in thermal expansion coefficient between the two layers, υ is Poisson's ratio of the layer, and ΔT is the change in temperature upon cooling [25, 47]. For the TBC system, the CTE mismatch with respect to the substrate can be used to calculate misfit stress for each layer. The CTE misfit stress is a major source of elastic energy which drives TBC delamination [45]. Thus, the energy release rate for delamination (G) is proportional to the elastic modulus and the CTE difference. Typical values for E and α are given in Table 1. If the top coat properties are modified during the lifetime of the TBC, top coat delamination may result. An increase in the elastic modulus would lead to a corresponding increase in the driving force for delamination. Also, if Δα increases (by lowering α of the TBC) then the driving force for delamination is also increased.

Table 1: Typical values for material properties of different TBC layers [25, 39]

Layer	E	α
7YSZ Top Coat	10-50 GPa	11-13 x10^{-6} °C^{-1}
MCrAlY Bond Coat	200 GPa	13-16 x10^{-6} °C^{-1}
Alumina TGO	350-400 GPa	8-9 x10^{-6} °C^{-1}
Ni-based Superalloy	200 GPa	17.1x10^{-6} °C^{-1}

The stresses in a TBC vary in different locations in the top coat, and the stress distribution changes during thermal cycling. He et al. have modeled the misfit stress and energy release rate as functions of CTE mismatch and elastic modulus[47]. Eventually the stress caused by thermal cycling causes TBC delamination. This failure by thermal cycling is affected by several factors:

TGO growth, thermal expansion coefficient mismatch between TBC layers, and deformation in the TGO and bond coat [47]. Figure 9 shows the residual stresses in the TBC due to TGO growth and thermal cycling. The stresses in the top coat normal to the YSZ/TGO interface alternate between regions of tension and compression. As the TGO grows and stresses increase, cracks originate in the tensile regions. These cracks spread through the tensile stress region, but are arrested when they encounter regions of compressive stress. After further thermal cycling, the energy release rate is large enough to propagate the crack all the way through the region of compressive stress into the next area of tensile stress. Eventually, these spreading cracks meet and large-scale delamination occurs.

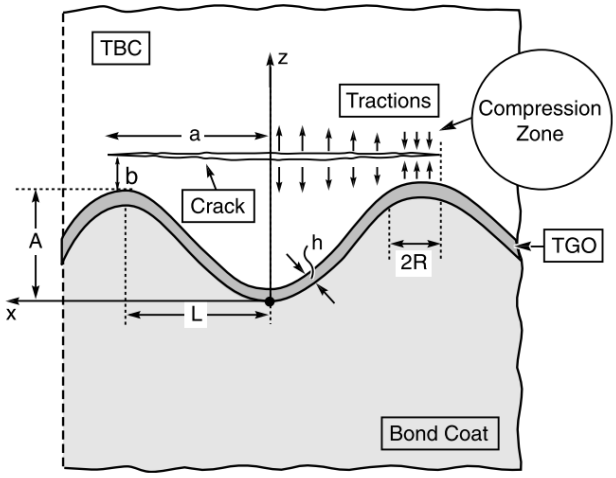

Figure 9: Crack propagation in APS top coat [47].

As a crack of length L propagates through a tensile region of the top coat, G increases until it reaches a region of compression. It then decreases as the crack propagates through the compression region, until it reaches a minimum where it reaches another region of tension and begins to increase again. Therefore, the minimum G_{min} represents the point where the crack has penetrated through the compression region and exceeded the toughness of the TBC, Γ_{tbc}. The value of G_{min} can be used as a failure criterion for the TBC. After a few initial cycles, G_{min} increases almost linearly. The value of G_{min} has been modeled as a function of number of cycles, N, by the following equation

$$\frac{G_{min}}{E_{tbc}L(\Delta\alpha\Delta T)^2} = k(N - N_O) \qquad (2\text{-}2)$$

Where N_o is the number of cycles before G_{min} increases linearly. The value of k is dependent on assumptions made about the TGO and bond coat. Figure 10 shows the energy release rate as a function of crack length, and also the change in G_{min} upon cycling.

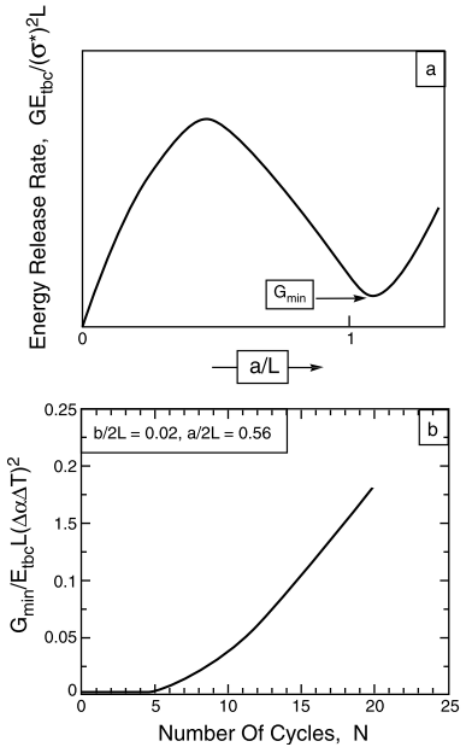

Figure 10: Minimum energy release rate for large scale delamination of TBC top coat [47].

Using these results, the number of cycles to failure, N_f, has been predicted with the following equation

$$N_f = N_o + \frac{\Gamma_{tbc}}{E_{tbc}L(\Delta\alpha\Delta T)^2 k} \tag{2-3}$$

This model relates the number of cycles to failure and the TBC properties of elastic modulus and thermal expansion coefficient. It also uses the failure criteria of $G_{min}>\Gamma_{tbc}$ as the onset of large scale delamination. The number of cycles to failure depends on parameters such as the values of k and Γ_{tbc} which depend on specific processing conditions. Equations such as these demonstrate that failure can be predicted for a specific set of TBC parameters. In harsh operating environments, the values of parameters such as E, α, and Γ_{tbc} can be changed and thus the number of cycles to failure can be altered as well. Equations such as the one above do not take into account the effects of operating environment and changes in TBC properties due to deposits.

The thermal stresses induced in the TBC upon cooling have been summarized by Levi [45] for cases of temperature gradients across the topcoat thickness. The assumption is that the coating stresses are zero at the hottest operating temperature as a result of creep relaxation. As the temperature of the substrate drops from the hot state, T^o, and during cooling experiences a temperature change $\Delta T_{SUB}=T^o_{SUB}-T_{SUB}$. Similarly, the temperature change at the surface of the topcoat, T_{SUR} changes $\Delta T_{SUR}=T^o_{SUR}-T_{SUR}$. The temperature difference between the TBC surface relative to the substrate, $\Delta T_{SUR/SUB}$ can be described by

$$\Delta T_{SUR/SUB} = (T^o_{SUR} - T_{SUR}) - (T^o_{SUB} - T_{SUB}) = \Delta T_{SUR} - \Delta T_{SUB} \quad (2\text{-}4)$$

Upon cooling, the substrate imposes biaxial in-plane strain change, $-\alpha_s \Delta T_{SUB}$, where α_s is the CTE of the substrate. Taking into account the temperature gradient, Equation 2-1 can be written as

$$\sigma(y) = \frac{E_c}{1-\nu_c}\left(-\Delta\alpha_c \Delta T_{SUB} + \left(\frac{y}{h_c}\right)\alpha_c \Delta T_{SUR/SUB}\right) \quad (2\text{-}5)$$

where σ(y) is the stress as a function of the through-thickness, y, measured from the YSZ/bondcoat interface, E_c is the elastic modulus of the YSZ, α_c is the CTE of the YSZ, and h_c is the thickness of the YSZ. Because of the CTE mismatch, the coating should be in compression overall. Equation 2-5, however, shows that cooling of the coating (large $\Delta T_{SUR/SUB}$) can produce an overall tensile stress ($+\sigma$), while cooling of the substrate (ΔT_{SUB}) can impose compressive stress which depends on the CTE mismatch between the YSZ and substrate, $\Delta\alpha_c$. As previously discussed, the driving force behind topcoat delamination is stored elastic strain energy in the topcoat, U, which can now be described by the equation

$$U = \frac{E_c h_c (1+\nu_c)}{2(1-\nu_c)}\left\{(\Delta\alpha_c \Delta T_{SUB})^2 - (\Delta\alpha_c \Delta T_{SUB})\left(\Delta\alpha_c \Delta T_{SUR/SUB}\right) + \frac{1}{3}\left(\alpha_c \Delta T_{SUR/SUB}\right)^2\right\} \quad (2\text{-}6)$$

Equation 2-6 shows that the stored energy in the YSZ is determined by two competing factors: compressive stress arising from cooling of the substrate, ΔT_{SUB}, and tensile stress arising from cooling of the surface relative to the substrate, $\Delta T_{SUR/SUB}$. The stored elastic energy/unit area is plotted in Figure 11 normalized to $U/E_c h_c$. The ΔT_{SUB} axis represents isothermal heating/cooling where the TBC surface is assumed to be heated and cooled to the same temperatures as the substrate ($\Delta T_{SUR/SUB}$=0). In some regimes, the cooling of the surface can somewhat reduce overall strain energy. Larger values of E and/or h_c would cause strain energy to increase. This agrees with previous studies which have reported reduced lifetimes for increasing TBC thickness [50] and also liquid infiltration from CMAS [51].

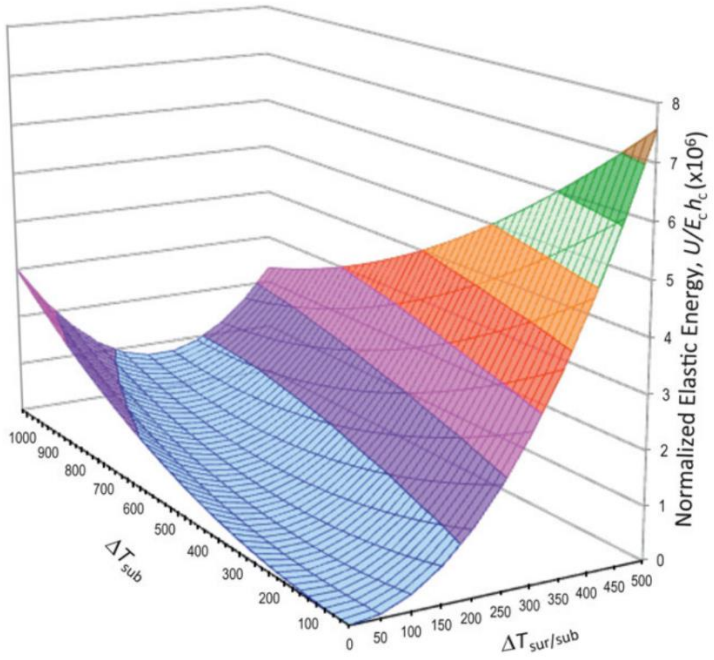

Figure 11: Normalized elastic energy/area in the TBC coating [45].

2.4 ENVIRONMENTAL FACTORS AFFECTING TBCS

TBCs are exposed to different operating conditions when used in land-based turbines for power generation compared to aero-engines. Variations in thermal cycles and gas atmospheres can affect TBC performance and lifetime. EBPVD TBCs used in aero-engines are designed to withstand many thermal cycles. They must also withstand debris from different operating environments as well as from the combustion of jet fuel. Land-based turbines on the other hand typically experience much longer (and thus fewer overall) thermal cycles and only withstand the ambient air from a single location, but they are also subject to contamination from the combustion of a fuel source.

2.4.1 Thermal Effects

The severity of thermal cycling is determined not only by the maximum temperature, but also by the difference between maximum and minimum. Imperfections which form in the thickening TGO cause a significant amount of stress upon cycling [52]. Figure 12 shows the cracking sequence around a growth misfit as the temperature is decreased in a thermal cycle. Radial cracks can initiate in the top coat near an imperfection. As the system cools during the thermal cycle, the CTE mismatch between layers results in a large tensile stress. Eventually, cracks coalesce and spallation occurs through the TGO at the imperfection.

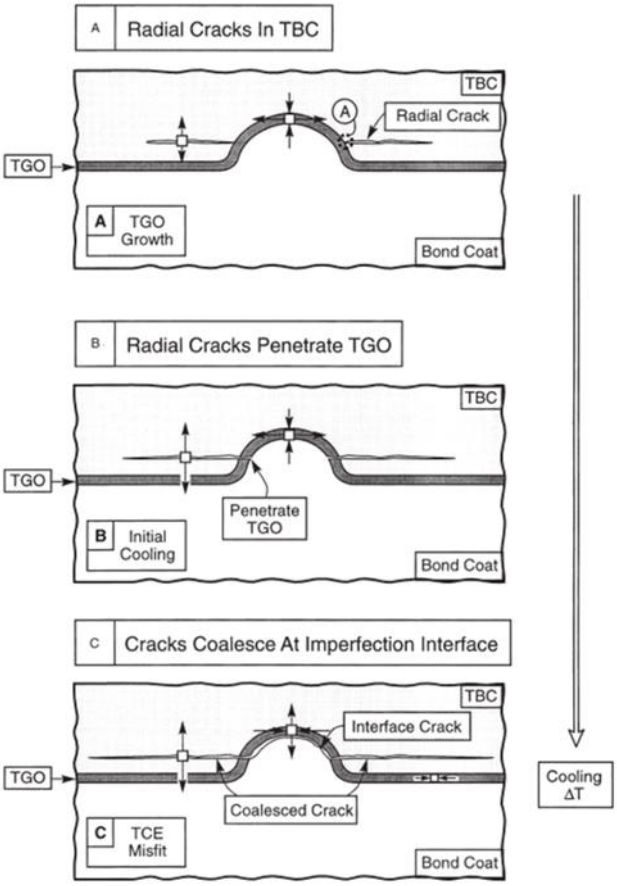

Figure 12: Stress-induced cracking around a growth misfit upon thermal cycling [52].

EBPVD TBCs can utilize diffusion aluminide bond coats or overlay MCrAlY bond coats. In either case, they are characterized by a relatively flat interface between the top coat and bond coat layers (compared to APS top coats) [25, 52]. A common intrinsic failure mechanism for EBPVD TBCs is ratcheting which occurs after repeated thermal cycling [53]. Ratcheting is related to the roughness of the substrate surface, because failure originates at undulated regions created when the TGO plastically deforms to relieve stress. Upon cycling, rumples which originate at these undulations grow and eventually form cracks which extend laterally along the YSZ/TGO

interface. When these cracks coalesce, spallation occurs at this interface and leaves behind the exposed surface consisting primarily of the TGO. In contrast, EBPVD TBCs which utilize a MCrAlY bond coat are more likely to exhibit delamination along the TGO/bond coat interface due to defects which penetrate the TGO [48, 53]. In this case, the TGO develops oxides other than alumina which form “pegs” that grow into the bond coat. The magnitude of these pegs are sensitive to bond coat composition, and delamination eventually occurs along this interface and cuts through the pegs, leaving islands of TGO embedded in the bond coat. In the case of either type of bond coat, failure ensues after cracks propagate along the substrate.

2.4.2 Atmospheric Effects

The adhesion of alumina is important for TBC performance. The use of low-sulfur alloys and reactive elements such as Hf and Y, or Pt, help with adhesion and prolong TBC lifetime [23]. However, atmospheric effects can still cause early failure. The adhesion of the top coat and alumina interface can be compromised as a result of water vapor in the atmosphere [54-57]. This type of failure is observed at room temperature after thermal cycling, and is commonly referred to as moisture induced delayed spallation (MIDS). Failure due to MIDS can shorten the lifetime of a TBC significantly in laboratory experiments and in many cases more accurately describes its “true” lifetime [54]. This is a different failure mechanism compared to normal failure resulting from thermal cycling, although the two are still related.

Failure from MIDS has been observed at room temperature after cool down in EBPVD TBCs. The fact that MIDS only occurs after a critical number of cycles shows that a minimum TGO thickness is necessary for failure [54]. Failure occurs at the scale/metal interface and can be long after cool down. Strain energy from cycling due to CTE mismatch is not enough to cause spallation, but failure occurs rapidly after water is added to the TBC [55]. Moisture effects are particularly detrimental to simple diffusion aluminide coatings (without Pt) because they already suffer from less adhesion as a result of sulfur interfacial segregation [57, 58].

One proposed mechanism for moisture-induced early failure involves the formation of Al-OH bonds at the metal surface which results in a lowered α-Al_2O_3/alloy interfacial toughness [57]. However, when the interfacial toughness is high, as is the case in low-S alloys and on platinum aluminide coatings, this lowered interfacial toughness is not sufficient to cause early spallation [59]. Another proposed mechanism is that water vapor accesses the interface via cracks which develop in the Al_2O_3 during thermal cycling [59, 60]. Water vapor was also observed to have additional effects, such as more transient oxidation prior to α-Al_2O_3 formation and increased formation of spinel phase [59].

Another form of degradation due to moisture is one in which the top coat can transform from metastable tetragonal (t') into monoclinic [28, 61]. YSZ compositions which are desirable for fracture toughness (low yttria content) are more susceptible to another form of degradation which results from moisture environments known as low temperature degradation (LTD). A phase transition from tetragonal to monoclinic can be observed in temperatures below 400°C in the presence of moisture. The mechanism behind LTD depends on OH- ions diffusing through the YSZ lattice and annihilating oxygen vacancies [62]. Anion diffusion is typically slow at low

temperatures, but in this case the smaller charge of OH^- ions compared to O^{2-} ions makes diffusion along grain boundaries relatively fast. The oxygen vacancies are responsible for the retention of the tetragonal phase, and therefore their annihilation can result in destabilization of the metastable t'-YSZ structure at low temperature. YSZ with more yttria content will have more oxygen vacancies, and thus will require much more oxygen vacancy annihilation to cause LTD [28]. This explains why more stabilized (higher yttria content) YSZ with more oxygen vacancy content is more resistant to LTD. Fully stabilized (cubic) YSZ is very resistant compared to t'-YSZ. Cubic YSZ is also characterized by larger grain boundaries, which further increases resistance to LTD because of fewer pathways for OH^- diffusion [61].

Stress transformation toughening and LTD could both occur at relatively low temperatures. However the two processes are inherently different in that LTD is triggered chemically, whereas transformation toughening is induced by stress in the ceramic. Transformation to the monoclinic phase could have detrimental effects on the TBC system at low temperatures experienced in the cold zone during thermal cycling in water vapor atmospheres. Under normal conditions, the tetragonal phase should be retained as the metastable t' YSZ. If, however, the presence of moisture causes the transformation to monoclinic then the volume expansion which accompanies this phase transformation could contribute to early failure of the top coat. LTD at the YSZ surface can result in surface roughening, microcracking, and grain pull-out. Cracking near surfaces can lead to further penetration of moisture species and increased LTD. Engine components can potentially be affected by LTD as steam content is increased in the combustion process in an effort to increase output power. This can also be a potential issue when engine components are washed with high-pressure steam. Furthermore, it is not clear how LTD in TBC

systems will be affected by deposits that can also build up on engine components during combustion.

2.5 DEPOSIT-INDUCED ATTACK IN TBC SYSTEMS

Land-based gas turbines are subjected to lower operating temperatures and frequency of thermal cycles compared to aeroengines. Different challenges, however, are created by harsher environments and much less frequent maintenance schedules [63]. The first stage of an industrial gas turbine is exposed to an aggressive atmosphere which is affected by the type of fuel burned, impurities in the fuel, and impurities in the ingested air. Common impurities in fuel include potentially high levels of sulfur and vanadium [63]. Particulates in the air can originate from ingested air and erosion of other engine components upstream in the system [32, 45, 64, 65]. Ingested impurities in the air can have various origins such as industrial and agricultural dusts and salts, as well as sea-salt containing aerosols [63]. The composition of engine deposits can vary greatly depending on location and operating conditions. The primary constituents of engine deposits are typically oxides of Ca, Mg, Al, and Si which occur in different proportions depending on the source of the buildup [45]. Other constituents which typically occur in lesser quantities, but can play an important role in degradation, are formed from sulfur containing species. Airborne NaCl, for example, can react with sulfur to form Na_2SO_4. Even low levels of impurities in

ingested air can lead to significant deposit buildup over time because of the air-fuel ratio of 30:1 to 50:1 [63].

Deposit-induced attack has been studied in plasma sprayed TBCs as well as EB-PVD TBCs [66, 67]. Deposits can degrade TBC performance in several ways: chemical reaction or attack with the YSZ top coat, change in mechanical properties of the top coat, or corrosion of the bond coat [35]. Chemical reactions can include dissolution/precipitation of the YSZ, or selective reaction with the stabilizer (Y_2O_3) which leads to destabilization of the metastable t' phase. The mechanical properties of the YSZ are typically modified by liquid infiltration into open voids, or by enhanced sintering of the YSZ in the presence of oxides such as Fe_xO_y or SiO_2. Destabilization of the YSZ is typically the result of leaching of Y_2O_3 by selective reaction with deposit constituents or sulfur in the atmosphere. This causes the Y-lean YSZ to undergo the monoclinic transition upon cooling and experience the accompanying detrimental volume expansion.

2.5.1 Hot Corrosion of TBCs

A given TBC is susceptible to being damaged by hot corrosion if exposed to a harsh gas atmosphere and/or deposit chemistry. The hot corrosion of TBCs can result from degradation of the YSZ top coat, the thermally grown oxide, or the bond coat by molten salts. Hot corrosion studies have been conducted with salts at temperatures ranging from 700°C-1100°C in dry air and sulfur-containing atmospheres. The majority of hot corrosion studies in the literature are concerned with Na_2SO_4 as the deposit. A long-standing view has been that NaCl from ambient air

near seawater can react with sulfur impurity in the fuel to form Na_2SO_4 inside the engine [68]. More recent data has also identified relatively high SO_2 levels and particulates in ambient atmospheres which could contribute to hot corrosion.

Although ZrO_2 in the top coat has proven to be extremely resistant to hot corrosion attack, the Y_2O_3 stabilizer may be selectively removed via reaction. This selective leaching of Y_2O_3 could result in Y-lean YSZ which is susceptible to transition to the monoclinic phase. At temperatures above 1000°C, hot corrosion studies of YSZ have not identified any damage to the YSZ top coat from molten Na_2SO_4 or K_2SO_4 [35, 63, 69, 70]. However, top coat damage from vanadium-containing deposits has been well documented in the literature. [69, 71-74] The selective reaction of Y_2O_3 with V_2O_5 results in monoclinic ZrO_2 via the reaction:

$$ZrO_2(Y_2O_3) + V_2O_5 \rightarrow ZrO_2(monoclinic) + 2YVO_4. \quad (2\text{-}7)$$

The degradation can be accelerated with the addition of Na_2SO_4, which reacts with V_2O_3 to form $NaVO_3$ [72]. The Y_2O_3 readily reacts with $NaVO_3$ to form YVO_4, leading to additional formation of YVO_4 (and additional leaching of Y_2O_3 from the YSZ).

The reaction between Y_2O_3 and SO_3 in the presence of Na_2SO_4 led to the formation of Y_2SO_3 and destabilization of the YSZ at temperatures below 1000°C [75, 76] according to the reaction:

$$ZrO_2(Y_2O_3) + 3SO_3(+Na_2SO_4) \rightarrow Y_2(SO_4)_3 \quad (2\text{-}8)$$

A similar reaction is expected in an SO_2-containing atmosphere without the addition of Na_2SO_4.

In addition to the leaching of Y_2O_3 from the YSZ, salts can also infiltrate the YSZ and affect the mechanical properties of the top coat. Vanadate salts should not contribute significantly to "cold shock" type stresses upon cooling, because they contract during cooling [35]. However, the presence of the salts in the open cracks and pores can still reduce the strain tolerance upon cooling [35].

Molten salt penetration through the entire YSZ top coat can result in hot corrosion of the bond coat and contribute to early TBC failure. Intentional vertical cracks in EBPVD TBCS and DVC plasma sprayed TBCs can act as short circuit pathways through the YSZ to the bond coat. Once the fused deposit reaches the bond coat, it can be in direct contact with the alumina TGO. This can accelerate TBC failure primarily by formation of non-uniform, porous layers of mixed oxide scales [63]. Na_2SO_4 has been reported to penetrate through the YSZ at 950°C and promote formation of $Ni(Cr,Al)_2O_4$ spinel oxides [68, 77, 78]. The additional presence of V_2O_3 leads to the formation of $NaVO_3$, which is molten above 610°C and can dissolve the protective oxide. This would lead to the formation of non-protective Na_2CrO_4 and $NaAlVO_4$ [68, 73]. In general, any hot corrosion of the alumina that produces fast-growing oxides will produce additional stress at the TGO/bond coat and TGO/YSZ interfaces and contribute to early failure.

2.5.2 CMAS

Engine design has required increasingly higher operating temperatures, which has led to increasing dependence on the use of TBCs to maintain the integrity of the superalloy substrate. The operation of aircraft engines at combustion temperatures above ~1240°C has led to failure of the top coat due to molten deposits on turbine blades [64]. These deposits consist primarily of calcia-magnesia-alumina-silicate (CMAS) mixtures which melt at these high temperatures. At lower temperatures, they are solid particles which tend to cause erosion damage which is reasonably well understood. At elevated temperatures, however, the deposits adhere to the surface of the TBC as a glassy melt which is drawn into the porous top coat [51, 79]. The liquid CMAS eventually solidifies inside the coating and causes delamination and spallation. In regions where aircraft are exposed to elements such as dust, sand, and volcanic ash, failure due to CMAS attack has become a limiting factor in further increasing operating temperatures in jet engines [32, 45]. TBC damage from CMAS is generally classified into two categories: thermo-mechanical and thermo-chemical effects.

Thermo-mechanical damage to TBC top coats results from changes in the mechanical properties of the YSZ from CMAS infiltration. Figure 13 illustrates a typical CMAS attack on an EB-PVD coated TBC [64]. Molten CMAS penetrates the porous YSZ where it solidifies due to the imposed thermal gradient in the TBC. The solidified CMAS layer causes stress in the YSZ because of the loss of strain tolerance, increased modulus, and low thermal expansion coefficient [64]. The modulus of elasticity in the CMAS-penetrated region can be raised by as much as a factor of three [45]. The infiltrated YSZ eventually spalls from the TBC upon rapid cooling, and in the

presence of more CMAS the process can repeat, leading to significant loss of material. The CMAS-penetrated region can also exhibit decreased erosion resistance and lose further material due to particulates in the gas stream[46].

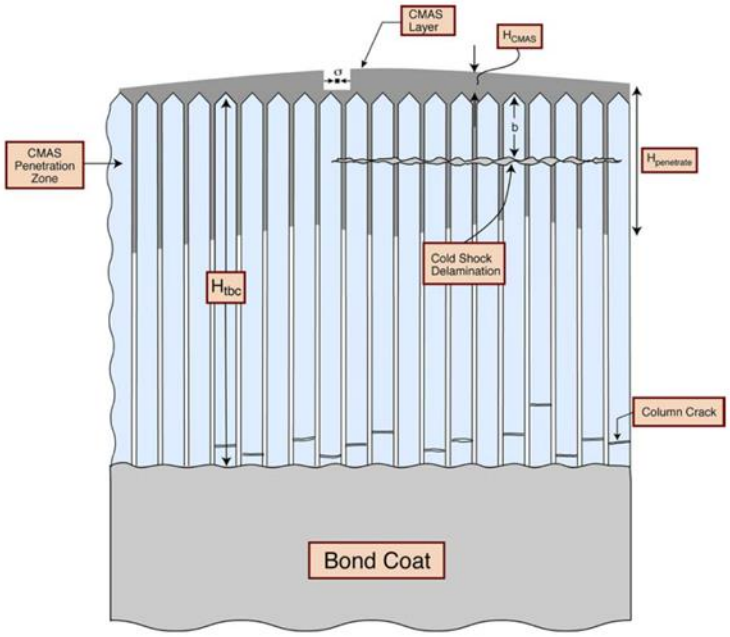

Figure 13: Schematic of CMAS attack on an EBPVD TBC [64].

Penetration of the molten CMAS into the YSZ layer is a function of the viscosity of the fused deposit, the surface tension of that deposit, and the structure and porosity of the top-coat layer [32]. The penetration depth into the YSZ has also been shown to depend on the initial thickness of the CMAS melt [80]. The CMAS has been observed in EB-PVD layers to penetrate all the way to the TGO layer in very short times during isothermal heating [32]. The measured infiltration

times for APS top coatings have been much longer [32, 81] under similar isothermal conditions. The penetration depth is expected to be shorter if a thermal gradient existed across the YSZ layer.

The mechanism by which the CMAS layer infiltrates the TBC is generally different for EB-PVD coatings and APS coatings. The capillary effect between the columns of EB-PVD columns quickly draws the liquid CMAS into the TBC [64]. The molten CMAS in APS coatings spreads into the coating, filling the free space between splats, thereby increasing the overall density of the layer as well as raising the temperature of the coating and promoting further penetration [81]. The dense layer formed by the solidified CMAS can actually act as a barrier to further infiltration until delamination occurs[79]. The detrimental effects of the CMAS infiltration, however, typically offset this benefit. In either type of coating, large stresses eventually lead to cracks which run parallel to the surface of the YSZ and eventually coalesce [80]. Spallation occurs and the useful lifetime of the TBC is significantly shortened. It should be noted that some more dense APS coatings have proven to be more resistant to the infiltration of CMAS [79]. This is because the horizontal splat morphology is not as quickly penetrated by molten CMAS compared to the vertical channels in the EB-PVD coating.

In addition to the thermo-mechanical effects of CMAS penetration, the TBC can be damaged by thermo-chemical interactions with the liquid melt. Destabilization of the t' phase is often associated with a leaching out of the Y_2O_3 from the YSZ coating. In some cases, the molten CMAS melt can dissolve the YSZ and re-precipitate it as either a Y-lean or Y-rich ZrO_2. The Y-lean oxide could then be susceptible to the detrimental t→m transition upon cooling, whereas the Y-rich ZrO_2 would remain cubic in structure [81]. The overall structure of the YSZ could be completely destroyed in the dissolution/re-precipitation process and the coating would have a

completely different morphology. The columns of an EBPVD coating, or the splats of an APS coating, would be replaced by globules of transformed YSZ. Figure 14 shows an APS YSZ coating of a TBC which has been attacked by liquid CMAS, resulting in dissolution and reprecipitation of the YSZ [65]. The porous structure of the YSZ is completely destroyed, and the reprecipitated ZrO_2 grains are not the same composition of YSZ compared to the original coating.

If the molten CMAS is allowed to actually penetrate all the way through the YSZ to the TGO, it can dissolve Al_2O_3. Eventually the CMAS melt becomes saturated with Al_2O_3, inducing precipitation of Y-enriched, non-transformable cubic YSZ [32].

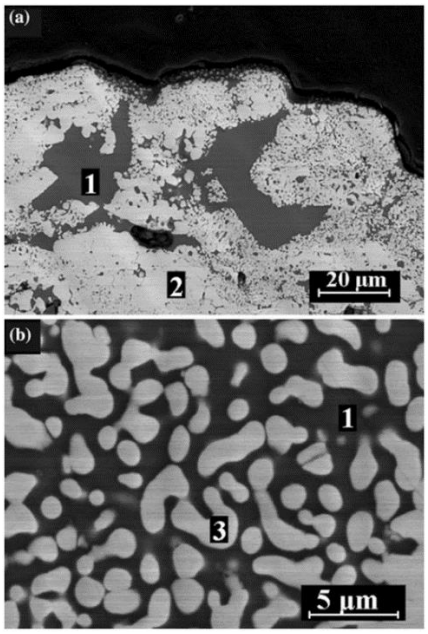

Figure 14: APS TBC top coat that has been infiltrated by CMAS at 1300°C. Regions 1 and 2 show a CMAS island and an unaffected region of YSZ, respectively. Region 3 shows YSZ that has been dissolved by liquid CMAS and reprecipitated [65].

Damage from infiltration requires liquid formation from two or more oxide constituents in the CMAS deposit. If one considers binary mixtures of the primary CMAS oxide constituents, the minimum temperatures for liquid formation can be identified. The binary phase diagrams between the oxide components shown in Figure 15 do not indicate any liquids formed from eutectic compounds below 1360°C. This shows that liquid silicate infiltration from CMAS which has been observed at temperatures ~1250°C involves more than two oxides.

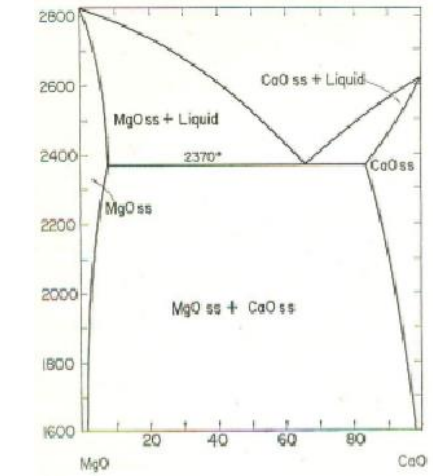

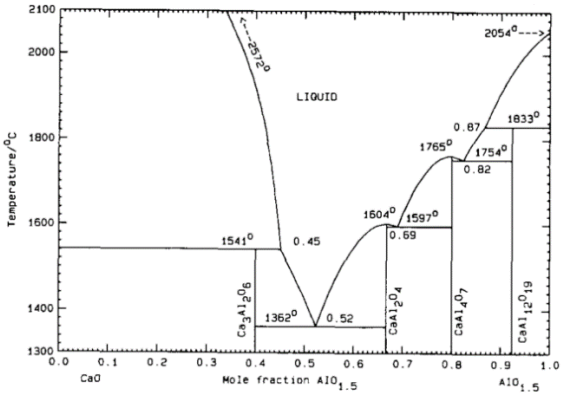

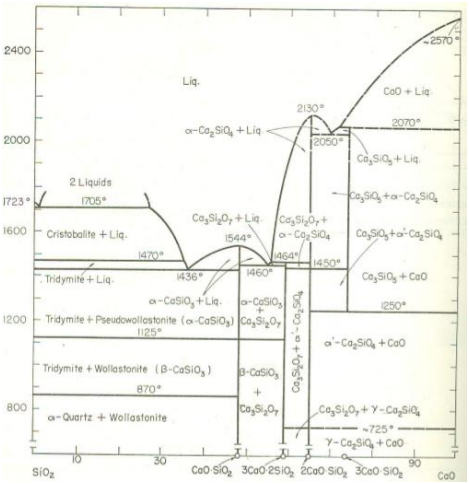

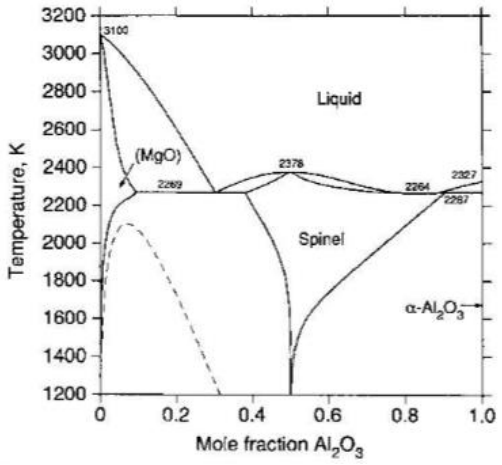

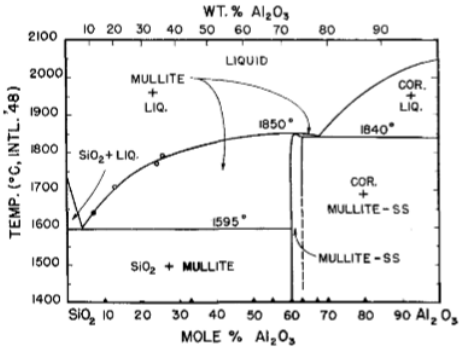

Figure 15: Binary phase diagrams of oxide constituents which comprise CMAS deposits. Phase diagrams are shown for the MgO-CaO [82], CaO-Al_2O_3 [83], SiO_2-CaO [82], MgO-Al_2O_3[84], and SiO_2-Al_2O_3 [85] systems.

Several recent CMAS mitigation strategies have yielded promising results [45]. Successful strategies typically involve changing the chemistry of the YSZ by doping it with other elements that will react with the liquid CMAS [38, 86]. The resulting reaction layer forms a barrier to further ingestion of CMAS into the YSZ. However, these methods of mitigation are largely unproven in long-term industrial use. One problem is that the doped YSZ top coats can lack the necessary toughness to sustain thermal cycling in harsh environments [45]. They can also require expensive retrofitting of manufacturing processes. 7YSZ still remains the industry standard material for TBCs operating at temperatures up to 1200°C-1250°C.

Several studies have modeled the reactivity of CMAS melts with oxides, including YSZ top coats. A common technique for correlating reactivity of deposits with YSZ top coats in TBCs is the use of optical basicity [87, 88]. The optical basicity, Λ, of a silicate liquid depends on the relative concentrations of the oxide constituents. The value of Λ is a measure of the ability of oxygen to donate electrons in a melt. The more readily the oxygen anion is able to donate electrons, the more basic the melt becomes. This tendency of the anion to donate electrons is related to the cation in the oxide, and thus oxides have varying levels of optical basicity for different metal cations. The relative optical basicity of different oxides has been used to predict reactivity. The overall optical basicity of oxide melts can be calculated according to [87]

$$\Lambda = X_A\Lambda_A + X_B\Lambda_B + \cdots \tag{2-9}$$

where X is the fraction of oxygen ions contributed by each oxide and Λ is the optical basicity of each oxide [87, 89]. A more convenient method of expressing this equation for oxide mixtures is

$$\Lambda = \frac{\sum M_i O_i \Lambda_i}{\sum M_i O_i}, \tag{2-10}$$

Where M_i, O_i, and Λ_i are the mol%, number of oxygen atoms, and optical basicity in each oxide, respectively. Optical basicities of relevant oxides to CMAS deposits are shown in Table 2. Optical basicity values for typical CMAS deposits and other engine deposits typically fall within a range of 0.5-0.65.

Table 2: Optical basicities of relevant oxides, adapted from [87].

Oxide	Λ
K_2O	1.40
Nd_2O_3	1.19
Gd_2O_3	1.18
La_2O_3	1.18
Na_2O	1.15
TiO_2	1.00
Fe_2O_3	1.04
CaO	1.00
MnO	1.00
Y_2O_3	1.00
Yb_2O_3	0.94
Sc_2O_3	0.89
ZrO_2[†]	0.86
MgO	0.78
Al_2O_3[‡]	0.60
SiO_2	0.48

[†]Based on Zr^{4+} CN = 8. For CN = 7, Λ = 0.98; CN = 6, Λ = 1.15.
[‡]Based on Al^{3+} CN = 4. For CN = 6, Λ = 0.40.

The predicted driving force for reaction between two oxides is based on the difference between the optical basicity values. A relatively large driving force would exist for reaction between YSZ and highly acidic melts (high in SiO_2) because of a large difference in optical basicity. Less driving force would exist for reaction of YSZ with more basic melts (high in CaO) because the difference in optical basicity values between the oxides is not as large. Some studies of molten deposits have used a ratio (Ca+Mg):Si in the CMAS, along with the alumina content, to characterize reactivity with the YSZ [45]. Typically, CMAS studies report dissolution/re-precipitation of YSZ in silicates that are relatively high in SiO_2 and Al_2O_3. This is also consistent with the concept of optical basicity, in which those oxide melts would be relatively acidic. CaO-rich deposits could be generally considered less detrimental because they are more basic.

Recent CMAS studies, however, of in-service turbine blades have identified corrosion which involves Ca-rich deposits which degrade TBCs by a process that involves reaction with YSZ in the solid state [90-93]. Substantial $CaSO_4$ infiltration shown in Figure 16(a) was observed deep into the inter-columnar gaps of the EB-PVD YSZ. The TBC surface shown in the figure was covered with a Fe,Ti-rich crystalline CMAS (FT-CMAS) deposit. The FT-CMAS was likely deposited from particle impingement on the turbine components resulting from impurities in the gas atmosphere. A magnified image near the YSZ surface shown in Figure 16(b) indicates two additional layers: a Ca-Zr-garnet, and a $CaZrO_3$ layer. The $CaZrO_3$ layer formed from a solid-state reaction between $CaSO_4$ and ZrO_2 at the expense of the YSZ, which left the column tips blunted

[92]. This layer also contained some fully stabilized, cubic zirconia as a result of Y-enrichment in the YSZ near the $CaZrO_3$ reaction zone.

The reported layers of YSZ degradation caused by $CaSO_4$ and FT-CMAS are summarized in the schematic in Figure 17. The infiltrated $CaSO_4$ regions were attributed to a vapor phase deposition in the YSZ pores from a Ca- and S-rich vapor phase prior to FT-CMAS impingement. The $CaSO_4$ near the surface reacted with the YSZ to form $CaZrO_3$. The fully-stabilized ZrO_2 grains formed from Y-rich ZrO_2 that did not react to form $CaZrO_3$. The Ca-Zr-garnet layer that formed between the $CaZrO_3$ was determined to be kimzeyite, $Ca_3(Zr,Ti,Fe)_2(Al,Fe,Si)_3O_{12}$ [91]. This garnet layer was inferred to have formed predominantly from a solid-state reaction at the expense of the YSZ.

The reaction layers shown in Figure 16 occurred instead of typical molten silicate infiltration because the deposit contained lower levels of SiO_2 compared to typical CMAS degradation studies. The $CaZrO_3$ layer is expected to be stable under zero or very low Si-activity. The formation of distinct layers was explained by the temperature dependence of the stable phases shown in Figure 17. The temperature at the column tips during operation would be around 1150-1200°C. Laboratory experiments with $CaSO_4$/YSZ mixtures showed that the onset of $CaZrO_3$ formation occurred around 1150°C [91]. The garnet formed at increased temperatures of >1200°C further from the column tips.

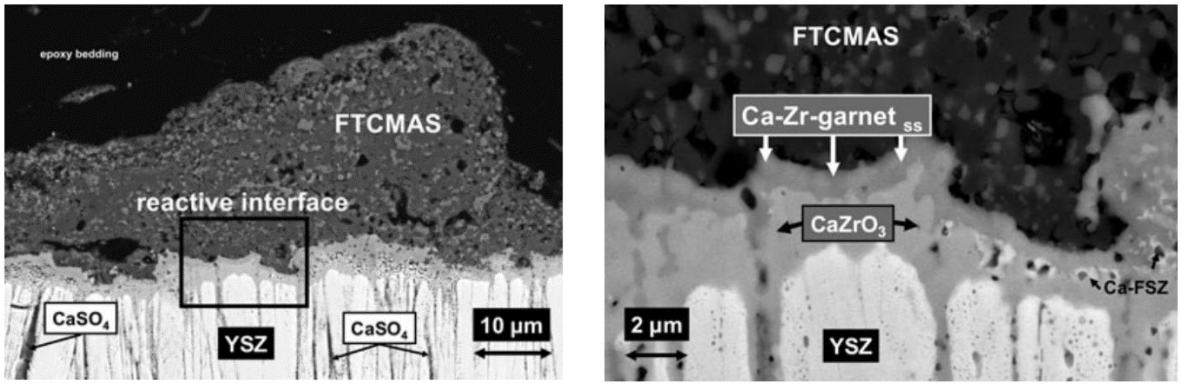

Figure 16: Corrosion of EB-PVD TBC from Fe, Ti-rich CMAS (FTMAS). (a) $CaSO_4$ infiltration was observed in open pores of YSZ and FTCMAS deposit on surface. (b) Closer inspection of the FTCMAS/YSZ interaction revealed additional Ca-containing layers [91].

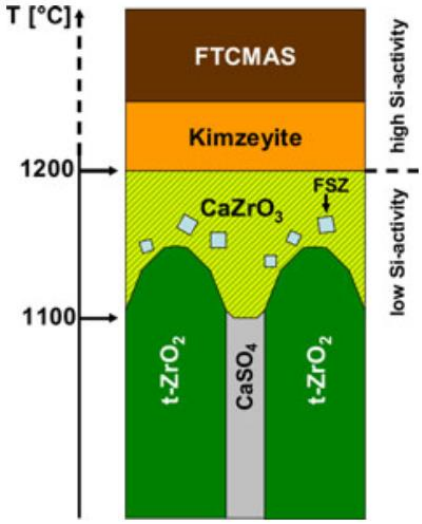

Figure 17: Schematic of FTCMAS degradation of EB-PVD TBC showing layers of corrosion [91].

Some TBC degradation from FT-CMAS was also observed at the TGO/bond coat interface [92]. The TEM image in Figure 18 shows pockets of amorphous TGO which contained $CaSO_4$ and CMAS components (Mg, Ca, S). Newly formed spinel phases ($CaTiO_3$, $MgAl_2O_4$) also indicated

some inter-diffusion with the deposit. This degradation at the TGO could contribute to cracking and eventual spallation of the TBC; although, such failure was not observed in these studies.

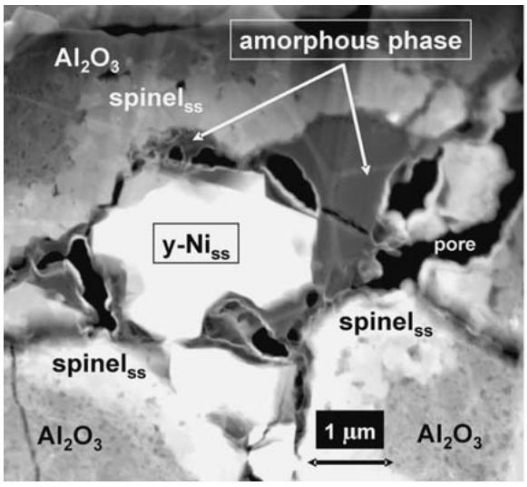

Figure 18: Inter-diffusion between $CaSO_4$/FT-CMAS constituents and TGO [92].

Several interesting aspects of the FT-CMAS deserve further study: YSZ degradation could occur from low-Si deposits; the degradation could result from a solid-state reaction; and the reaction involved Ca. It is also important to note that the reaction with $CaSO_4$ to form $CaZrO_3$ did not occur below 1150°C in those studies. Also, the corrosion of the TBCs did not appear to severely limit the TBC lifetimes; the TBC components remained largely intact and functional prior to their removal for characterization.

2.5.3 Fly Ash

Land-based turbine engines used in power generation often suffer from detrimental effects of deposits which accumulate on turbine and combustor components. The composition of deposits can vary for different fuel types (coal, biomass, petcoke), operating conditions (temperature, power cycle), and atmosphere (geographical location). These deposits are generally classified into a broad category called fly-ash. Deposits can accumulate on TBC components at temperatures below the overall melting point of the fly-ash, and the deposition rate increases with higher temperatures [94]. This can be especially problematic as temperatures are increased to obtain higher efficiencies. Fly-ash deposition rate can be affected by factors such as the temperature of the gas, temperature of the turbine surface, roughness of the surface, geometry of the turbine blade, and impact velocity of particulates

Most of the particulates from the initial fuel source (coal, biomass) in an IGCC plant should be filtered out during cooling and cleaning. However, filters do occasionally fail and/or wear out over time and some ash from the coal can exist in the turbine inlet. Also, when the filtered syngas is combusted in the turbine, it is mixed with air. Much of the fly-ash in the turbine comes from the atmosphere via the air which is mixed with syngas during combustion [7]. The high mass flow rates in land based turbines can result in significant particle buildup on TBC components. A particulate concentration of 0.1ppm by weight can result in 2 tons of ingested material in a large utility power plant during an 8000 hour operating year [94]. Another source of deposit is from erosion of other components in the system [95].

The fly-ash ingested in a turbine can lead to erosion, corrosion, or deposition on coatings inside the turbine. Deposition of fly-ash on TBCs can also lead to blockage of cooling holes, changes in thermal insulating properties and CTE of the ceramic top coat, and infiltration into the porous top coat (above any melting temperatures) [94]. Damage in TBC components due to fly-ash deposits can lead to loss of efficiency and availability in power generation. Much less is understood about degradation mechanisms from fly-ash compared to CMAS.

Figure 19 shows a comparison between common CMAS compositions and typical fly-ash from various sources. One primary difference between typical fly-ash and is a greater concentration of sulfur containing species such as K_2SO_4, Na_2SO_4, and FeS that can enter the ash from the initial fuel source or interaction with engine components upstream from the TBC [45, 94]. Another main difference between CMAS and fly-ash is that the operating temperatures of land based turbines tend to be lower than those of aeroengines. The overall meting point of the deposit is therefore not exceeded, and in many cases the degradation is the result of a solid state interaction between the deposit and TBC. In some cases, partial melting of some constituents may result in some degradation similar to CMAS.

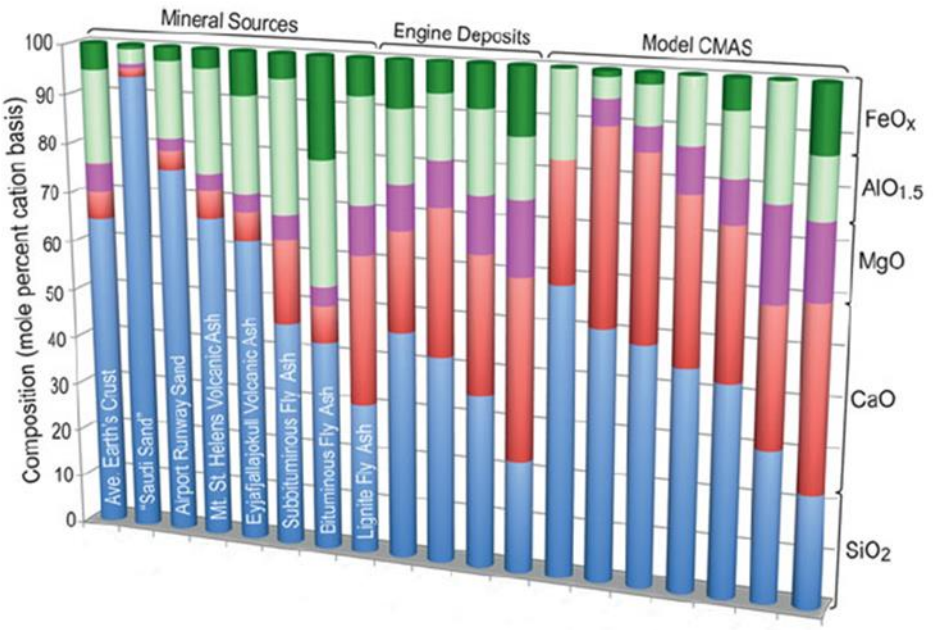

Figure 19: Comparison of common CMAS and fly-ash compositions[45].

Fly-ash commonly found in IGCC power plants contain oxides similar to those found in typical CMAS deposits [96, 97]. Table 3 summarizes a typical fly-ash composition which would be expected from a coal-derived syngas used in an IGCC power plant.

Table 3: Typical IGCC fly-ash composition [96, 97].

	C	SiO_2	Al_2O_3	CaO	Fe_2O_3	K_2O	S	MgO	Na_2O
Wt%	5.5	57	19	6	4	3.5	1	1	1

Previous studies have shown some interaction between fly-ash and TBCs. Figure 20 shows the DVC top coat of a TBC which has been reacted with a coal fly-ash deposit with a composition similar to Table 1 [94]. Some ash deposit can be seen to have penetrated a large crack in the TBC surface. This can be detrimental to the overall lifetime of the TBC because the vertical cracks are necessary to provide strain tolerance in thermal cycling. The infiltration could potentially cause spallation similar to a cold shock mechanism found in CMAS degradation. The infiltration could be made worse with additional levels of lower melting salts such as KCl and K_2SO_4 which could bind fly-ash particles together [94]. The detrimental effects of this type of infiltration in TBCs are not well understood.

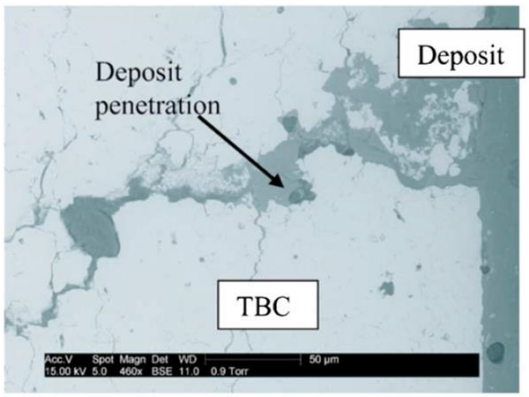

Figure 20: Coal fly-ash that has been reacted with a DVC TBC [94].

Another recent study has examined damaging effects of lignite fly-ash in APS TBCs and mitigation strategies [66]. Figure 21 shows fly-ash has penetrated through the APS coating to the substrate after a 24 hour exposure at 1200°C. Molten fly-ash filled the voids in the YSZ and caused

delamination of the TBC from the substrate. The elemental maps show that fly-ash constituents have penetrated through the entire thickness of the YSZ. Clearly when heated beyond the melting temperature of the ash, the interaction with the TBC is similar to that of CMAS. The ash used in this study was not a typical ash from an IGCC plant. Also, it is not clear what detrimental effects this ash would have had on the TBC at slightly lower temperatures at which the ash (or at least its main constituents) would remain solid.

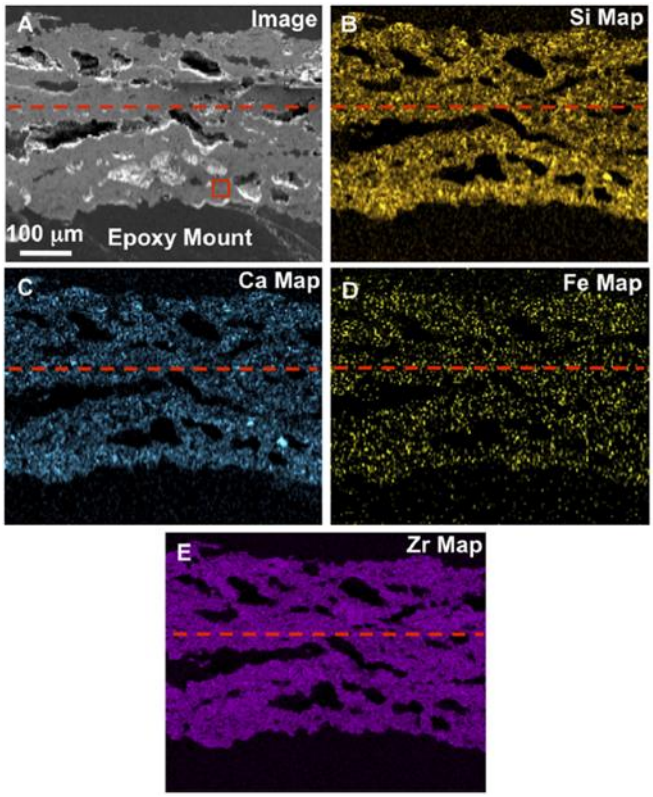

Figure 21: APS TBC that has been reacted with lignite fly-ash.[98]

3.0 AIMS OF CURRENT PROJECT

As economic and environmental concerns push for higher efficiency in power generation, land-based turbines will continue to operate at increased temperatures. This necessitates the study of degradation of turbine components in relevant conditions. Thermal barrier coatings made from 7YSZ topcoats are commonly used in the hottest sections of gas turbines. These TBCSs are subjected to harsh gas atmospheres as well as deposits from ingested particulates in the turbine.

Early TBC failure from deposits at temperatures ≥1250°C has been widely studied. Degradation from CMAS deposits typically results from either a chemical interaction with the YSZ or a change in mechanical properties from liquid silicate infiltration. The fly-ash deposits which are found in land-based turbines contain similar oxide constituent as those found in CMAS. Detrimental effects of these deposits at the relatively lower operating temperature of ~1100°C typical for land-based turbines are not well understood. In addition to oxide components, fly-ash deposits typically contain minor constituents (K_2SO_4, FeS, Na_2SO_4) which are not typically considered in CMAS studies. The effects of salts have been studied on TBC components at lower temperatures ≤900°C. At relatively lower temperatures, molten salts can detrimentally affect

TGO and/or YSZ topcoat. The combined effects of sulfates with CMAS-type deposits are not typically studied.

The purpose of this study is to identify degradation mechanisms of fly-ash deposits on 7YSZ TBCs at 1100°C. As shown schematically in Figure 22, this is a temperature range between that of typical hot corrosion studies and CMAS studies. This temperature is typically not considered detrimental for hot corrosion because of sulfate volatilization. Degradation form CMAS deposits is also not considered at this temperature because extensive liquid silicate formation in the deposit would not be expected. This study, however, aims to identify degradation mechanisms which could be classified in between hot corrosion and CMAS.

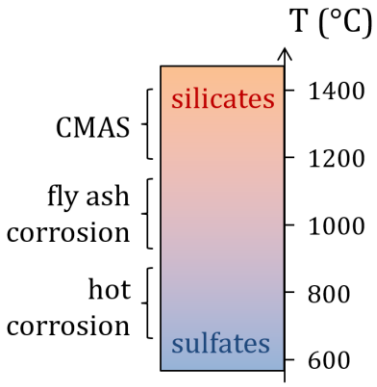

Figure 22: Temperature range of fly-ash corrosion compared to that of hot corrosion and CMAS studies.

Detrimental effects of harsh gas atmospheres on TBCS have been studied. Early TBC failure has been identified after exposure to moisture-containing atmospheres as well as SO_2-containing

atmospheres. The combined effects of these harsh gas atmospheres in addition to degradation from fly-ash deposits at 1100°C is not known. Degradation and early TBC failure from fly-ash deposits will be studied in gas atmospheres containing CO_2, H_2O, and SO_2 which are relevant to IGCC systems. Combined effects of deposits and gas environments which can be most detrimental to TBC lifetime will be identified.

4.0 EXPERIMENTAL

4.1 SPECIMENS

All TBC specimens were provided by Praxair Surface Technologies (PST). Fly-ash testing was done with two main types of specimens: free-standing YSZ and complete TBC systems. The structure and composition used were chosen to represent state-of-the art coatings which are typically used for industrial gas turbines. The composition of the YSZ is given in Table 4. The purpose of testing with free-standing YSZ was to identify degradation of the TBC top coat material itself. The study of free-standing YSZ allowed for systematic basic study of the chemical aspects of damage caused by ash and specific ash constituents. Testing with free-standing YSZ was used to identify problems involving deposits such as destabilization of the t' phase, liquid formation in the deposit, and dissolution of the YSZ. The complete TBC systems were then tested in order to identify the detrimental effects of the ash on chemical and mechanical properties of the TBCs and how those effects limit the performance of the TBCs in thermal cycling.

Table 4: Composition (wt. %) of 7YSZ specimens provided by PST

ZrO_2	Y_2O_3	Al_2O_3	CaO	Fe_2O_3	HfO_2	MgO	SiO_2	Other
Base	7.736	0.011	0.003	0.007	1.69	<0.001	0.013	0.157

4.1.1 Free-Standing YSZ

Free standing dense vertically cracked (DVC) 7YSZ coatings were used for isothermal testing. The microstructure of the free-standing YSZ is shown in Figure 23. Large vertical cracks are distributed throughout the specimen along with smaller horizontal cracks and open pores. The ceramic coatings were initially deposited on aluminum panels. The aluminum was then dissolved in a solution of NaOH and deionized water. For each YSZ panel, 30g of NaOH was added to a 500mL beaker filled with deionized water. The panels were left in the solution at room temperature with a magnetic stir bar for 24 hours, and then ultrasonically cleaned in deionized water. Residual aluminum was removed from the back of the 7YSZ panels with grinding paper. The free-standing YSZ panels were then cut into smaller coupons for testing. Changes in mechanical properties (coefficient of thermal expansion and elastic modulus) of YSZ due to fly ash exposures could also be determined with free-standing YSZ.

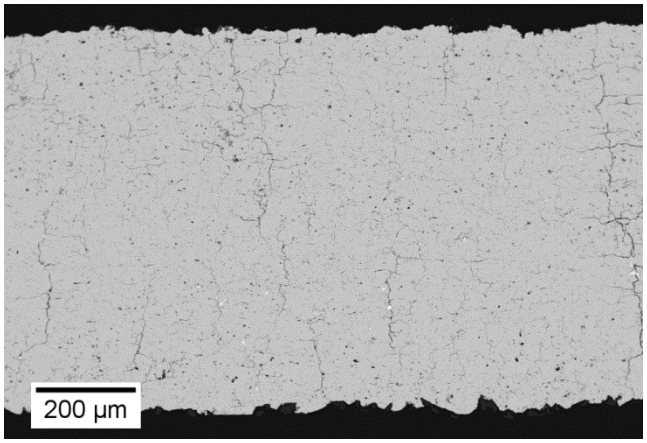

Figure 23: A Dense vertically cracked (DVC) free-standing YSZ sample used in isothermal testing

4.1.2 TBCs

Buttons of the superalloys Rene' N5 and PWA 1484 were used for TBC systems. The 2.5cm diameter buttons were coated with a NiCoCrAlY bond coat by argon-shroud plasma spraying, vacuum heat treated for 4h at 1080°C, and coated with DVC and HPLD TBCs. Nominal compositions of the superalloy, bondcoat, and YSZ layers are provided in Table 4 and 5. Reported nominal densities for DVC and high-purity low-density (HPLD) coatings were 92% and 85% theoretical density (T.D.), respectively. Topcoats were deposited to thicknesses of 375 µm. Previous studies have shown that these high-purity TBCs exhibited excellent resistance to sintering and phase separation at operating temperatures around 1100°C [99]. This was accomplished by controlling impurities such as silica and alumina in the YSZ powder during processing [100]. Apart from any variability in processing, the DVC top coats and the free-standing YSZ samples were essentially the same. Representative DVC and HPLD TBCs are shown

in Figure 24 and 26 in their as-received conditions. As indicated in Figure 23 and 25, the as-deposited DVC morphology can be characterized as having a relatively dense microstructure with large vertical cracks. As discussed previously, these cracks formed during TBC processing and can provide improved strain tolerance in thermal cycling. The HPLD top coat exhibited a comparatively less dense morphology, with discernable horizontal splats and relatively larger voids.

Table 5: Reported nominal compositions (Wt. %) of components of TBC system

	Ni	Co	Cr	Al	W	Mo	Ta	C	B	Re	Y	Hf
Rene' N5	Bal	7.5	7	6.2	5	1.5	6.5	0.05	0.004	3	0.01	0.15
PWA 1484	Bal	10	5	5.6	6	2	8.7			3		0.1
Bond Coat	Base	22	16	13							0.5	

The same dual layer NiCoCrAlY overlay bond coat (175-200 μm thick) was used for all TBC systems. This type of bond coat, exhibiting the two-phase β-ϒ microstructure, is commonly used in land-based gas turbines. The β-NiAl phase, which is shown in the micrographs as the darker phase, provides the source of Al for Al_2O_3 scale growth at high temperatures. A thin thermally grown oxide (TGO) had formed during processing, but was virtually indistinguishable at the magnification shown (x100) in Figure 24 and 26. Both 2nd generation nickel-based substrate alloys, PWA1484 and Rene' N5, were specifically chosen because they are commonly used for turbine blades. It should be noted that these two superalloys were very similar in composition,

and therefore any effects of the substrate (such as interdiffusion with the bond coat) would be very similar for the two different TBCs.

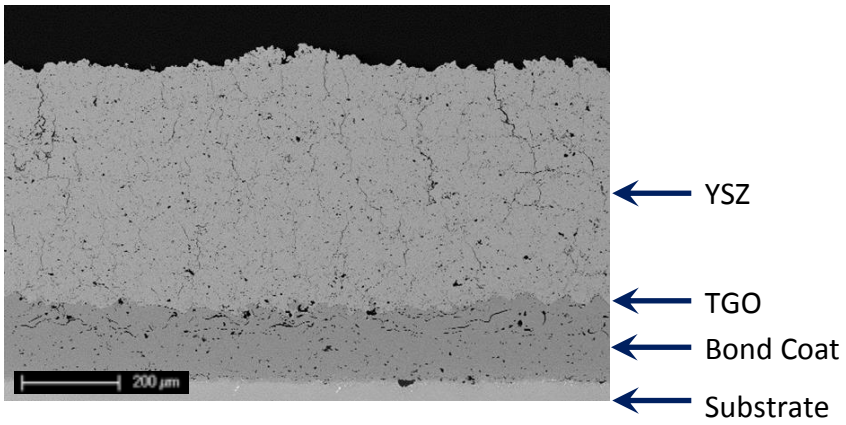

Figure 24: As-processed TBC with DVC top coat which is characterized by an overall dense morphology which includes large vertical cracks

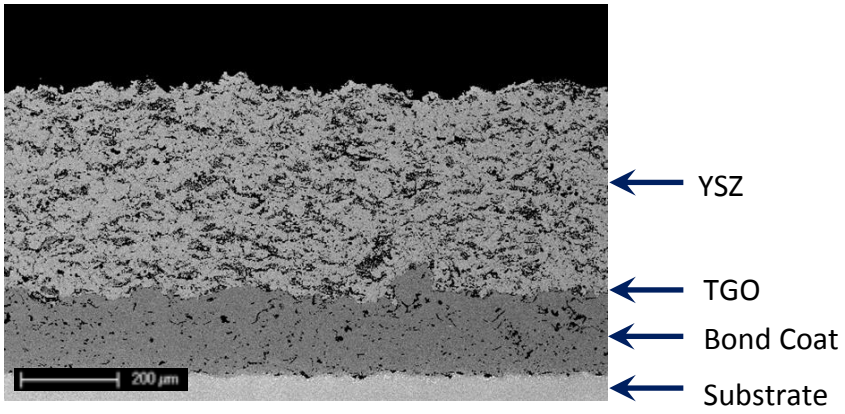

Figure 25: As-processed TBC with conventional top coat which is characterized by splat morphology

4.2 FLY ASH

Testing was done with commercial fly ash, which was obtained from a combustion coal power plant through Boral Fly Ash, and will be described in more detail in the subsequent section. Model deposits were then used to study specific reaction processes. Fly ash was deposited on the surface of all samples before thermal exposure. This was done by mixing a deposit with ethanol to create a slurry. The slurry was applied to the sample with a dropper and allowed to dry. Samples were weighed before and after slurry application to ensure that a deposit loading of 35 mg/cm^2 was achieved. This resulted in a typical ash deposit thickness of approximately 250 μm. The TBC samples were then tested in the thermal cycling rig with the synthetic deposit in contact with the YSZ top coat. The deposited assembly with approximate thicknesses is shown schematically in Figure 26.

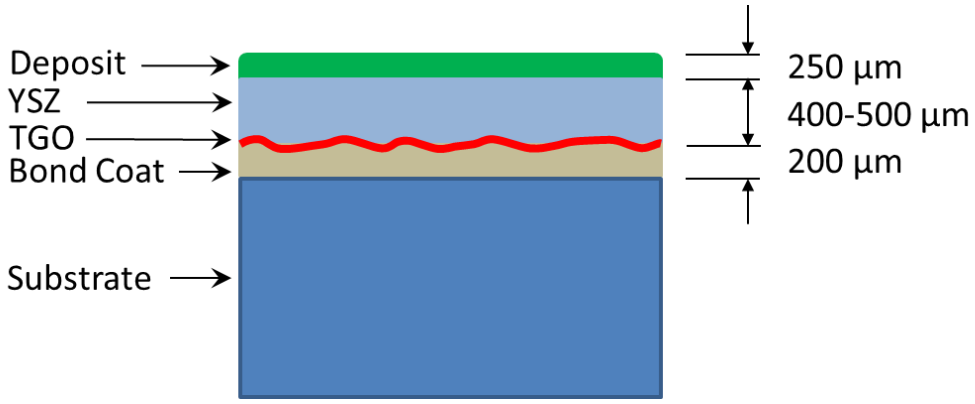

Figure 26: Ash deposit applied to surface of TBC before cyclic testing.

4.2.1 Commercial Fly Ash

Commercial fly ash from a conventional pulverized coal power plant was purchased from Boral fly ash company, San Antonio, TX. The composition of this Class C fly ash is summarized in Table 6. The morphology of the fly ash is shown in Figure 27 and is characterized as spherical ash particles which contain fused ash constituents. This is a typical morphology of coal fly ash which has been reported in literature [9]. The same ash constituents (oxides and sulfates) are expected in a typical IGCC resulting from syngas combustion, though perhaps in different ratios [94, 97].

Table 6: Composition of Commercial Fly Ash (At%)

	CaO	SiO_2	Al_2O_3	MgO	Fe_2O_3	Na_2SO_4	K_2SO_4
Class C	39.2	29.2	13.1	13.2	2.5	2.5	0.3

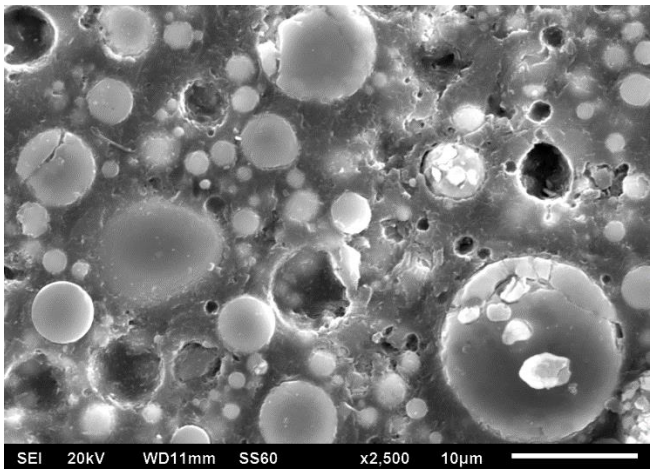

Figure 27: Commercial class C fly ash

4.2.2 Synthetic Fly Ash

Synthetic fly ash mixtures were prepared from commercially purchased oxide powders in order to precisely control the ash composition. The overall strategy in choosing synthetic ash mixtures was to systematically vary a single constituent while maintaining the relative concentrations of the other oxides at constant ratios. Synthetic ash mixtures were prepared by mixing oxides in the desired proportions, and crushing the mixture using a mortar and pestle. Synthetic ashes were then heated at 1200°C for 2 hours in order to obtain partial fusing of ash constituents, and then crushed again with mortar and pestle. Partial fusing was inferred based on SEM-EDS analysis which indicated deposit particles containing traces of all constituents. Some synthetic ash mixtures were then mixed with K_2SO_4 and/or FeS and again crushed together with mortar and pestle. Some model fly ash mixtures were tested with different preparation techniques in order to study the effects of deposit preparation technique on reaction with YSZ.

These results will be discussed in a subsequent section. Unless otherwise noted, all testing was done with synthetic ash described in this section.

4.3 TESTING CONDITIONS

Two different horizontal tube furnaces were used in the configuration shown in Figure 28 for testing of free-standing YSZ and complete TBC systems. A Thermo Scientific three zone furnace was used for isothermal exposures at 1100°C, and an Applied Test Systems (ATS) single zone furnace was used for cyclic exposures between 1100°C (45 minutes) and 160°C (15 minutes). Both furnaces were capable of maintaining gas atmospheres containing dry air, CO_2, SO_2, or steam by using glass end caps that were sealed to both ends of the furnace tubes. Samples were moved horizontally using a magnet outside of the glass end cap that forced an iron-based metal slug to move the sample rod. The opposite end of the sample rod was attached to the sample holder (alumina boat) which was attached via Kanthal wire. Moving samples with a magnet was done manually for the isothermal furnace. The cyclic apparatus utilized an automated ball nut which traveled along a rotating ball screw to move the magnet. This was operated automatically using a programmable controller.

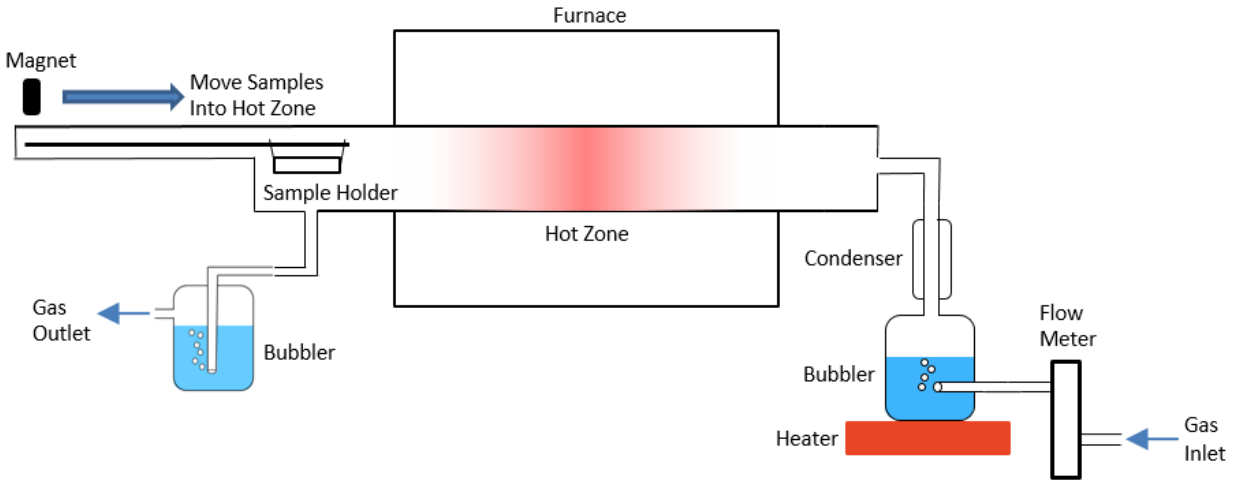

Figure 28: Experimental setup

Atmospheres containing water vapor were achieved using a water bath with bubbler followed by a condenser. The reaction gas passing through the bubbler submersed in a water bath absorbed an amount of water vapor which depended on the temperature. For atmospheres containing 20% water vapor, a temperature of 60°C was required (in accordance with steam tables). The water bath, however, was set at 62°C, in order to slightly over-saturate the gas. This over-saturated gas then traveled through the condenser which was maintained at the desired temperature of 60°C. The main advantage of this process was that the condensation of excess water vapor could be monitored on the walls of the condenser in order to verify the water vapor content was accurate. The gas, now containing the appropriate amount of water vapor, was flowed to the reaction furnace using copper tubing which was wrapped with heating tape to avoid condensation of steam before reaching the reaction tube.

Thermal cycling in the horizontal tube furnace was done with three complete TBCs at a time. This was determined to be the maximum number of TBCs which could reasonably fit in the hot zone of the furnace, and also the maximum number which could be reliably cycled with the magnetic system given the weight of each sample. TBCs were subjected to the same gas atmosphere in the reaction zone as they were in the cold zone. The end cap typically opened and the TBCs exposed to lab air every 160 cycles in order to inspect the experimental setup and maintain the integrity of the sample holder and rod. Thorough inspection of TBCs was done to determine failure. Samples were also monitored by inspection through the clear end cap while the samples were cycled out of the furnace. Partial spallation of YSZ top coat was often observed at the edges, but complete TBC failure was determined when the entire top coat (or what was left after partial spallation) delaminated from the substrate.

Thermal cycling in lab air was done with a bottom loading CM furnace. Thermal cycles in the bottom loading furnace consisted of a 10 minute ramp to 1100°C, followed by a 45 minute hold at 1100°C, and then a 10 minute cooling period in forced air to 60°C. This testing cycle represents a more harsh thermal cycle compared to thermal cycling in the horizontal tube furnace because the temperature change is both greater in magnitude and more rapid. The disadvantage, however, is that the gas atmosphere could not be controlled.

4.4 CHARACTERIZATION TECHNIQUES

After reaction, samples were mounted, cut, and polished to a 1 μm finish using oil-based products to avoid the loss of any water-soluble products. Polished cross sections were examined using a JEOL model JSM6510 scanning electron microscope (SEM). The SEM was equipped with electron dispersive x-ray spectroscopy (EDS) for elemental analysis. The EDS allowed for chemical analysis at specific locations as well as elemental mapping over larger regions. SEM micrographs were primarily used to characterize oxide scale formation and TBC failure. In some cases, Raman spectroscopy was also used on mounted TBC specimens to identify YSZ phases. The cubic, tetragonal, and monoclinic phases each have unique Raman spectra [63]. The occurrence of these different peaks can be used to determine the presence of each phase. Similarly, oxidized surfaces were examined by photo-stimulated luminescence spectroscopy, which allows γ, θ and α polymorphs of Al_2O_3 to be distinguished [64], using a 633 nm HeNe laser in a Renishaw inVia Raman microscope. In addition to SEM and Raman characterization, some characterization with a transmission electron microscope (TEM) was done at Case Western Reserve University.

The elastic modulus measurements of free-standing YSZ were performed using three point bend testing. Testing was done with YSZ samples (1”x.25”x.03”) which had been heat treated for 72 hours. A total of eight samples were tested: four which were heat treated without deposit, and four which were reacted with a synthetic fly-ash deposit. Modulus testing was done by Innovative Test Solutions (ITS) in Schenectady, New York

Dilatometry measurements were performed at Praxair Surface Technologies in order to determine the coefficient of thermal expansion (CTE) of free-standing DVC YSZ samples. The CTE was measured on YSZ which was heat treated for 72 hours with synthetic ash deposit, and compared to identical samples heat treated without deposit.

5.0 COMMERCIAL FLY ASH TESTING

Isothermal exposures to commercial fly ash were used to examine possible degradation from ash produced from a conventional coal-fired power plant. This type of fly ash represents a typical morphology which could be expected of an ash which formed at high temperatures and solidified on downstream components at lower temperatures. Commercial fly ash testing was done as a baseline for comparison with synthetic deposits which more accurately reflect IGCC fly ash.

5.1 RESULTS OF YSZ EXPOSURES TO CLASS C COMMERCIAL FLY ASH

Free-standing YSZ was reacted in dry air at several temperatures with the commercial fly-ash summarized in Table 6. The 100 hour exposure at 1300˚C shown in Figure 29(a) caused severe degradation of the YSZ. The depth of the degradation into the YSZ is indicated in

Figure 30(a). Much of the initial DVC microstructure was unrecognizable after the exposure. This type of severe degradation was similar to CMAS exposures at temperatures ≥1200˚C [32, 65, 86], which was discussed in section 2.5.2. The Raman spectra shown in

Figure 30 indicate the t' phase (indicated by the six distinct peaks) was still evident 500-600µm into the sample, away from the deposit. Closer to the deposit, however, where degradation was more severe, the characteristic t' peaks were less pronounced, indicating loss of the t' phase in the YSZ around 200-300µm from the deposit. The t' phase was not recognizable in the most severely degraded areas ≤200µm from the surface, where the ash was deposited.

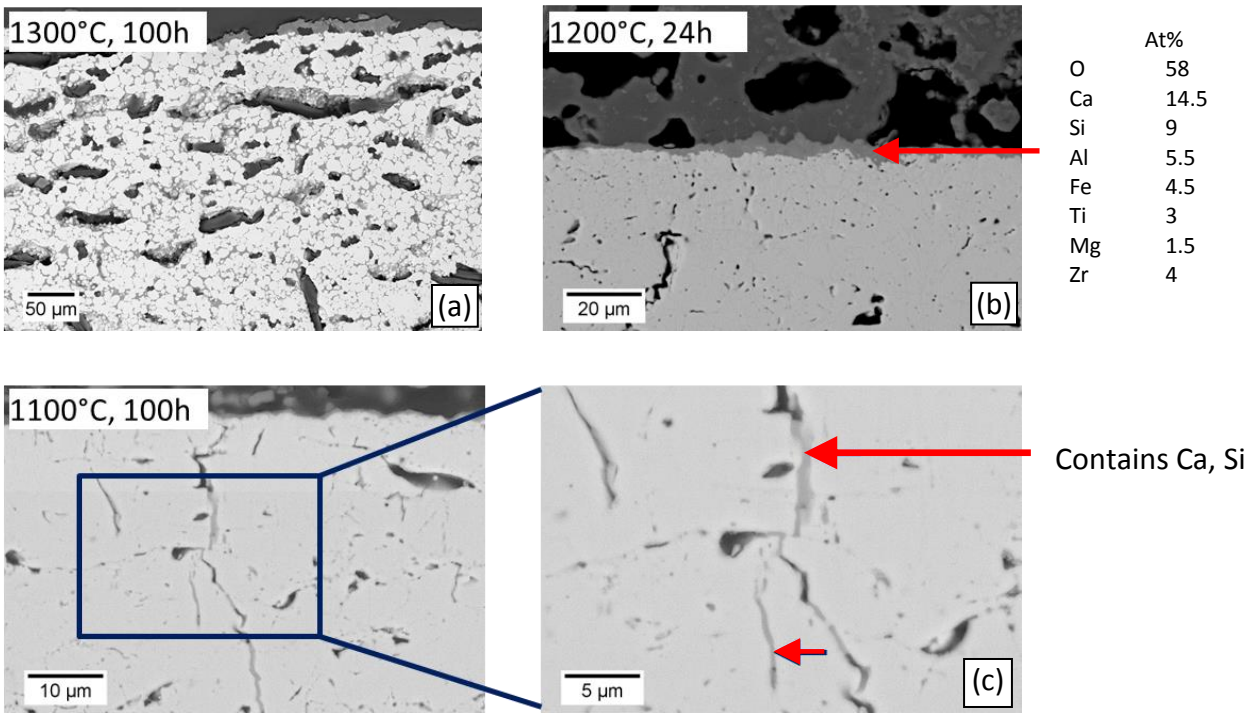

Figure 29: Reaction between YSZ commercial class C fly ash in dry air at three different temperatures. At relatively lower temperatures the extent of damage appears to decrease.

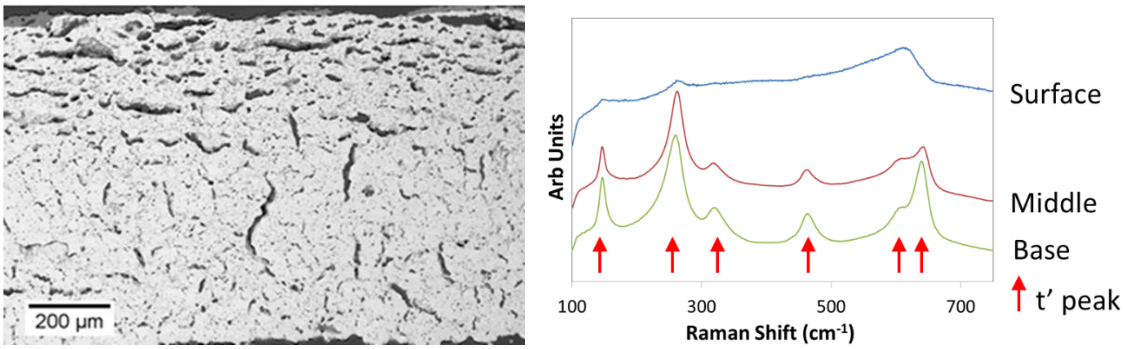

Figure 30: (a) YSZ degradation from 100h exposure to class C fly ash at 1300°C. (b) Raman spectra show loss of metastable t' phase at three penetration depths from the YSZ surface.

The exposure at 1200°C shown in Figure 29(b) resulted in less overall damage to the free-standing YSZ. The morphology of the bulk DVC YSZ was not significantly altered from the as-processed state. Although, the formation of a complex reaction layer between the deposit and YSZ surface was evidence that some damage could occur at this temperature. The dense reaction layer along the surface of the YSZ contained ash constituents and did not appear to significantly infiltrate the YSZ as was the case in the 1300°C exposure.

Detrimental effects of deposit infiltration are not typically reported in studies at temperatures below 1200°C. Silicates formed from oxide constituents of a deposit would not be expected to melt at temperatures less than 1200°C [92, 95]. Exposure to the commercial ash at a lower temperature of 1100°C is shown in Figure 29(c). There was no observed continuous reaction layer formation between the ash and YSZ. However, examination of sub-surface cracks revealed some infiltration of ash constituents into the YSZ. EDS analysis indicated that infiltrated regions up to 40µm below the sample surface contained Ca and Si.

5.2 DISCUSSION OF COMMERCIAL ASH TESTING

The extensive degradation at 1300°C was similar to what has been observed after CMAS exposures. The composition of the oxide constituents in the commercial ash used in these exposures was similar to common CMAS deposits, and thus it is reasonable to conclude that the degradation observed here was the result of a dissolution-precipitation process [32, 92, 93, 101]. At the relatively lower reaction temperature of 1200°C, no evidence of extensive liquid formation from the deposit was observed. This was consistent with CMAS studies [45] which typically do not report extensive liquid formation at temperatures below ≤1200°C. However, the formation of a surface reaction layer indicated that some damage could result at this temperature. The reaction product contained CMAS oxides in addition to Fe and Ti. A similar product has been observed to form from a solid-state reaction with the YSZ in other studies [91, 93]. These results demonstrate the important role solid-state reactions could play in TBC degradation at temperatures (≤1200°C) below those typically considered in CMAS studies.

Fly-ash exposures at 1100°C resulted in some small cracks being filled with ash constituents up to 50 µm below the YSZ surface. The onset-of-melting temperatures of CMAS constituents reported in the literature are typically around 1200°C [32, 102]. The lowest reported eutectic temperature involving oxide constituents (CaO-MgO-Al_2O_3-SiO_2) of the ash is 1170°C [32]. Therefore, apparent liquid formation in this study likely involved other fly ash constituents such as Na_2SO_4 and K_2SO_4. These minor constituents are not typically included in CMAS studies, and

therefore the potential consequences of deposit infiltration at 1100°C are not well understood. The two primary cation components of fly ash, Ca and Si, were also detected in the infiltrated regions of the TBC. These results indicated a need to investigate CaO and SiO_2 combined with minor sulfate constituents such as Na_2SO_4 and K_2SO_4.

6.0 THE ROLE OF CaO

Nearly all deposits which reacted with 7YSZ TBCs contained some level of Ca [45, 94, 103]. Previous studies of turbine blades have identified CaO and $CaSO_4$ as important species which may react with YSZ [90, 91, 93], depending on the ash composition. However, the effect of those reactions on the overall lifetimes of the TBC are not yet understood. Fly ash typically contains relatively high levels of Ca. Previous studies [90, 92] on turbine blades removed from service showed that Ca-bearing compounds could infiltrate YSZ top coats, and this was shown in chapter 4 with a deposit containing 39% CaO at a temperature of 1100°C. Synthetic ash mixtures, therefore, were used in order to study the effect of CaO levels on reactivity with YSZ (in the form of free-standing samples). The CaO levels in synthetic deposits were systematically varied and studied in dry air at 1100°C.

6.1 SOLID-STATE REACTION OF YSZ WITH CAO

Figure 31 shows the reaction of YSZ with synthetic-ash deposits containing systematically varying levels of CaO. High concentrations of CaO (≥63 at. %) in the deposit resulted in the

formation of a reaction product at the YSZ surface where the deposit was applied, indicated by arrows in Figure 31. EDS analysis indicated that the reaction product contained only Ca, Zr, Y, and O. Therefore, other oxide constituents in the synthetic ash did not appear to affect reaction with the YSZ. Analysis with EDS also showed the same 1:1:3 molar ratio of Ca:Zr:O in the product formed from exposure to pure CaO and CaO-rich synthetic ash. The reaction layer was continuous along the YSZ surface after exposures to deposits with ≥ 70 at. % CaO. Examination of high magnification SEM images taken beneath the surface showed that the reaction product did not penetrate significantly into cracks in the YSZ.

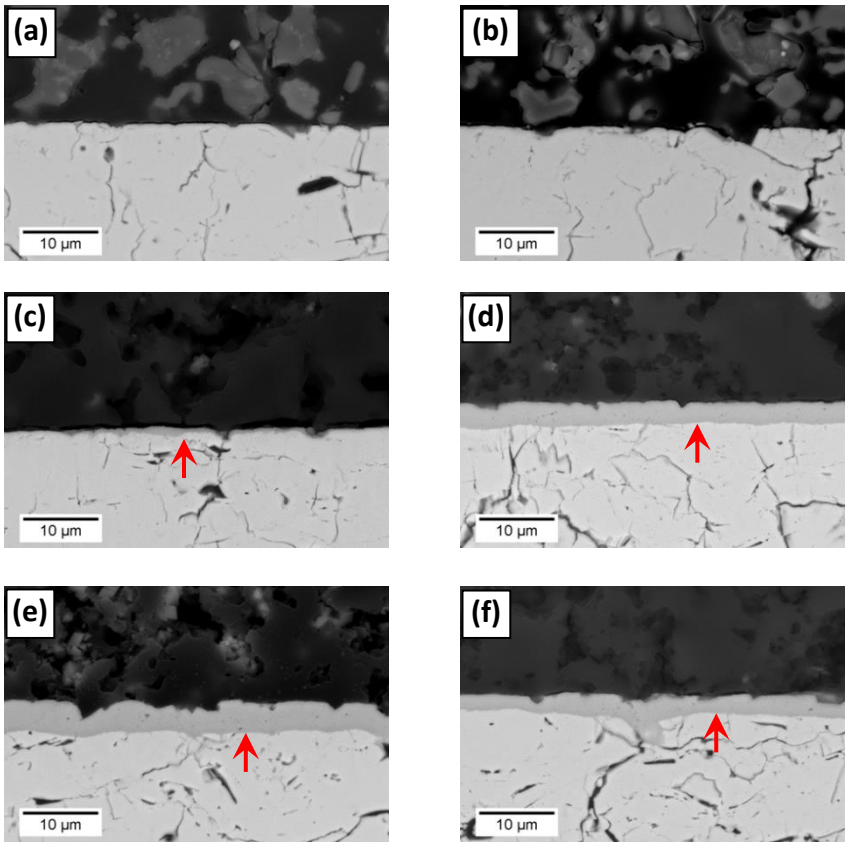

Figure 31: Reaction with YSZ and synthetic ash mixtures containing oxides with (a) 12, (b) 46, (c) 63, (d) 74, (e) 85, and (f) 100 at. % CaO for 72h in dry air at 1100°C. High-CaO (≥60%) mixtures form dense reaction product layers on the YSZ surface, indicated by arrows in the micrographs. Synthetic ash compositions are shown in Table 7.

The reaction between CaO and ZrO_2 can produce several products. The ZrO_2–CaO phase diagram shown in Figure 32 indicates that two compounds are possible at 1100°C, $CaZr_4O_9$ and $CaZrO_3$. The 1:1:3 molar ratios of Ca:Zr:O consistently measured by EDS in the reaction products shown in Figure 31 indicated that the product formed in all exposures was $CaZrO_3$. XRD analysis of the surface reaction layer shown in Figure 32 confirmed that the reaction product was $CaZrO_3$,

calcium zirconate. The formation of $CaZrO_3$ from CaO and ZrO_2 can occur according to the reaction:

$$CaO + ZrO_2 = CaZrO_3 . \quad (6\text{-}1)$$

The standard free energy change ΔG^o=-48.8 kJ/mol [104] associated with this reaction at 1100°C indicates that the reaction would proceed with a minimum activity of CaO, a_{CaO}=0.0139 (assuming unit activity of ZrO_2 and $CaZrO_3$).

Table 7: Synthetic ash compositions (at. %) used in reactions with YSZ to show dependence of CaO level on surface reaction layer.

	(a)	(b)	(c)	(d)	(e)	(f)
CaO	12	52	63	74	85	100
SiO_2	58	32	25	18	10	0
Al_2O_3	17	9	7	5	3	0
MgO	9	5	3	1	1	0
Fe_2O_3	4	2	2	1	1	0

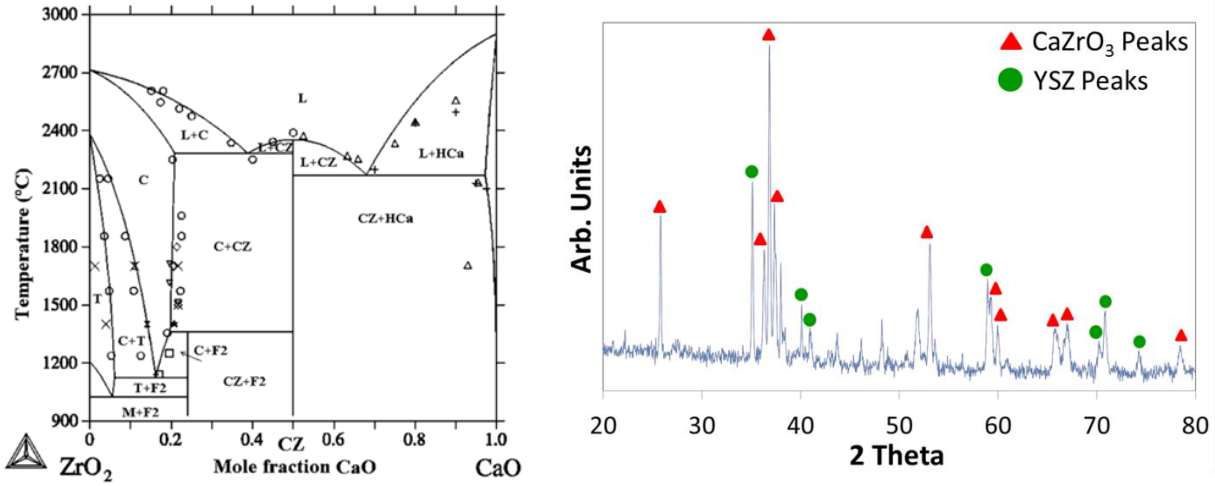

Figure 32: (a) Binary ZrO_2-CaO phase diagram showing two possible compounds at 1100°C, and (b) XRD scan of YSZ surface after a 72 hour dry air exposure to CaO-rich ash at 1100˚C showing formation of $CaZrO_3$ product.

The $CaZrO_3$ surface layer formed between YSZ and CaO thickened over time. The reaction layer thickness was calculated using image threshold analysis. An example of the threshold analysis shown in Figure 33 shows how the area of $CaZrO_3$ was isolated. The overall thickness of the reaction layer was then estimated by dividing the area of $CaZrO_3$ by the total width of the micrograph. This was repeated for several locations along the YSZ surface. The thickening kinetics of the $CaZrO_3$ layer are shown in Figure 33 as a plot of reaction layer thickness (x) vs. the square root of time ($t^{1/2}$). The fact that the plot of x vs. $t^{1/2}$ is linear shows that the reaction layer thickens according to parabolic kinetics, which indicates that growth was diffusion-controlled. The plot also indicates an incubation period in which a continuous layer had not yet formed on the YSZ surface. The formation of a continuous surface layer could have been initially obstructed by lack of even contact between CaO particles and YSZ. The details of this incubation period were not investigated in this study.

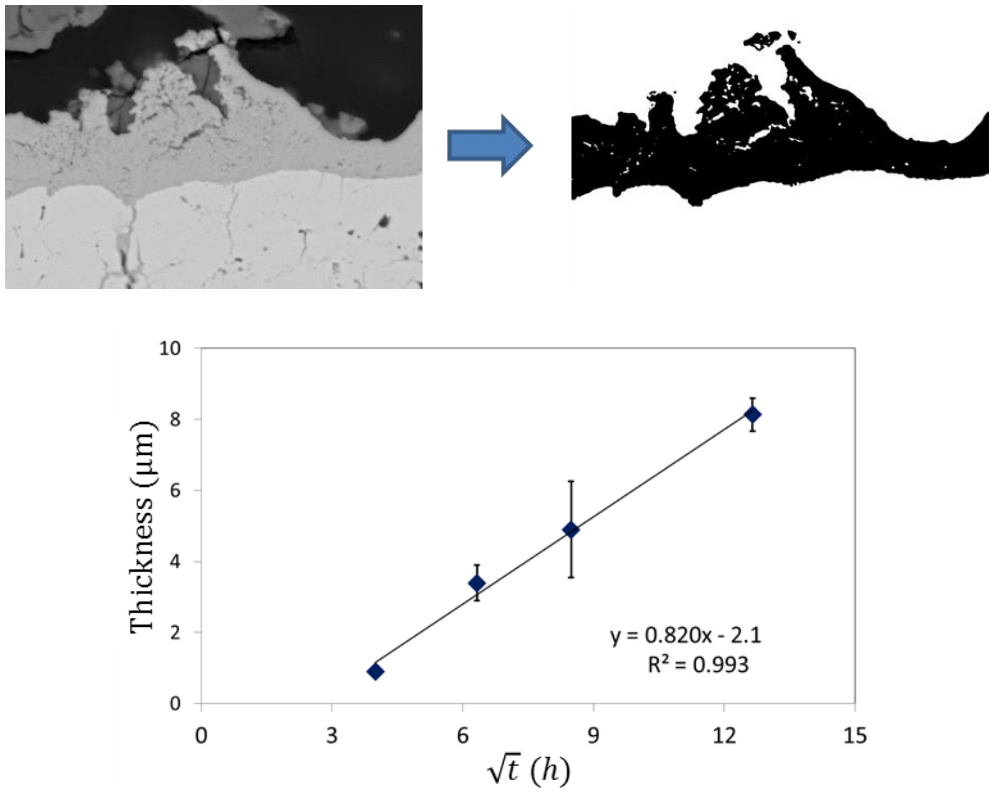

Figure 33: (a) Image analysis used to calculate reaction layer thickness on YSZ surface, and (b) growth kinetics of $CaZrO_3$ layer formed from reaction between YSZ and CaO.

6.2 $CAZRO_3$ FORMATION WITH SYNTHETIC ASH DEPOSIT

Deposits were tested with 72h exposures in dry air at 1100°C and additions of FeS and K_2SO_4, common constituents of fly ash produced from coal and biomass fuels [9, 10, 96, 97]. A synthetic fly-ash deposit was tested with the systematic additions of K_2SO_4 and FeS summarized in Table 8. These variations were used to study the degradation caused by individual deposit

components (oxides, K_2SO_4, FeS). Figure 34 shows micrographs and EDS maps of Ca for the same high-CaO deposit with variations in the addition of K_2SO_4 and FeS. Each 72h exposure at 1100°C resulted in the formation of a $CaZrO_3$ layer on the YSZ surface. The combined addition of K_2SO_4 and FeS, as indicated in Figure 34(b) caused a reaction product to form in cracks inside the free-standing YSZ samples. This reaction product was determined through EDS analysis to be $CaZrO_3$ because of a 1:1 molar ratio of Ca:Zr. The $CaZrO_3$ formation is shown in more detail in Figure 35. The internally forming $CaZrO_3$ was observed more than 100μm into the YSZ.

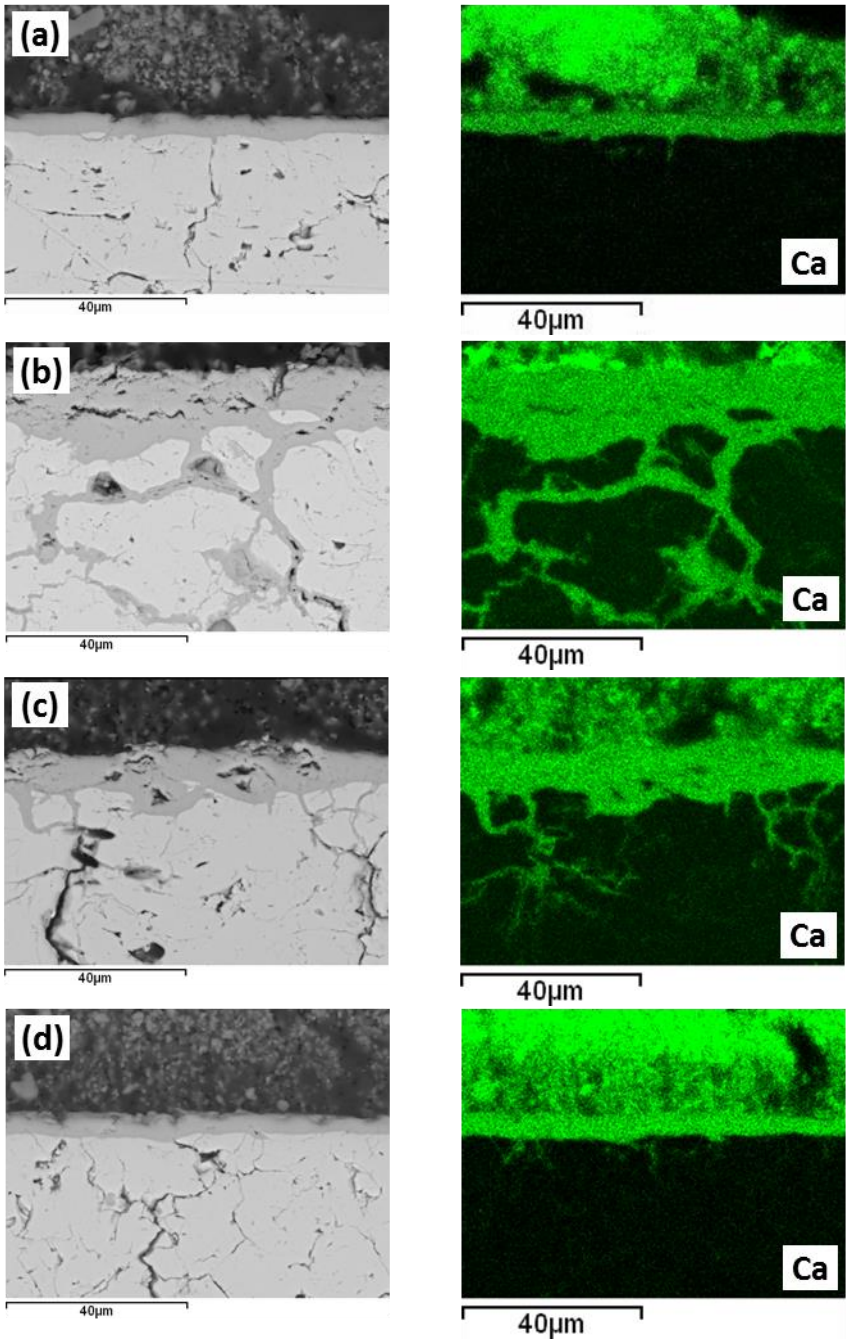

Figure 34: Free-standing YSZ that was reacted in dry air for 72 hours at 1100°C with the same high-CaO synthetic fly ash (a) containing only oxides, and with additions of (b) 2 mol % K_2SO_4 and 4 mol % FeS, (c) 2 mol % K_2SO_4, and (d) 3 mol % FeS. The Ca map for each shows the extent of Ca corresponding to $CaZrO_3$ reaction product in the YSZ for each exposure. Deposit compositions for each exposure are presented in Table 8.

The presence of FeS in the deposit did not appear to significantly affect the extent of internal $CaZrO_3$ formation in the YSZ. The Ca mapping shown in Figure 34 indicates that the same internal $CaZrO_3$ formation occurred for deposits containing both K_2SO_4 and FeS compared to the deposit which contained only K_2SO_4. This suggests that the addition of FeS to the deposit did not cause internal $CaZrO_3$ formation in the YSZ.

Table 8: Composition of synthetic ash deposits (mol %) used to compare effects of K_2SO_4 and FeS on $CaZrO_3$ formation in free-standing YSZ after 72 hour 1100°C exposures in dry air.

	CaO	SiO_2	Al_2O_3	MgO	Fe_2O_3	K_2SO_4	FeS
(a)	85	10	3	1	1		
(b)	80	9	3	1	1	2	4
(c)	83	10	3	1	1	2	
(d)	83	9	3	1	1		3

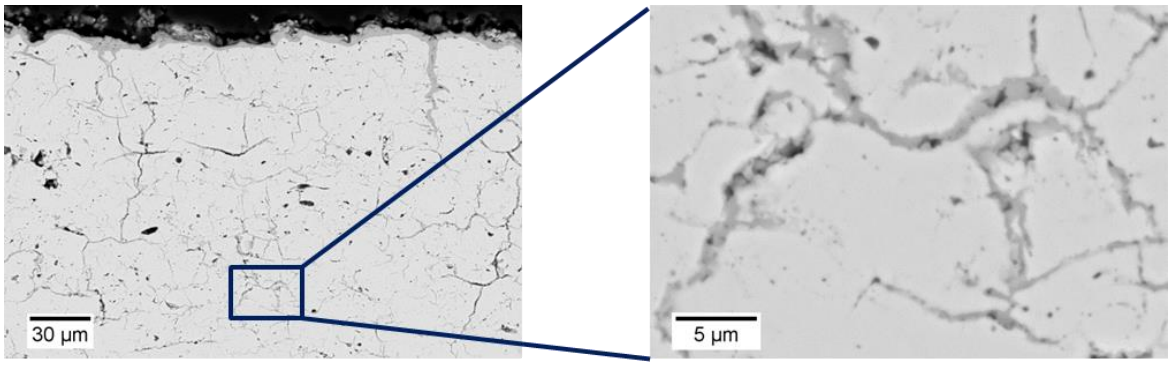

Figure 35: CaO-rich synthetic ash with K_2SO_4 causes $CaZrO_3$ formation in small cracks in YSZ after 72h dry air exposure at 1100°C.

The internal $CaZrO_3$ formation was studied in more detail using localized FIB milling and corresponding TEM analysis. Representative images are shown in Figure 36. These images were obtained from the same 72 hour dry air exposure at 1100°C shown in Figure 35. The TEM images were taken at a depth of about 150µm below the TBC surface. The reaction product is shown filling the entire width of the crack. There do not appear to be any additional phases between the reaction product and the YSZ, which would be indicated by a different contrast and/or variation in EDS data. This suggests the absence of secondary products which may have formed between the main product and the YSZ. The Ca:Zr:O molar ratio of 1:1:3 found by EDS analysis of the infiltrated crack, Figure 36, confirms that the reaction product in the crack consists predominantly of $CaZrO_3$. The figure also shows K_2SO_4 (labeled as scan 1 in Figure 36) which contains ~1 mol % Ca in solution.

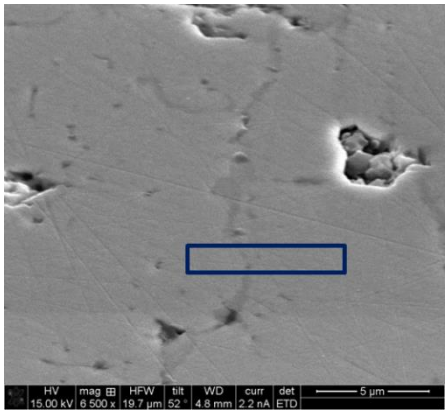

	1	2
O	65	63
Al	0.5	
Si	1	
S	15	
K	17	
Ca	1	17
Fe	0.5	0.5
Zr		19
Y		0.5

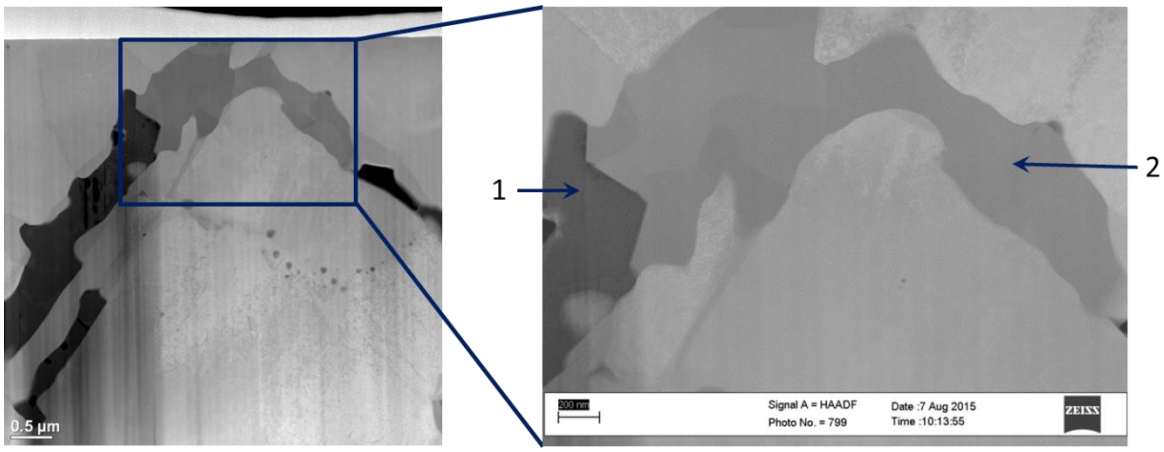

Figure 36: (a) Location of FIB milling at infiltrated YSZ crack. (b)TEM images show crack filled with $CaZrO_3$ and liquid K_2SO_4. EDS data (mol %) shows $CaZrO_3$ formation and some solubility of Ca in K_2SO_4.

6.3 INTERNAL $CAZRO_3$ FORMATION INVOLVING CAO-K_2SO_4 DEPOSITS

The only synthetic ash constituents which contributed to internal $CaZrO_3$ formation in YSZ at 1100°C were CaO and K_2SO_4. Other oxide components in the deposit did not appear to significantly contribute to the formation of $CaZrO_3$ inside the YSZ. Deposits which contained only

CaO and K_2SO_4 were reacted with free-standing YSZ samples at 1100°C in dry air. $CaZrO_3$ formation on the surface and in cracks inside the YSZ was observed after reaction with CaO-K_2SO_4 deposits. The result of reaction with 0.5CaO-0.5K_2SO_4 (wt. %) deposit is shown in Figure 37 for exposure times of 1 and 70h. EDS mapping of K and Ca for each time shows the penetration of K and Ca into the YSZ. The EDS mapping of S matched that of K. After a 1 hour exposure, significant levels of both K and Ca were observed in many of the cracks in the YSZ. However, there did not appear from SEM images to be significant $CaZrO_3$ formation after 1 hour. The EDS mapping after 70 hours showed considerable Ca in cracks inside the YSZ, and $CaZrO_3$ formation was observed in SEM images of the sample. The presence of K, however, was significantly decreased after the 70 hour exposure. The EDS signal from S was also reduced to the same extent as that of K.

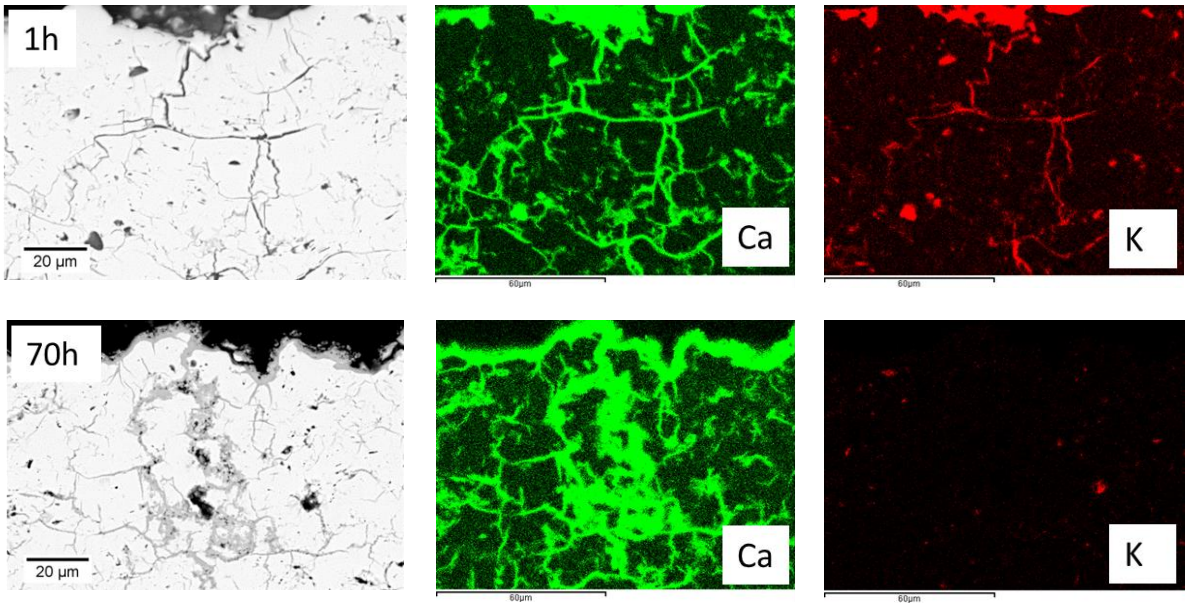

Figure 37: Free-standing DVC YSZ exposures with 0.5CaO-0.5K_2SO_4 (wt%) deposit in dry air at 1100°C. EDS mapping after 1h and 70h reaction times show Ca and K in porous YSZ.

The progression of K and Ca into YSZ was studied in more detail at several different exposure times. A 0.5CaO-0.5K_2SO_4 (wt. %) deposit was reacted in dry air with free-standing YSZ at 1100°C for three different times. EDS scans after each reaction were obtained over narrow areas at increasing depths under the YSZ surface, as described in Figure 38. The EDS scan at each distance was used to identify relative intensities of Ca and K at the depth indicated by the distance to the middle of the corresponding rectangle. The measured relative concentrations of Ca and K as a function of depth in the YSZ are summarized in Figure 39. The EDS scans showed significant levels of K distributed relatively evenly through the YSZ after a 15 minute exposure. The Ca penetration measured by EDS analysis increased at longer times. After 70 h exposure, very little signal from K remained in the YSZ, while the Ca signal was the strongest. The lines in each graph represent the trends at the three different times. Thus, K diminished in amount at a given depth while Ca increased.

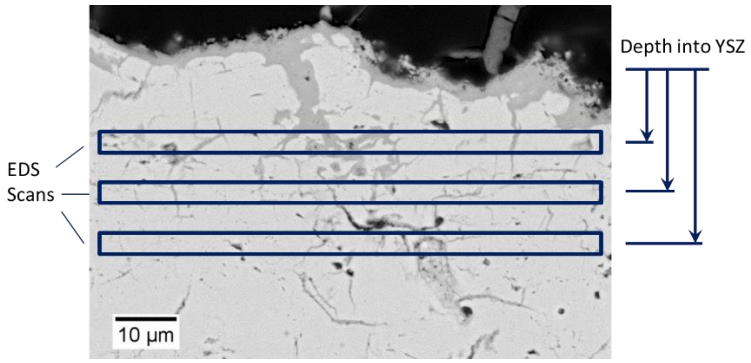

Figure 38: EDS scans conducted in thin rectangular regions parallel to the YSZ surface at increasing distance below YSZ surface were used to quantify relative intensities of Ca and K signals.

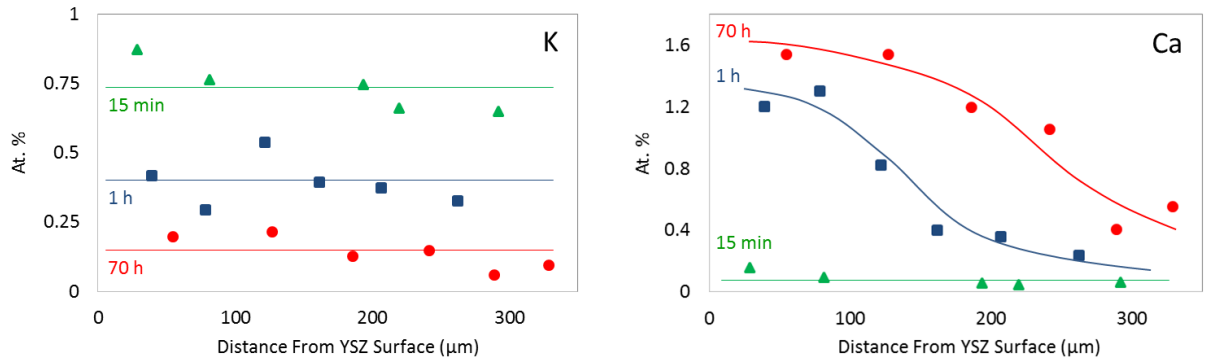

Figure 39: Free-standing YSZ exposures to 0.5CaO-0.5K_2SO_4 deposit in dry air at 100°C results in progression of K and Ca EDS signals into free-standing YSZ. EDS scans at various depths beneath YSZ surface show relative decreasing K presence and increasing Ca presence with longer exposure times.

Internal $CaZrO_3$ formation in the presence of CaO was shown to occur after reactions with CaO+K_2SO_4 deposits at 1100°C. The presence of CaO in actual fly-ash deposits, however, is not common. Rather, the sulfur levels in combustion environments are more likely to promote $CaSO_4$ formation. The equilibrium P_{SO3} level for CaO/$CaSO_4$ at 1100°C is $9x10^{-7}$atm [104]. Thus, even reported low sulfur levels in IGCC systems of 1-2 ppm SO_2 would be enough to stabilize $CaSO_4$. Reaction between free-standing YSZ and a $CaSO_4$-K_2SO_4 deposit was studied at 1100°C. The infiltration from a 0.9$CaSO_4$-0.1K_2SO_4 (wt. %) deposit is shown in Figure 40. The internal $CaZrO_3$ formation in the YSZ was determined through SEM-EDS to be essentially the same as that found with CaO-K_2SO_4 deposit. This indicates that a similar liquid penetration into YSZ cracks was responsible for $CaZrO_3$ formation inside YSZ cracks. Moreover, it reveals the high stability of $CaZrO_3$, with either CaO or $CaSO_4$ being an adequate Ca source.

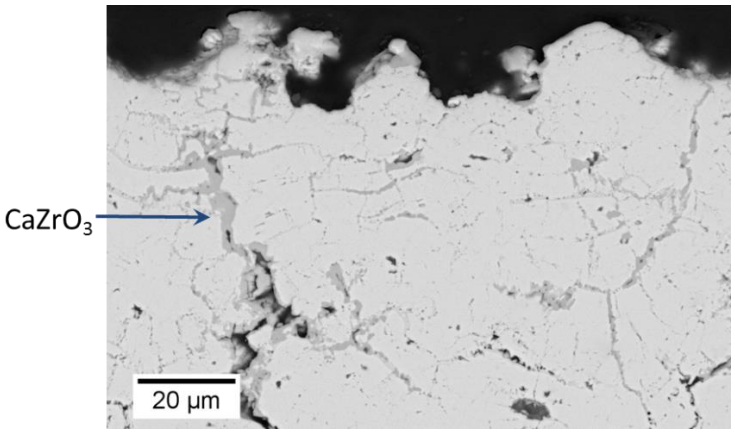

Figure 40: Internal $CaZrO_3$ formation in free-standing YSZ after 72 hour dry air exposure to $0.9CaSO_4$-$0.1K_2SO_4$ deposit at 1100°C.

6.4 SOLUBILITY AND DIFFUSIVITY OF CA^{2+} IN K_2SO_4

The EDS analysis shown in Figure 39 indicated that both K and Ca were present in the infiltrated regions of YSZ after the 1 hour exposure. This result suggests that the liquid K_2SO_4 could be responsible for transporting Ca^{2+} into the YSZ where it eventually reacts with YSZ to form $CaZrO_3$ at longer exposure times. CaO is reported to be essentially insoluble in molten K_2SO_4 [105]; however, some amount of Ca^{2+} dissolution in a liquid K_2SO_4 is necessary for its transport. Solubility of Ca^{2+} in liquid K_2SO_4 was assessed using mixtures of K_2SO_4 and CaO. Figure 41 shows a CaO-K_2SO_4 mixture after heat treatment at 1100°C in dry air followed by an air cool at room temperature. EDS results from the solidified K_2SO_4 after exposure indicated around 1.5 at. % Ca.,

which agrees with the TEM analysis presented in Figure 36. The XRD scan of the mixture after exposure shown in Figure 42 indicates CaO and K_2SO_4. The Al_2O_3 in the XRD is from the crucible.

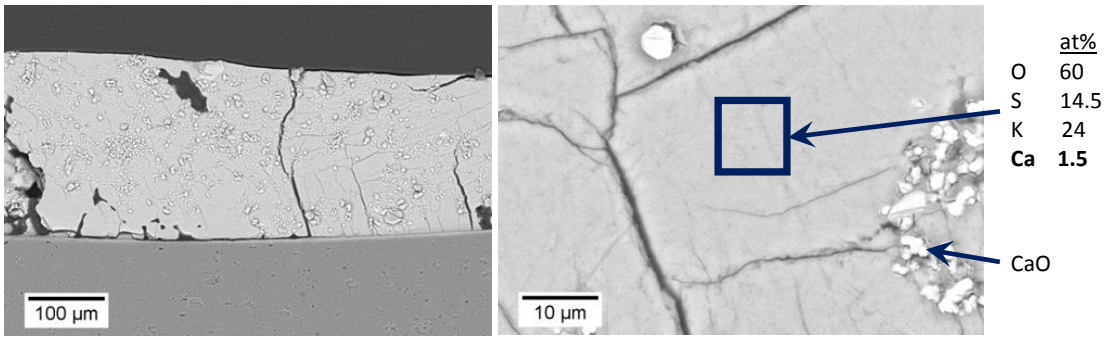

Figure 41: (a) Mixture of $90K_2SO_4$-10CaO (wt. %) that had been heated at 1100°C for 1 hour in dry air, and (b) magnified image showing solidified K_2SO_4 and also some CaO particles. EDS scans detected some Ca^{2+} in the K_2SO_4.

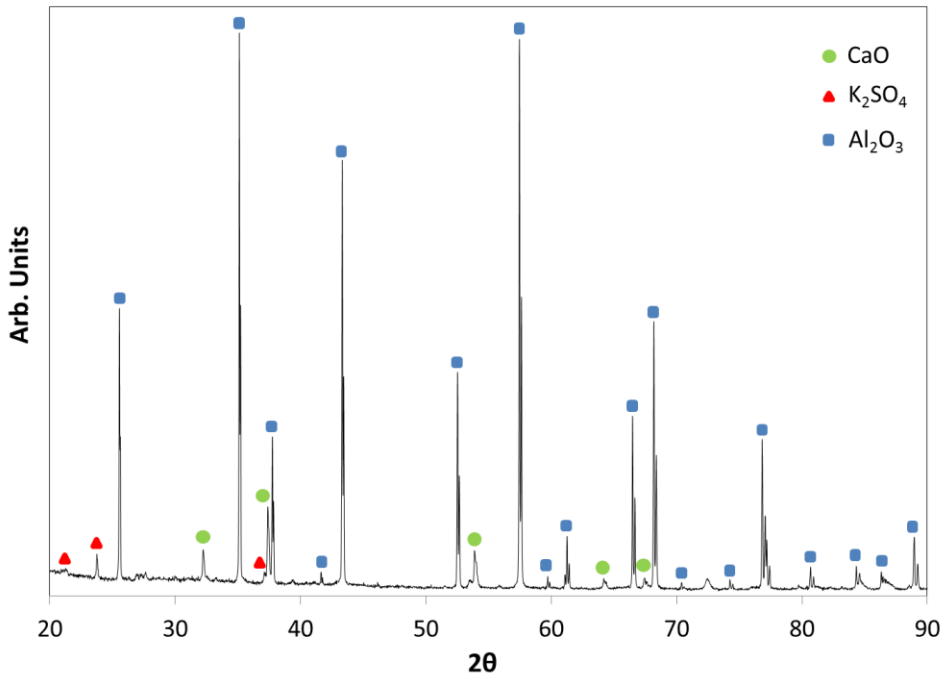

Figure 42: XRD scan on $90K_2SO_4$-10CaO (wt. %) mixture after being heated at 1100°C for 1 hour in dry air and then cooled in lab air. The scan shows distinct peaks corresponding to CaO and K_2SO_4. No $CaSO_4$ was detected. Peaks from Al_2O_3 were detected from the sample crucible.

Figure 43 shows cross-sectional images from a $CaSiO_3$-K_2SO_4 mixture heated at 1100°C in dry air for 1 hour. No measurable solubility of Ca^{2+} in K_2SO_4 was detected. This indicates that K_2SO_4 did not dissolve Ca^{2+} when in contact with the silicate, $CaSiO_3$. The stability of $CaSiO_3$ (ΔG^o= -1857 kJ/mol) [104] is greater than that of $CaSO_4$ (ΔG^o= -1709 kJ/mol) [104] at 1100°C, and the Ca remained bound to the silicate. This suggests that the Ca^{2+} penetration (and subsequent internal $CaZrO_3$ formation) would only be expected in the presence of Ca in the form of either CaO or $CaSO_4$ in the deposit.

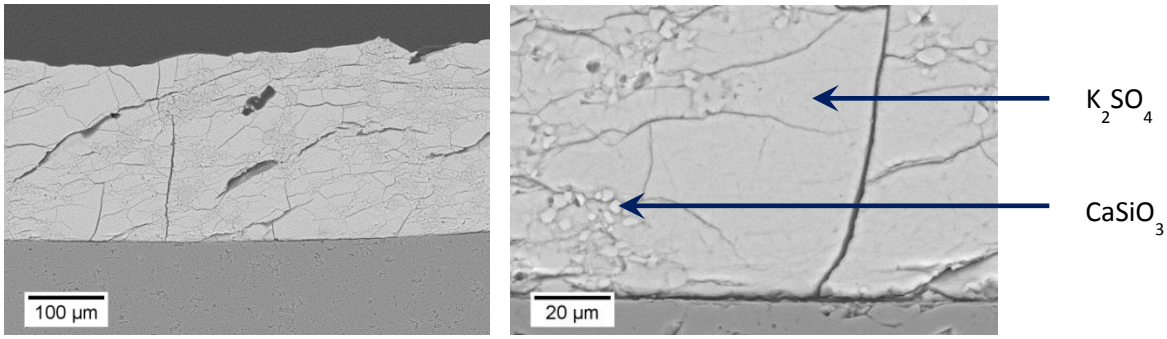

Figure 43: (a) Mixture of $90K_2SO_4$-$10CaSiO_3$ (wt. %) that had been heat treated at 1100°C for 1 hour in dry air, and (b) magnified image. EDS analysis indicated no solubility of Ca^{2+} in liquid K_2SO_4.

The diffusivity of Ca^{2+} in liquid K_2SO_4 was studied by immersing a compressed pellet of CaO in liquid K_2SO_4 for 30 minutes at 1100°C in laboratory air. The dissolution of Ca shown in Figure 44 was then measured via EDS at increasing distance from the solid CaO. The concentration of Ca^{2+} in solution with liquid K_2SO_4 at 1100°C is shown to decrease away from the CaO surface. Measurements were not used within 1µm from the CaO pellet because the proximity to CaO was within the accuracy of the EDS probe.

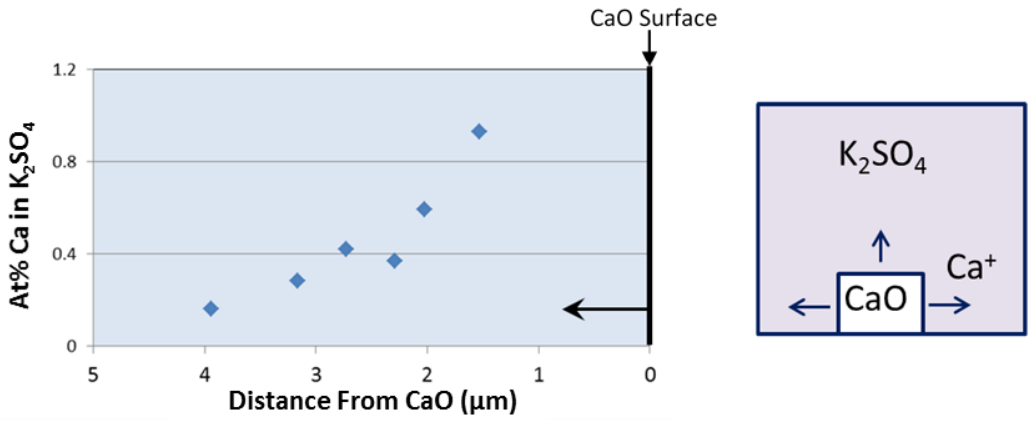

Figure 44: Dissolution of Ca in liquid K_2SO_4 at 1100°C in lab air. The concentration of Ca in K_2SO_4 is shown at increasing distance from a particle of CaO.

The diffusion of Ca^{2+} in liquid K_2SO_4 at 1100°C can be modeled using the equation

$$\frac{C_x - C_o}{C_s - C_o} = 1 - \mathrm{erf}\left(\frac{x}{2\sqrt{Dt}}\right), \tag{6-2}$$

where C_x is the concentration at distance x in the liquid after time t, C_s is the surface concentration of Ca, C_o is the initial concentration of Ca in K_2SO_4, and D is the diffusion coefficient for Ca in liquid K_2SO_4. The diffusion profile from Figure 44 was used with equation 6-2 to calculate a diffusion coefficient, $D \sim 10^{-15}$ m^2/s, using C_s=2.25wt% (extrapolated from Figure 44), C_o=0, and t=900s. The diffusion coefficient is presented in the table for several different depths in Table 9.

The expected diffusion distance after 72h would be approximately 30 µm when estimated using the equation

$$x = 2\sqrt{Dt}. \quad (6\text{-}3)$$

Diffusion of Ca^{2+} from the surface could not account for the extensive depth of $CaZrO_3$ formation observed in these experiments, which typically extended several hundred microns into the YSZ.

Table 9: Calculated diffusion coefficient of Ca^{2+} in K_2SO_4 using data presented in Figure 44 and Equation 6-2.

Distance x from surface (µm)	Measured C_x (wt. %)	Calculated D (m^2/sec)
2.02	0.9	$3.2x10^{-15}$
2.73	0.58	$3.23x10^{-15}$
3.16	0.43	$3.03x10^{-15}$

The diffusion coefficient which was estimated in this work is much lower than typical values (~10^{-9} m^2/sec) reported in the literature [106]. The reasons for such a low calculated value were not explored in detail. Moreover, it was deemed beyond the scope of this work to get a more accurate value. The accuracy of this calculation is limited by the precision of the SEM-EDS measurements. The slow diffusion observed experimentally in this study served to demonstrate

that the diffusion of CaO from the surface would not account for the depth of Ca penetration, and that dissolution must occur quickly in the liquid sulfate at the beginning of the exposure.

6.5 K_2SO_4 EVAPORATION

YSZ exposures to synthetic deposit indicated decreased K over longer times, as discussed in sections 6.2 and 0. This loss of K can be partially explained by evaporation of K_2SO_4 at 1100°C. The measured weight loss of K_2SO_4 due to evaporation at 1100°C is shown in Figure 45. This loss of K_2SO_4 was measured by recording weight loss of a crucible filled with K_2SO_4 after various exposure times. The rate of K_2SO_4 volatilization was affected by the geometry of the crucible used to contain the K_2SO_4 during exposure. The weight loss shown in Figure 46 shows the effect of the sample crucible geometry. The slower volatilization rate was measured from a cylindrical crucible with straight walls. The weight loss from a shallow bowl was much more significant. The slower evaporation rate in the relatively taller cylinder could be a consequence of less surface area and also a greater volume of stagnant air above the liquid sulfate. Another factor in volatilization rate was the mixture of K_2SO_4 with oxides. Figure 47 shows that the addition of SiO_2 and CaO reduced the rate of weight loss from a deposit. The effect of CaO was particularly significant. The mixture of $0.5K_2SO_4$-0.5CaO (wt. %) resulted in dramatically reduced weight loss. The addition of SiO_2 should have resulted in the formation of a liquid silicate which could be more stable than molten

K_2SO_4, thus reducing the rate of volatilization. There was also less K_2SO_4 available to volatilize in these mixtures.

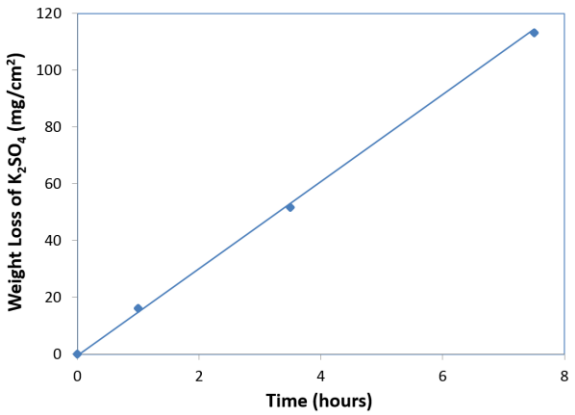

Figure 45: Weight loss of K_2SO_4 due to evaporation at 1100°C.

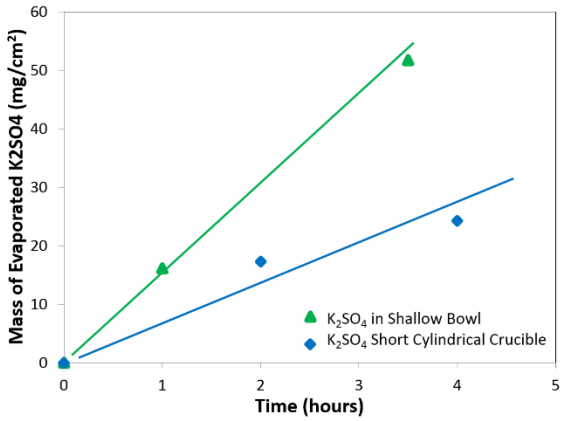

Figure 46: Weight loss of K_2SO_4 due to evaporation at 1100°C. Evaporation rate can be affected by geometry of container.

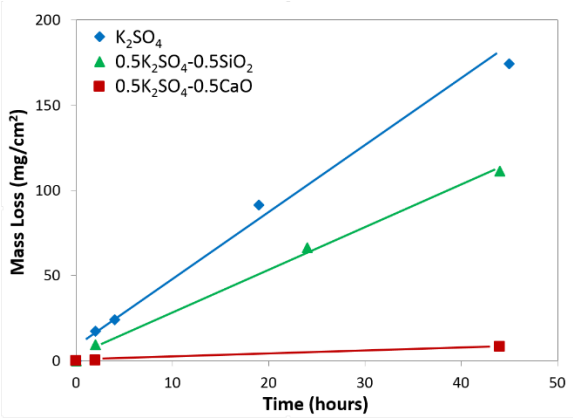

Figure 47: Weight loss due to volatilization at 1100°C. The presence of SiO_2 or CaO can influence the mass loss from a deposit.

The volatilization of K_2SO_4 can occur through dissociative processes according to several reactions described by the reactions:

$$K_2SO_{4\,(s)} = 2K_{(g)} + SO_2 + O_2 \qquad (6\text{-}4)$$

$$K_2SO_{4\,(l)} = 2K_{(g)} + SO_2 + O_2 \qquad (6\text{-}5)$$

$$K_2SO_{4\,(g)} = 2K_{(g)} + SO_2 + O_2 \qquad (6\text{-}6)$$

Previous studies [107, 108] however have reported that weight loss occurs primarily as a result of non-dissociative vaporization via sublimation or evaporation, i.e.,

$$K_2SO_{4\,(s)} = K_2SO_{4\,(g)} \quad (6\text{-}7)$$

$$K_2SO_{4\,(l)} = K_2SO_{4\,(g)} \quad (6\text{-}8)$$

The reduced weight loss measured for the CaO-K_2SO_4 mixture shows that CaO dramatically reduces volatilization from the deposit. Weight loss would primarily be due to volatilization of K_2SO_4. The reduced weight loss could be partially explained by the fact that there was less overall K_2SO_4 to volatilize. The mixture was 0.5CaO-0.5K_2SO_4 (wt. %), and due to the much greater molecular weight of K_2SO_4 (174 g/mol) compared to CaO (56 g/mol), the mixture consisted predominantly of CaO. The weight loss from CaO should be essentially zero because volatilization of CaO at 1100°C would be negligibly small.

Reduced weight loss in the K_2SO_4-CaO mixture would be a consequence of $CaSO_4$ formation through a reaction such as

$$CaO + K_2SO_4 = CaSO_4 + K_2O. \quad (6\text{-}9)$$

The formation of $CaSO_4$, however, was not detected by EDS or XRD. The CaO remained in the CaO-K_2SO_4 mixture and impeded the volatilization of K_2SO_4 from the crucible. The details of this were not explored any further and require further study to explain in more detail.

6.6 Discussion of the Role of CaO

Significant internal reaction-product formation was identified in free-standing YSZ during 1100°C exposures to synthetic deposits in which alkali metal sulfate, K_2SO_4, was incorporated. This type of penetration into the YSZ is not typically observed at temperatures below 1170°C [109] with deposits containing the same oxide constituents (CaO-MgO-Al_2O_3-SiO_2) that were included in the synthetic deposits in this study. Those studies [32, 45, 46], however, do not typically include sulfates such as K_2SO_4. The exclusion of sulfates in CMAS studies is justified because at temperatures ≥1250°C the volatilization of the molten salt would occur quickly before being involved in degradation. At relatively lower temperature of 1100°C, however, volatilization is expected to occur at a slower rate and the molten K_2SO_4 could remain on the sample for sufficient time to infiltrate the YSZ.

Internal formation of a reaction product in YSZ samples from deposits high in CaO involved reaction between Ca^{2+} and ZrO_2. The Ca^{2+} in solution with K_2SO_4 reacted with YSZ to form $CaZrO_3$, and deposits sufficiently high in CaO were capable of sealing the surface with a continuous $CaZrO_3$ layer (as shown in Figure 31). The reaction layer was observed to grow with parabolic kinetics, which can be described by the equation

$$y^2 = k_p(t - t_o), \tag{6-10}$$

where y is the layer thickness at time t and k_p is a rate constant. The plot of the growth kinetics shown in Figure 33 indicated that there was a delay in the initiation of the continuous reaction layer growth during the exposure to CaO. The time t_o represents an incubation period during which YSZ was in contact with the deposit but the continuous $CaZrO_3$ layer had not yet formed. Some $CaZrO_3$ formation is expected during this early stage, however the reaction is not sufficient to produce a continuous solid layer. The reasons for this incubation period are likely related to the lack of even contact between the large CaO particles and the YSZ surface which would result in localized $CaZrO_3$ formation during initial exposure. The details of this, however, were not studied any further in this work. Eventually, the surface reaction layer forms over the YSZ and act as a barrier to any liquid infiltration. The observed delay in continuous reaction-layer formation, however, suggests that during the initial stage of exposure the surface could be susceptible to liquid infiltration.

The onset of internal $CaZrO_3$ formation should occur more quickly than the surface formation because of the more intimate contact between the liquid and YSZ in a crack compared to the discontinuous surface contact with larger solid particles. If one applies the observed kinetics of surface $CaZrO_3$ thickness to the growth rate of $CaZrO_3$ in a crack inside the YSZ, a typical crack approximately 0.5-1um wide would fill with $CaZrO_3$ in approximately 3-5 hours. This would occur before the observed delay in continuous surface formation of approximately 9 hours. Therefore, the observed filling of many cracks inside the YSZ is consistent with the measured delay time in continuous surface $CaZrO_3$. The observed incubation period in which the surface-connected cracks would provide a conduit for liquid penetration would provide enough time for internal $CaZrO_3$ formation to fill many small cracks.

The formation of internal $CaZrO_3$ did not appear to progress significantly into the porous YSZ surface after 1100°C exposures with deposits consisting of only oxides. This was consistent with studies in the literature which do not report liquid formation between these oxides at 1100°C [32]. The addition of K_2SO_4, however resulted in significant $CaZrO_3$ formation in the YSZ. The K_2SO_4 (T_m=1069°C) itself would be molten at 1100°C, and would therefore infiltrate the YSZ until the $CaZrO_3$ surface layer formed and was able to stop further liquid penetration. The observation of significant $CaZrO_3$ formation, however, indicated that Ca^{2+} was being transported into the YSZ along with the liquid K_2SO_4. This could occur in one of two ways: in solution with K_2SO_4 (as Ca^{2+}), or as CaO particles carried in suspension in the liquid K_2SO_4. No CaO particles were observed inside the YSZ, and therefore Ca^{2+} transport in solution with K_2SO_4 was likely.

The measured solubility indicates that Ca^{2+} could enter the open spaces of the YSZ in solution with liquid K_2SO_4 at 1100°C. The high-CaO deposit consisting of 10 wt. % K_2SO_4 contained

a total of 3.5mg, or $2.01x10^{-5}$ moles, of K_2SO_4. The measured solubility of $CaSO_4$ in liquid K_2SO_4 indicated approximately a 1:10 ratio of Ca:K atoms. Thus, if all of the liquid K_2SO_4 had infiltrated the YSZ, it would carry in solution a maximum of $1.3x10^{-6}$ moles Ca, which would produce the same number of moles $CaZrO_3$. By analyzing threshold images of internal $CaZrO_3$ formation, and equating percentage of area coverage to that of volume, the overall concentration of Ca^{2+} in the YSZ was enough to form approximately $5x10^{-5}$ moles of $CaZrO_3$. Therefore, nearly all of the internal $CaZrO_3$ formation could be accounted for by the Ca^{2+} which would be initially transported into the YSZ in solution with liquid K_2SO_4. Some additional Ca^{2+} could also penetrate the YSZ via diffusion through K_2SO_4 near the surface where liquid K_2SO_4 would be in contact with CaO. Diffusion of Ca^{2+} from the surface cannot, however, account for the depth of internal $CaZrO_3$ observed in this work. As previously discussed, the penetration of $CaZrO_3$ observed in this work extended much farther into the YSZ than what would be possible from diffusion alone.

The vehicle for Ca transport was clearly the molten K_2SO_4, which appeared to wet the surface and open cracks of the YSZ. EDS scans showed that the K_2SO_4 was evenly distributed a large distance into the YSZ in a very short time. Considering the overall volume of open cracks, as measured using threshold analysis in the sample (5%), the volume of the sample (0.075 cm^3), along with the total amount of K_2SO_4 (3.5 mg) available in the deposit, approximately 35% of the open space would be filled by liquid K_2SO_4 at 1100°C. This is assuming complete wetting of all surfaces by the liquid sulfate. The condition for wetting of a droplet of liquid forming an angle θ with a surface is given by the equation

$$cos\theta \geq \frac{\Upsilon_{SV}-\Upsilon_{SL}}{\Upsilon_{LV}} \quad (6\text{-}11)$$

Where Υ_{SV}, Υ_{SL}, and Υ_{LV} are the surface energies of the solid/air, solid/liquid, and liquid/air interfaces, respectively. Complete wetting of the YSZ surface by liquid K_2SO_4 would occur when $\theta \rightarrow 0°$. In order for this to occur, the (Υ_{SV}-Υ_{SL}) would be equal to or greater than Υ_{LV}. At 1100°C, the surface energies for YSZ and liquid K_2SO_4 are Υ_{SV}=1.34 J/m^2 and Υ_{LV}=0.14 J/m^2, respectively [110, 111]. Therefore, complete wetting of the YSZ would occur when $\Upsilon_{SL} \leq 1.2$ J/m^2. The surface energy Υ_{SL} is not easily measured, and systems are often modeled only as functions of Υ_{SV} and Υ_{LV} [112]. Surface energies which are reported for the solid/liquid interface are typically lower than those of the solid/air and liquid/air interfaces in equilibrium [112, 113]. Typical values for molten salts on metallic surfaces have been reported around Υ_{SL}~0.1-0.3 J/m^2 [111, 114]. This range of surface energy values is consistent with the complete wetting observed in this study. Previous studies have also reported that molten salts readily wet ceramic coatings (at $T>T_m$ for the salt) and penetrate to the bond coat [63, 74]. Therefore, it is reasonable to expect a low interface energy, $\Upsilon_{SL} \leq 1.2$ J/m^2, for the YSZ/K_2SO_4 interface at high temperatures, which would be consistent with the wetting of the YSZ surface by the liquid sulfate. The wetting of a ceramic surface by molten K_2SO_4 was observed experimentally during volatilization experiments. The solidified K_2SO_4 was observed upon solidification during an air quench to climb a considerable distance along the vertical walls of a cylindrical crucible. This experimental observation (not shown) is consistent with the rapid wetting observed on the ceramic YSZ surface shown in the current study.

In addition to the wetting of the YSZ surface, the wetting of the CaO powder is a necessary condition for Ca^{2+} dissolution and/or transport (as solid pieces) by liquid K_2SO_4. The wettability of bulk powders is dependent on capillary pressure between powder particles [115]. Fast wetting is generally favored with high porosity and large particles [115]. The CaO particles used in the current study exhibit large particle size on the order of 10-20μm, which is consistent with the rapid wetting observed in the solubility experiments.

With longer exposure times, liquid K_2SO_4 would volatilize from larger cracks, which corresponds to the decrease in K signal measured in EDS scans. The observed volatilization rate of K_2SO_4 was reduced in the presence of CaO, which would allow more time for liquid K_2SO_4 to remain in the YSZ and transport Ca^{2+} for $CaZrO_3$ formation. While liquid sulfate was present in the YSZ cracks, it would provide a vehicle for Ca^{2+} transport to crack tips, which in turn would lead to $CaZrO_3$ formation. With sustained $CaZrO_3$ growth in the YSZ, the Ca signal measured by EDS increased as shown in Figure 39. Eventually, nearly all K_2SO_4 would leave the YSZ (through volatilization or and the surface reaction layer would also seal the surface from further liquid infiltration. Both of these events would prevent further internal $CaZrO_3$ formation because the vehicle for Ca^{2+} transport (liquid K_2SO_4) would no longer exist.

The observed incubation period for the formation of a $CaZrO_3$ surface layer could establish a window in which liquid K_2SO_4 could evaporate from the sample before the surface would be sealed by the continuous $CaZrO_3$ layer. The experimentally observed reaction kinetics showed that the continuous $CaZrO_3$ surface layer would form after an exposure time of approximately 9 hours. If one considers the volatilization rate of liquid K_2SO_4 measured in laboratory experiments, and also the total mass of K_2SO_4 in the high-CaO deposit, all of the liquid K_2SO_4 should evaporate

from the YSZ sample in approximately 5 hours. The expected evaporation rate from inside the YSZ cracks would be slower than that of the open crucible. Evaporation, however, could account for some of the substantial decrease in K_2SO_4 with longer exposure time. The remaining K_2SO_4 would also be spread to such an extent that the relative K signal in EDS scans would be reduced over longer times, as was observed in Figure 37.

The infiltration of K and Ca in the YSZ presented in Figure 39 indicated an increase in Ca and loss of K over time, which corresponded to internal $CaZrO_3$ formation in many small YSZ cracks. The sequence of Ca^{2+} penetration into YSZ cracks and subsequent $CaZrO_3$ formation is summarized schematically in Figure 48. Initially, molten K_2SO_4 at 1100°C should wet the YSZ and carry Ca^{2+} into the YSZ in solution. As previously discussed, the liquid sulfate is expected to readily wet the YSZ surface. This early stage is consistent with EDS results presented in Figure 39, which showed K infiltration and very little Ca signal after a 15 minutes exposure. The Ca^{2+} would exist in solution with K_2SO_4, which resulted in relatively weaker Ca mapping in the EDS scans. The $CaZrO_3$ was not expected to form in significant quantities in short exposure times based on results from the isothermal exposures with free-standing YSZ. This was observed in the delay time measured in $CaZrO_3$ growth kinetics, shown in Figure 33. Longer exposure time resulted in more overall Ca signal because of $CaZrO_3$ formation, which filled many small cracks in the YSZ. If one considers the growth kinetics of $CaZrO_3$, a small crack which is 1µm wide would be completely filled by $CaZrO_3$ in approximately 2 hours. The delay in continuous $CaZrO_3$ surface-layer formation of approximately 9 hours would provide enough time for a crack this large to be filled. This delay in surface layer formation also provided the window for K_2SO_4 volatilization, and the subsequent decrease in K signal measured at longer times.

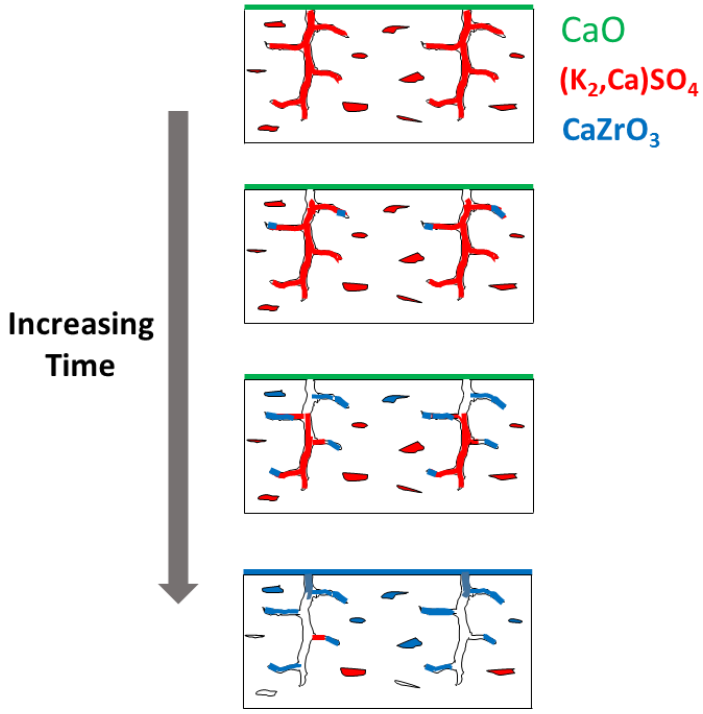

Figure 48: Ca^{2+} transport and resulting $CaZrO_3$ formation. Liquid K_2SO_4 carries Ca^{2+} in solution into cracks at 1100°C. At longer exposure times, Ca^{2+} reacts with YSZ at crack tips to form $CaZrO_3$.

The addition of $CaSO_4$ to synthetic deposits also caused internal $CaZrO_3$ formation in YSZ. Recent studies in the literature have identified TBC damage from $CaSO_4$ [90, 91, 93], which could readily form from CaO in the presence of SO_3 according to the reaction

$$CaO+SO_3=CaSO_4. \quad (6\text{-}12)$$

At 1100°C, the formation of $CaSO_4$ has a change in free energy associated with it of ΔG^o=-158.7 KJ/mol [104] and an equilibrium $P_{SO3}=9x10^{-7}$ atm. This indicates that $CaSO_4$ is very stable and one would expect some $CaSO_4$ formation in an atmosphere containing even a low level of sulfur. Figure 49 shows a $CaO/CaSO_4$ stability diagram for a range of temperatures including 1100°C. The P_{SO3} levels are indicated for the dry air and the $0.2O_2$-100ppmSO_2-CO_2 atmospheres used for exposures in this study. The $CaSO_4$ would be stable at this temperature in the $0.2O_2$-100ppmSO_2-CO_2 atmosphere where the P_{SO3} is above the $CaO/CaSO_4$ equilibrium. When in contact with YSZ cracks, the $CaSO_4$ could also form $CaZrO_3$ via the reaction

$$CaSO_4+ZrO_2=CaZrO_3+SO_3 \quad (6\text{-}13)$$

Which (for unity activity of $CaSO_4$) is accompanied by an equilibrium $P_{SO3}=6.6x10^{-5}$ atm at 1100°C. The $CaSO_4/CaZrO_3$ stability diagram shown in Figure 49 indicates that $CaZrO_3$ would be stable at 1100°C in both the dry air and the $0.2O_2$-100ppmSO_2-CO_2 atmospheres used in the current study. This is consistent with the internal $CaZrO_3$ formation observed in Figure 40 from exposure to a $CaSO_4$-K_2SO_4 deposit. From a thermodynamic perspective, deposits consisting of both $CaO+K_2SO_4$ and $CaSO_4+K_2SO_4$ would result in the same $CaZrO_3$ reaction product.

The P_{SO3} for dry air is below the $CaO/CaSO_4$ stability level, which indicates the impurity level of SO_3 in the dry air atmosphere is below the equilibrium P_{SO3} to form the sulfate. This is consistent with the exposures in dry air in which $CaSO_4$ formation was not observed. IGCC systems utilize syngas, which is capable of reducing total sulfur to levels below 20 ppm [5]. These low sulfur levels in IGCC systems indicate that CaO could be thermodynamically stable at 1100°C as opposed to conventional coal-fired power plants in which $CaSO_4$ is typically the predominant Ca-containing species because of the relatively higher P_{SO3} levels in combustion atmospheres.

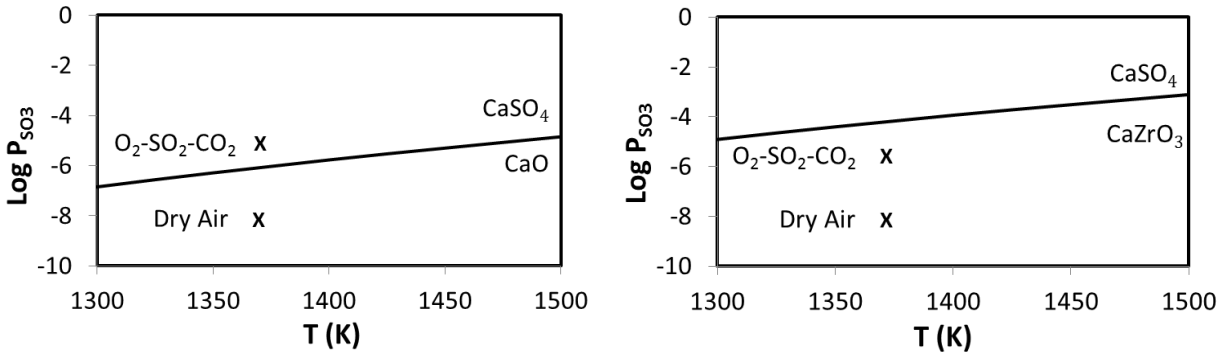

Figure 49: Stability diagrams for (a) $CaO/CaSO_4$ and (b) $CaSO_4/CaZrO_3$ formation

7.0 THE ROLE OF SIO_2

Silica is a common constituent in fly ash produced from coal and biomass is [16, 94]. Exposures to commercial fly ash discussed in Chapter 4 showed YSZ degraded by an internal reaction product which contained SiO_2. Synthetic deposits containing high levels of SiO_2 comprised of only oxides were tested with free-standing YSZ in dry air at 1100°C. The SiO_2 was also not observed to react with the YSZ surface. Oxide deposits containing high levels of SiO_2 were also not observed to cause internal formation of any reaction product in YSZ cracks. The internal reaction caused by the commercial fly ash likely involved other ash constituents. The effects of K_2SO_4 (a common fly-ash constituent) in the internal degradation of YSZ from high-SiO_2 deposits was studied.

7.1 LIQUID INFILTRATION IN THE PRESENCE OF K_2SO_4

Free-standing YSZ was reacted at 1100°C in dry air with the high-SiO_2 deposit detailed in Table 10. The EDS mapping in Figure 50 indicates that large amounts of Si and K penetrated YSZ

cracks up to around 100 µm into the sample after a 72 hours exposure in dry air. This result was different from internal reaction formed from high-CaO deposit, which indicated very little K signal after 72 hours. The presence of a strong Si and K signal after long exposure times suggests that the penetration was the result of liquid silicate formation. This is consistent with the fact that any potassium silicate which would form from K_2O and SiO_2 would be liquid at 1100°C [116].

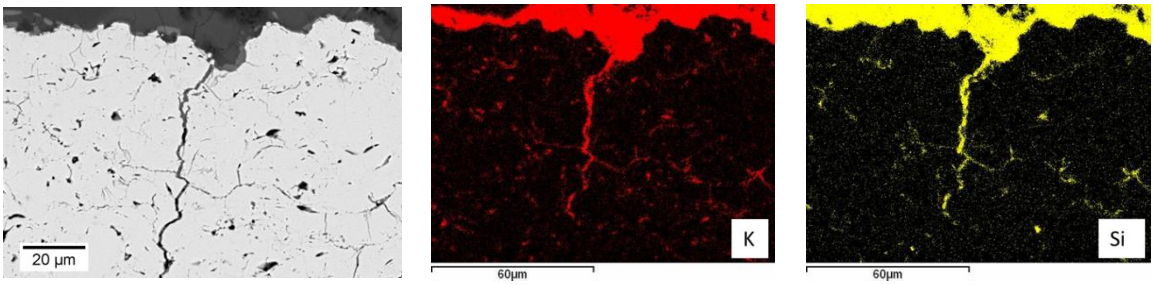

Figure 50: (a) Free-standing DVC YSZ reacted in dry air with SiO_2-rich synthetic ash for 72 hours at 1100°C and EDS mapping of (b) K and (c) Si showing penetration into cracks below YSZ surface.

Table 10: Composition (mol %) of high-SiO_2 synthetic ash deposit.

CaO	SiO_2	Al_2O_3	MgO	Fe_2O_3	K_2SO_4
12	55.5	16.5	8	4	4

Infiltration of free-standing YSZ after a 72 hour dry air exposure to high-SiO_2 synthetic ash at 1100°C was studied using FIB milling followed by TEM imaging, Figure 51 shows a crack in the YSZ 40µm below the surface which was completely filled with a product rich in K and S. These

results were consistent with SEM-EDS analysis of the same sample. EDS scans at several locations in Figure 51(b) show that the YSZ crack was filled with a silicate consisting of two distinct regions having molar K:Si ratios of 1:4 and 1:2. This silicate formation will be discussed in a later section. In addition to large cracks filled with liquid silicate, some segregation of ash constituents at grain boundaries is also shown by arrows in Figure 51(b). This was consistent with previous studies, which showed that SiO_2 will segregate to grain boundaries and degrade the YSZ [117]. Degradation would involve depletion of Y from the YSZ which typically leads to destabilization from the t' phase. No Y-depletion, however, was observed in this study.

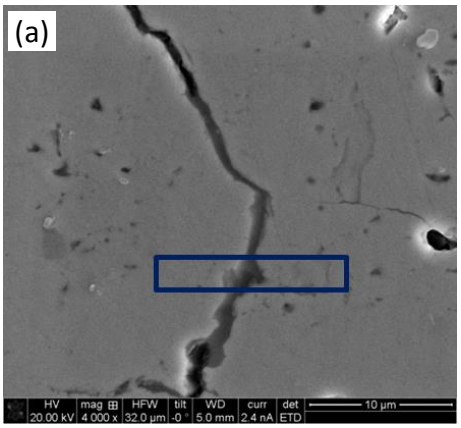

	1	2	3	4	5
O	63	60	48	53.5	52.5
Al	8	0.25		1	1.5
Si	22	23		2	3
K	5	10.25	31		
Fe	2		3.5		0.5
Zr		6.5	1	36	37.5
Ca			0.5	1	0.5
S			16		
Y				4	3
Mg				1	1

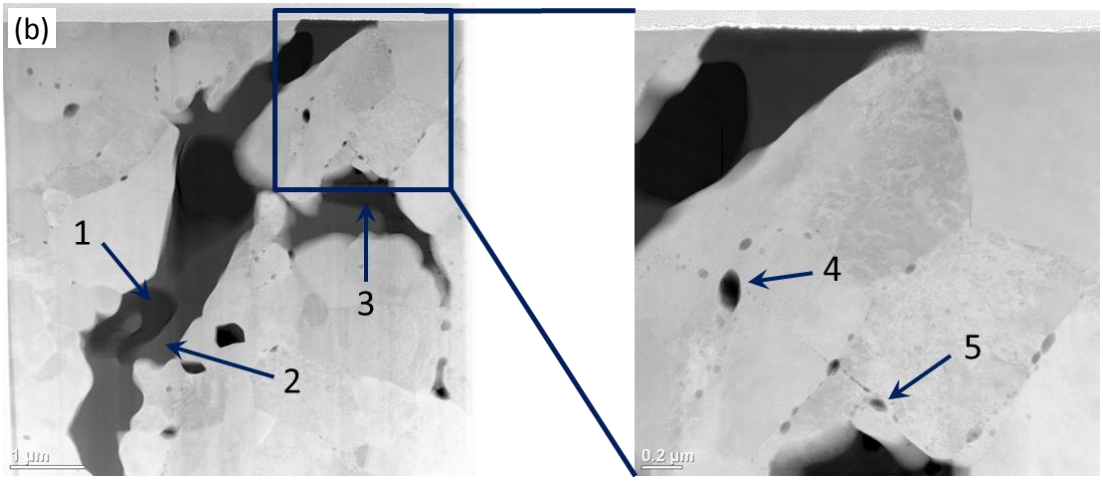

Figure 51: (a) Location of FIB milling at infiltrated YSZ crack. (b)TEM images show crack filled with potassium silicate. EDS data shows different K:S ratios in liquid silicate and grain boundaries affected by ash. (EDS in at. %)

7.2 SOLUBILITY EXPERIMENT WITH SIO_2 AND K_2SO_4

The filling of many YSZ cracks at 1100°C from the high-SiO_2 deposit involved the infiltration of liquid silicate into open spaces of the YSZ. The reaction product which formed upon cooling from 1100°C contained high levels of Si and K. In order to study silicate formation from SiO_2 and K_2SO_4, a mixture of $0.90K_2SO_4$-$0.10SiO_2$ (wt. %) was heated at 1100°C in dry air for 1 hour in an alumina crucible. The resulting mixture is shown in Figure 52 after air cooling to room temperature. The K_2O-SiO_2 phase diagram shown in Figure 53 indicates extensive liquid formation at 1100°C. Separation of a liquid into distinct compounds would be expected upon cooling. The mixture appeared to have solidified upon cooling and separated into two distinct regions: a region of SiO_2 (indicated by the molar K:Si:O ratio 1:10:20) and a silicate corresponding closely to $K_2Si_4O_9$ (indicated by the molar K:Si:O ratio of 1:3:6) shown in Figure 52(c). The details of this liquid silicate formation merit further study. For the purpose of this work, these results show that the presence of K_2SO_4 and SiO_2 leads to significant liquid formation.

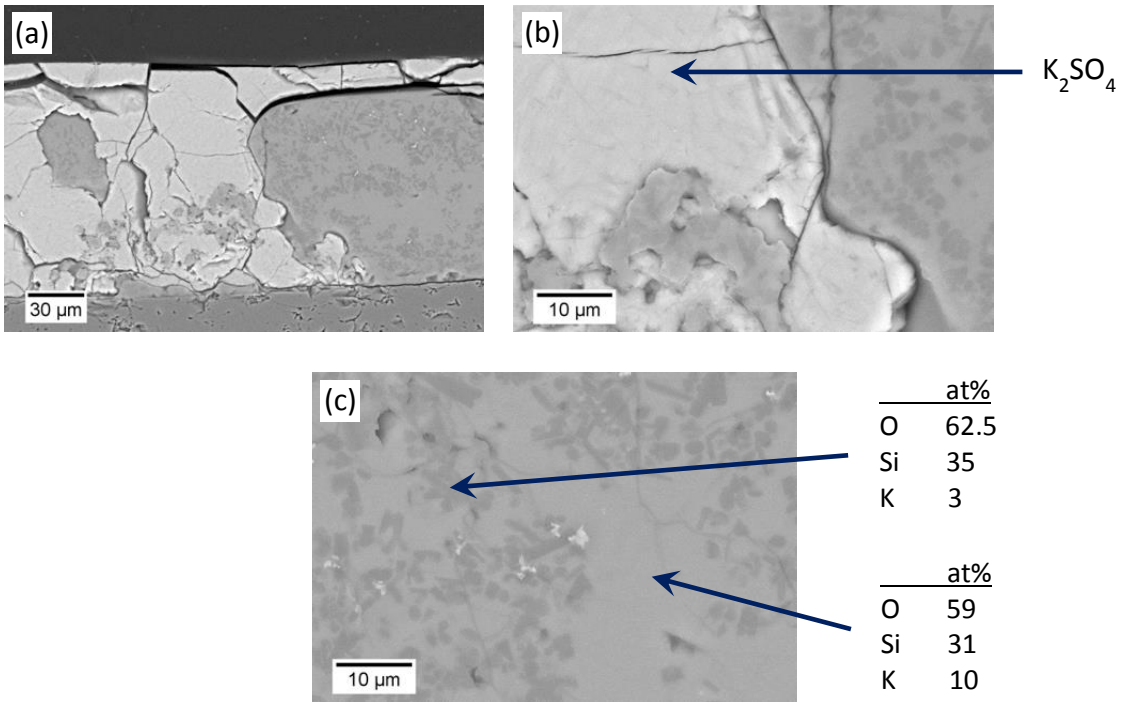

Figure 52: (a) A deposit consisting of $0.90K_2SO_4$-$0.10SiO_2$ (wt. %) heat treated for 1 hour at 1100°C in dry air. (b) Closer inspection of K_2SO_4 shows distinct K_2SO_4 and SiO_2 regions. (c) Much of the SiO_2 and K_2SO_4 appear to have reacted to form a liquid at 1100°C.

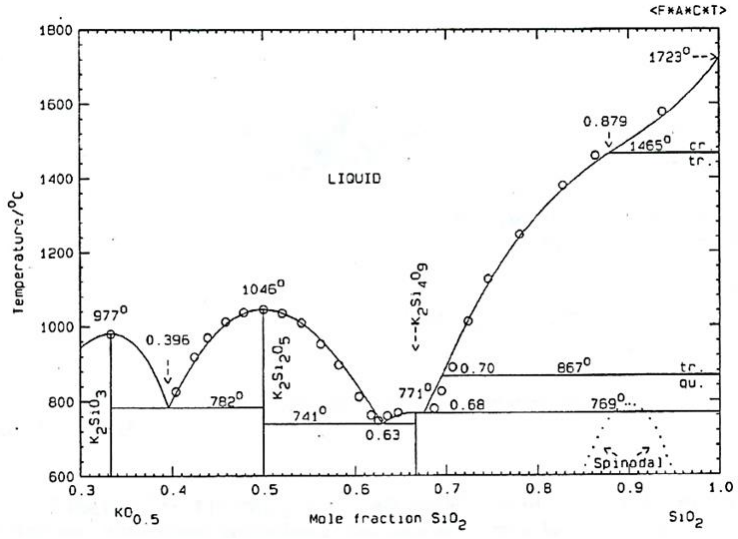

Figure 53: Binary phase diagram of the K_2O-SiO_2 system shows several potassium silicate compounds. Liquid formation is expected at 1100°C [116].

7.3 DISCUSSION OF SIO_2 EFFECTS

Exposures to the high-SiO_2 deposit resulted in liquid infiltration of the free-standing YSZ sample. Many cracks in the YSZ were filled with a product which was determined by EDS to contain high amounts of Si, K, and O. Thus, the liquid formed during exposure to high-SiO_2 ash was deduced to have involved the formation of $K_2Si_4O_9$ from K_2SO_4 and SiO_2 in the deposit. In accordance with the phase diagram in Figure 53, this silicate would be expected to exist as a liquid at 1100°C. The EDS mapping in Figure 50 showed strong signals from both K and Si even after long exposure times. This indicates that, unlike with the high-CaO ash exposures, the potassium remained by forming the silicate.

The K_2O-SiO_2 phase diagram shows an extensive range of liquid stability at 1100°C. K_2O itself would not exist in any measurable quantities in these experiments due to the formation of K_2SO_4,

$$K_2O+SO_3=K_2SO_4. \quad (7\text{-}1)$$

The equilibrium $P_{SO3}=1.3x10^{-17}$ atm for K_2SO_4 formation at 1100°C indicates that the sulfate is very stable. This sulfate could react with the silica in the deposit to form a silicate such as

$$K_2SO_4+SiO_2=K_2SiO_3+SO_3. \quad (7\text{-}2)$$

The equilibrium $P_{SO3}=5.5x10^{-7}$ atm for K_2SiO_3 formation at 1100°C shows that the silicate is very stable in low P_{SO3} atmospheres.

The silicate liquid which penetrated YSZ cracks at 1100°C appeared to have separated into two distinct phases upon cooling. A potassium silicate which would exist as a liquid at 1100°C could separate into two silicate compounds upon cooling. The K:Si:O ratios measured by EDS were 1:4:12 and 1:2:6 for the two distinct silicate regions. These molar ratios did not correspond to any two silicates from the SiO_2-K_2O phase diagram. The liquid observed in these exposures, therefore, cannot be explained by a silicate comprised only of K_2O and SiO_2. Examination of the EDS data in Figure 51 , however, also indicates a significant amount of Al in one of the two phases, indicated in Figure 51 by a K:Al:Si:O ratio of 1:1.5:4:12.5. The second phase was characterized by a K:Si:O ratio of 1:2:6. The phase diagram shown in Figure 54 shows liquid formation between potassium tetrasilicate, $K_2Si_4O_9$, and potash feldspar, $K_2Al_2Si_6O_{16}$, at 1100°C. A ternary phase diagram indicates that melting in the SiO_2-K_2O-Al_2O_3 system can occur at temperatures ≤1100°C. Upon cooling, this liquid melt could separate into the two distinct phases which corresponds with the EDS data in Figure 51.

The reaction of K_2SO_4 with SiO_2 at 1100°C could form amorphous phases as well as crystalline phases [116, 118]. XRD scans of a binary K_2SO_4-0.1SiO_2 (wt. %) mixture after heating to 1100°C in lab air followed by air quench showed the formation of crystalline phases. The phases were not examined any further, but the existence of XRD peaks indicated that crystalline phases could form upon cooling.

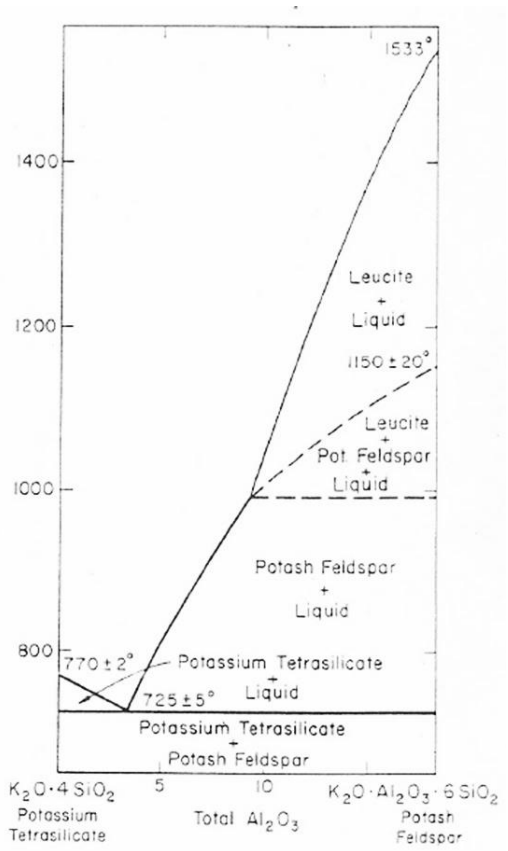

Figure 54: Phase diagram from the K_2O-SiO_2-Al_2O_3 system showing liquid formation between two potassium silicates [119].

The high-SiO_2 synthetic ash resulted in a rather significant amount of liquid-silicate infiltration in the YSZ at 1100°C. Investigation of regions of YSZ near infiltrated cracks showed segregation of ash constituents along grain boundaries in the YSZ. This could cause some destabilization of the YSZ, which would be detrimental to TBC lifetime. Grain-boundary segregation of silica impurities in YSZ has been shown to degrade 7YSZ in other studies [120]. This type of degradation would be accompanied by Y-depleted regions of YSZ which would cause destabilization of the t' phase. No such Y-depletion was observed in the EDS analysis. This indicates that the activity of Y_2O_3 in the YSZ was too low to react with the ash constituents at the grain boundaries.

8.0 DEPOSIT VARIABLES

Experimental variables were studied to examine the effect of each on $CaZrO_3$ formation with free-standing YSZ. The purpose of these experiments was to examine the reliability of laboratory tests in modeling degradation from real fly-ash deposits.

8.1 EFFECT OF HEAT TREATMENT AND K_2SO_4 ON $CAZRO_3$ GROWTH

Fly-ash deposits typically consist of particles which contain fused constituents. The fusing of constituents from an IGCC ash is the result of the high-temperature, high-pressure gasification process [96]. The fly-ash particles which become entrained in the gas consist of compounds formed on cooling. This is different from the synthetic deposits discussed in chapters 5 and 6, which consisted of oxide constituents which were mixed together at room temperature and then heat treated at 1200°C for 24 hours. After the heat treatment, a minor constituent such as K_2SO_4 was added to the synthetic deposit. Therefore, because the synthetic ash did not experience the same thermal history as a real fly ash, it was necessary to show that the YSZ degradation observed

could also occur with real fly ash. Several different fly ash preparation techniques were tested in order to determine the effects of initial ash condition on reaction with free-standing YSZ.

The high-CaO synthetic deposit presented in Table 7(d) was prepared by three different methods: 1) mixing oxides together with no heat treatment (NHT); 2) heat-treating the deposit for 24 hours at 1200°C in dry air (HT); and 3) heat-treating the deposit for 1 hour at 1500°C in dry air (fused). The results discussed in chapters 5 and 6 were obtained on deposits which had been heat-treated at 1200°C before YSZ exposure. The fused ash would be the closest model of a real fly ash which could form at very high temperatures (~1500°C) during gasification. Therefore, the NHT and fused deposits should represent two extremes of laboratory-prepared ash in terms of thermal history, with the majority of the results obtained in this work being between those two extremes.

The thickness of the $CaZrO_3$ surface layer is compared in Figure 55 for 72 hours dry air exposures at 1100°C, both with and without K_2SO_4 addition. In the absence of K_2SO_4, all deposits produced similar reaction layers of comparable thickness. The $CaZrO_3$ surface layer formation was not significantly affected by the thermal history of the deposit. However, it should be noted that the heat-treated deposit consistently produced a slightly thinner surface layer (both with and without K_2SO_4 addition) compared to NHT and fused deposits. The addition of K_2SO_4 resulted in some difference in reaction layer thickness for all three preparation techniques. For each deposit, the $CaZrO_3$ layer thickness increased with the addition of K_2SO_4. The increase in thickness with the NHT and HT deposits were very similar when K_2SO_4 was added (see Figure 55). The addition of K_2SO_4 to the fused ash, however, resulted in a more dramatic increase in $CaZrO_3$ surface layer thickness. The thickness of the $CaZrO_3$ shown in Figure 56 was substantially

increased with the addition of K_2SO_4 to the fused ash. This will be discussed further in another section.

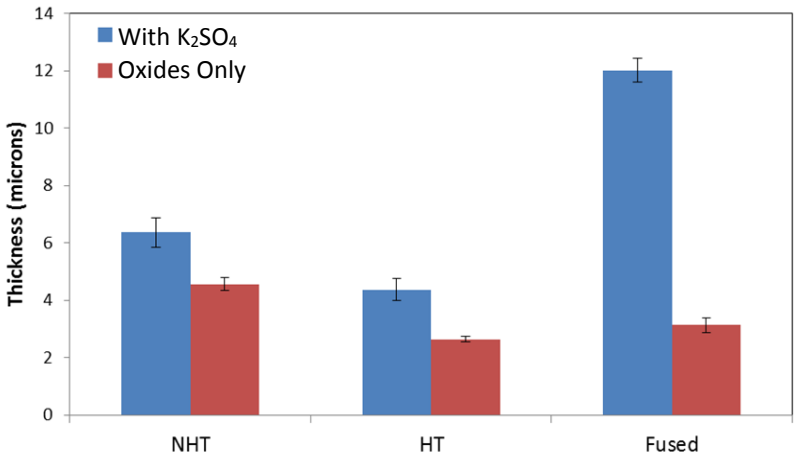

Figure 55: $CaZrO_3$ surface reaction layer thickness after 72h exposures in dry air at 1100°C. Surface layer thickness is compared for three different ash preparation techniques, both with and without K_2SO_4 addition.

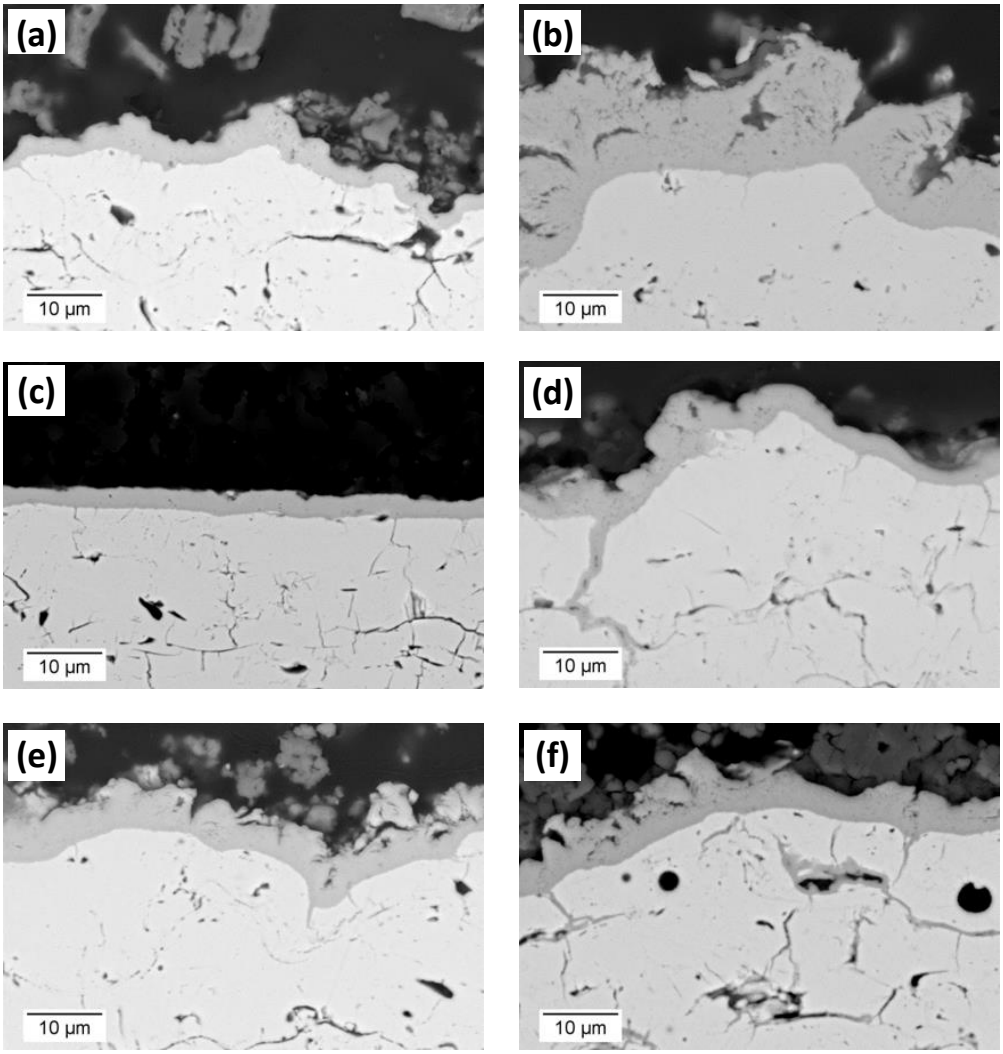

Figure 56: $CaZrO_3$ layer on YSZ surface after reaction in dry air at 1100°C with the same high-CaO synthetic ash described in Table 7(d) that was prepared differently before exposure. Reactions are shown for synthetic deposit which was (a) fused and crushed. (b) fused and crushed then mixed with 10 wt% K_2SO_4, (c) heat treated and crushed, (d) heat treated and crushed then mixed with 10wt% K_2SO_4, (e) not heat treated, and (f) not heat treated and mixed with 10 wt% K_2SO_4.

Two different synthetic fly-ash deposits, fused and NHT, are shown in Figure 57 after 72 hours dry air reactions with YSZ at 1100°C. The fused deposit consists of only oxide constituents, and contained no detectable levels of K_2SO_4. The NHT deposit, however, contained K and S, which

indicates the existence of sulfate(s) in the deposit after 72h exposure. The 1:1 molar ratio of K:S suggests that the sulfur is not entirely accounted for by K_2SO_4. This could be explained by the formation of $CaSO_4$ from the reaction with CaO in the deposit. The presence of sulfate components after exposure is consistent with previous results involving CaO and K_2SO_4 in which very little weight loss was observed after 1100°C heat treatment (see Figure 47).

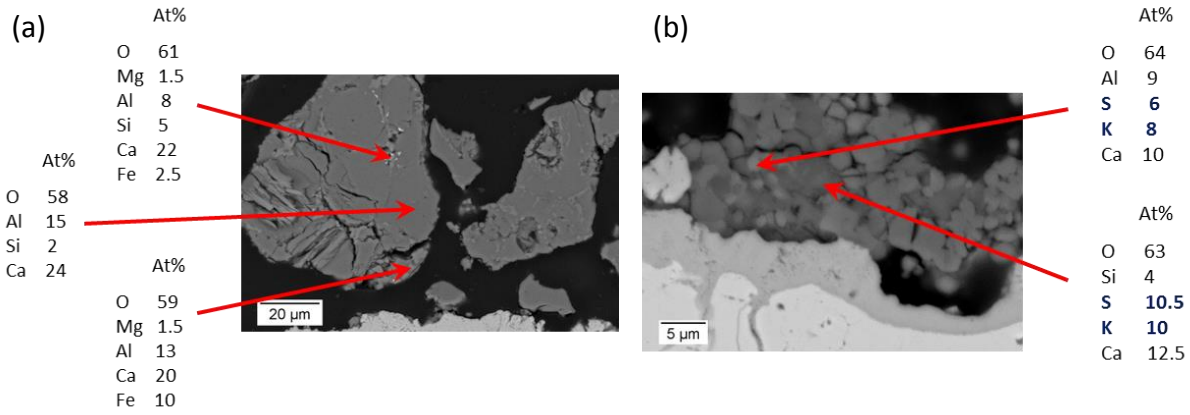

Figure 57: Two synthetic ashes of identical initial composition described in Table 7(d) with different thermal histories, after 72 hour dry air reactions with YSZ at 1100°C. (a) Oxide components were fused at 1500°C and then crushed before mixing with K_2SO_4. (b) The same oxide components were mixed together and did not experience any heat treatment before mixing with K_2SO_4.

The morphology of the surface $CaZrO_3$ layer was not significantly affected by the addition of K_2SO_4 for the HT and NHT deposits. The reaction layers shown in Figure 56 indicate that, other than a slight increase in overall thickness, the addition of K_2SO_4 did not significantly change the $CaZrO_3$ layer which was formed. The addition of K_2SO_4 to the fused ash, however, did affect the

morphology of the $CaZrO_3$ layer formed at the surface. In addition to being much thicker overall, the surface layer consisted of many open pockets absent of CaO. SEM-EDS analysis indicated that these regions contained solidified K_2SO_4. This could have occurred because the surface layer grew very fast and enclosed some molten K_2SO_4. These pockets of K_2SO_4 were excluded in the threshold analysis, and the overall thickness reported in Figure 55 represents only the $CaZrO_3$ on the YSZ surface. The $CaZrO_3$ itself, between the pockets of K_2SO_4, was nearly identical to the zirconate layer which formed without K_2SO_4.

8.2 EFFECT OF HEAT TREATMENT ON INTERNAL $CAZRO_3$ FORMATION

The overall $CaZrO_3$ formation after 72h dry air exposures at 1100°C is shown in Figure 58. The internal formation of $CaZrO_3$ reaction product was determined from micrographs taken at locations in a straight line through the thickness of the YSZ, so that areas near the surface and farther away were equally represented. Micrographs at the surface were not included (i.e., surface $CaZrO_3$ layer thickness was not represented), so that the results show only $CaZrO_3$ which formed in cracks internal to the YSZ. At each location, image threshold analysis was used to calculate the percentage of the area which was accounted for by $CaZrO_3$, similar to the method shown in Figure 33. Overall internal $CaZrO_3$ formation was similar for the heat-treated and fused deposits. Thus, the internal $CaZrO_3$ formation discussed in chapter 5 was similar to what would be expected from a fused ash. However, the penetration of internal $CaZrO_3$ was measured to be

more significant in the deposit which was not heat treated. This difference in NHT deposit confirmed the necessity to heat treat synthetic deposits in order to have infiltration which could be expected from fused deposits. The heat treatment of the oxides may be expected to produce silicates in the deposit which would not transport Ca^{2+} as readily into the YSZ compared to the pure oxides in NHT deposits. This is consistent with the result of the $CaSiO_3$-K_2SO_4 exposure shown in Figure 43; SEM-EDS analysis of the $CaSiO_3$-K_2SO_4 mixture after heating indicated no measurable solubility of Ca^{2+} in the silicate.

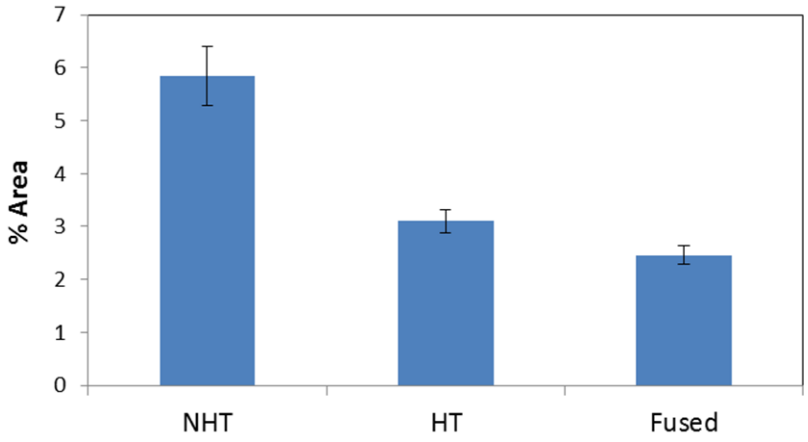

Figure 58: Internal $CaZrO_3$ formation in YSZ from high-CaO synthetic ash that was prepared with three different preparation techniques before being mixed with K_2SO_4. The same ash composition was not heat treated (NHT), heat treated (HT), and fused before addition of K_2SO_4 and subsequent exposure with YSZ at 1100°C in dry air.

8.3 EFFECT OF DEPOSIT RE-APPLICATION

Turbine components are constantly exposed to fly-ash buildup as they are continuously subjected to hot gases which contain particulates. The results presented in sections 5-7 were obtained after a single deposition of ash onto YSZ samples. A TBC used in an actual turbine could experience the loss of a deposit, and/or re-application of new deposit throughout its lifetime. $CaZrO_3$ formation was examined after multiple deposit applications in order to identify any effects from multiple deposit exposures. Figure 59 compares the thickness measured after a single deposit application to the same length exposure with three separate deposit applications. The $CaZrO_3$ layer thickness results did not indicate a substantial dependence on overall surface layer thickness.

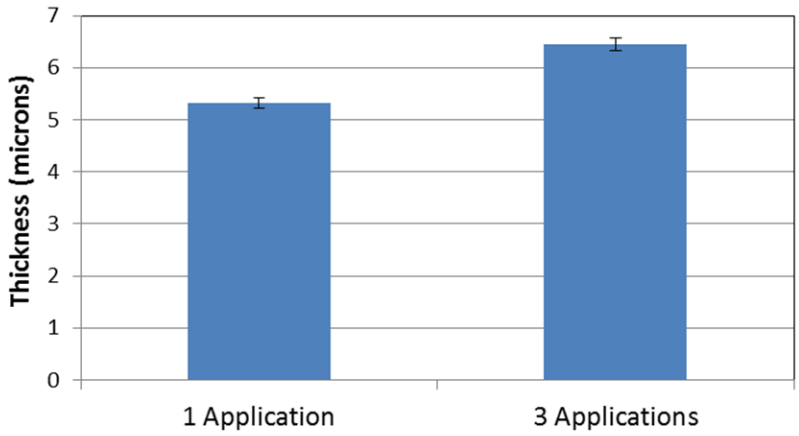

Figure 59: Surface $CaZrO_3$ layer thickness formed between YSZ and high-CaO synthetic ash after a single application of ash compared to that with 3 different applications of ash. Both exposures were at 100°C in dry air for a total of 72 hours.

The area percentage of $CaZrO_3$ measured with image threshold analysis is shown in Figure 59 after a single high-CaO deposit application and compared to that of three separate applications. The relative amount of open cracks for the same exposure without deposit is also shown to provide a baseline. Relative internal $CaZrO_3$ formation through the YSZ thickness indicates that multiple deposit applications did not have a measurable effect on overall penetration distance into YSZ cracks.

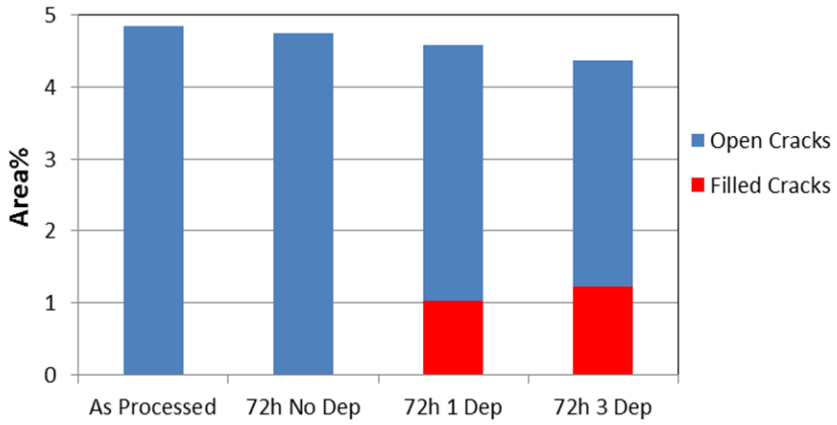

Figure 60: Image analysis results in YSZ measured through the thickness of three different samples. The area of open cracks and cracks filled with $CaZrO_3$ was measured for as-processed YSZ, Free-standing YSZ that had been heat treated without deposit, YSZ that was exposed to a single application of high-CaO synthetic ash, and also a sample that was reacted while high-CaO synthetic ash was applied at three equally-spaced intervals.

8.4 DISCUSSION OF DEPOSIT VARIABLES

Experiments were conducted with fused synthetic ash and mixed oxides which were not heat treated. The fused deposit should closely model a real fly ash, with the exception of alkali species (K and/or Na). Because K_2SO_4 was added after the heat treatment, compounds which could form between alkali metal sulfates and oxides ($CaSO_4$ and/or silicates involving K) at high temperatures were not initially represented in these experiments. These compounds could exist in real fly-ash deposits. K_2SO_4 which was added before heat treatment could have been largely lost due to volatilization at high temperatures (≥1100°C). The high rate of K_2SO_4 volatilization at 1100°C shown in Figure 45 would result in the loss of 100mg of K_2SO_4 on a $1cm^2$ sample in 7 hours. The expected rate of volatilization at the 1200°C temperature used for ash heat-treatment would be higher.

The same $CaZrO_3$ reaction layer was produced on the YSZ surface with fused ash, heat-treated ash, and mixed oxides (not heat treated). This showed that the heat-treated synthetic ash was replicating a reaction which could be expected with an actual fly ash. This was also verified by studies in the literature which showed $CaZrO_3$ formation on actual turbine blades which had been removed from service [91, 93]. The $CaZrO_3$ surface layer thickness was increased with K_2SO_4 addition. This is inferred to be a consequence of the presence of a molten phase. The liquid would wet the surface, and it would also provide a conduit through which Ca could be transported to the surface (via Ca^{2+} diffusion), effectively increasing the contact area between Ca and ZrO_2 and facilitating $CaZrO_3$ growth.

The heat treatment of the synthetic deposit at 1500°C before reaction with YSZ resulted in a synthetic ash which was capable of producing a substantially thicker $CaZrO_3$ surface layer at 1100°C. The micrographs shown in Figure 57 indicate differences in the deposits after the 72 hours reaction. After reaction, the fused deposit consisted of only the oxide constituents, and contained neither K_2SO_4 nor any compounds consisting of K or S. This deposit should have consisted primarily of silicates which did not react substantially with K_2SO_4. After reaction with the YSZ, some K_2SO_4 which was added to the fused deposit remained near the YSZ encased in the $CaZrO_3$ layer (this can be seen in Figure 56(b)). This suggests that, rather than reacting with the deposit, the molten K_2SO_4 spread along the YSZ surface to provide a medium for transporting Ca evenly to the YSZ surface. The NHT deposit, however, contained compounds which included K and S. Some of the K_2SO_4 reacted with the NHT deposit and less molten sulfate would be available to act as a conduit for Ca^{2+} transport at the surface to facilitate $CaZrO_3$ growth.

YSZ exposures with heat-treated and fused deposits resulted in similar internal $CaZrO_3$ formation. The fused deposit should be similar to an actual fly-ash deposit which forms at high temperatures. This indicates that the heat-treated deposit (which was used to generate results shown in previous sections) accurately replicated $CaZrO_3$ formation which might be expected from a real fly ash. The penetration of $CaZrO_3$ into the YSZ was more significant with the deposit which was not exposed to any heat treatment prior to YSZ testing. The CaO in the NHT deposit would not initially be fused with any other ash constituent, and thus could be more readily dissolved by the liquid K_2SO_4 during exposure at 1100°C. This shows that the preparation of the deposit prior to YSZ exposure can affect overall infiltration.

Re-application of deposit did not significantly increase overall internal $CaZrO_3$ formation. The continuous $CaZrO_3$ layer which formed on the surface would seal the surface and prevent further liquid infiltration from subsequent re-application of deposit. This provides confirmation that a single application of a deposit should sufficiently reproduce penetration of reaction product into the YSZ expected from a high-CaO deposit capable of forming $CaZrO_3$, in isothermal conditions.

9.0 THERMO-MECHANICAL CONSEQUENCES OF SYNTHETIC FLY ASH

The literature reports that liquid compounds are not formed in CMAS deposits below ~1250°C [45]. This is true of the oxide constituents; however, it has been shown in this research that the addition of sulfates can produce liquid phases at temperatures lower than 1250°C. Hence, these CMAS-based deposits with addition of K_2SO_4 could have detrimental effects on TBC lifetimes at temperatures lower than what has previously been considered a dangerous regime.

Two different molten phases involving K_2SO_4 were identified at 1100°C in dry air. Deposits which contained a high concentration of CaO produced extensive formation of a $CaZrO_3$ reaction product in YSZ cracks, whereas high levels of SiO_2 caused infiltration of a liquid potassium silicate. Both types of penetration into YSZ could damage TBCs which experience thermal cycling due to detrimental effects on mechanical properties of coatings. Thermo-mechanical consequences of these deposits on TBC performance at 1100°C are considered in the following sections.

9.1 SURFACE REACTION LAYER EFFECTS

Free-standing YSZ exposure to high-CaO deposits produced $CaZrO_3$ reaction layers which were continuous along the YSZ surface after 72 hours exposure in dry air. Potential effects of the surface layer on TBC lifetime were tested by subjecting complete TBCs with a pre-formed $CaZrO_3$ layer to thermal cycling in laboratory air at 1100°C, using a bottom-loading furnace. The pre-formed layer was the result of a 72 hour isothermal exposure at 1100°C to the high-CaO deposit (without K_2SO_4) presented in Table 7. The surface layer did not appear to cause additional damage compared to an identical TBC with no $CaZrO_3$.

Thermal cycling in the bottom-loading furnace is shown in Figure 61 for a DVC TBC without deposit compared to an identical TBC with a CaO deposit applied to the surface before cycling. All TBCs were intact after 200 cycles. The CaO deposit formed a $CaZrO_3$ surface layer during cycling, and did not produce additional damage to the TBC. No observable differences were detected in the YSZ top coat, underlying bond coat, or the TGO formed during cycling between the TBC without deposit and the one with the CaO deposit. Additional testing was done in which the CaO deposit was re-applied every 20 cycles. No additional damage resulted from the re-application of the CaO deposit. The surface reaction layer did not appear to influence the lifetime of the TBC.

While the $CaZrO_3$ layer on the surface of the TBC did not affect TBC lifetime in 200 cycles, internal $CaZrO_3$ formation from addition of K_2SO_4 caused considerable reduction in TBC lifetime during cycling in lab air. The TBCs shown in Figure 62 both experienced 140 cycles in the bottom-loading furnace. A high-CaO synthetic ash deposit was applied to both: one which contained only

oxides and the other with K_2SO_4 addition. The addition of K_2SO_4, and subsequent internal $CaZrO_3$ formation, caused complete spallation of the YSZ top coat. The high-CaO deposit, which formed a $CaZrO_3$ surface layer similar to the CaO deposit, did not exhibit any signs of damage to the TBC.

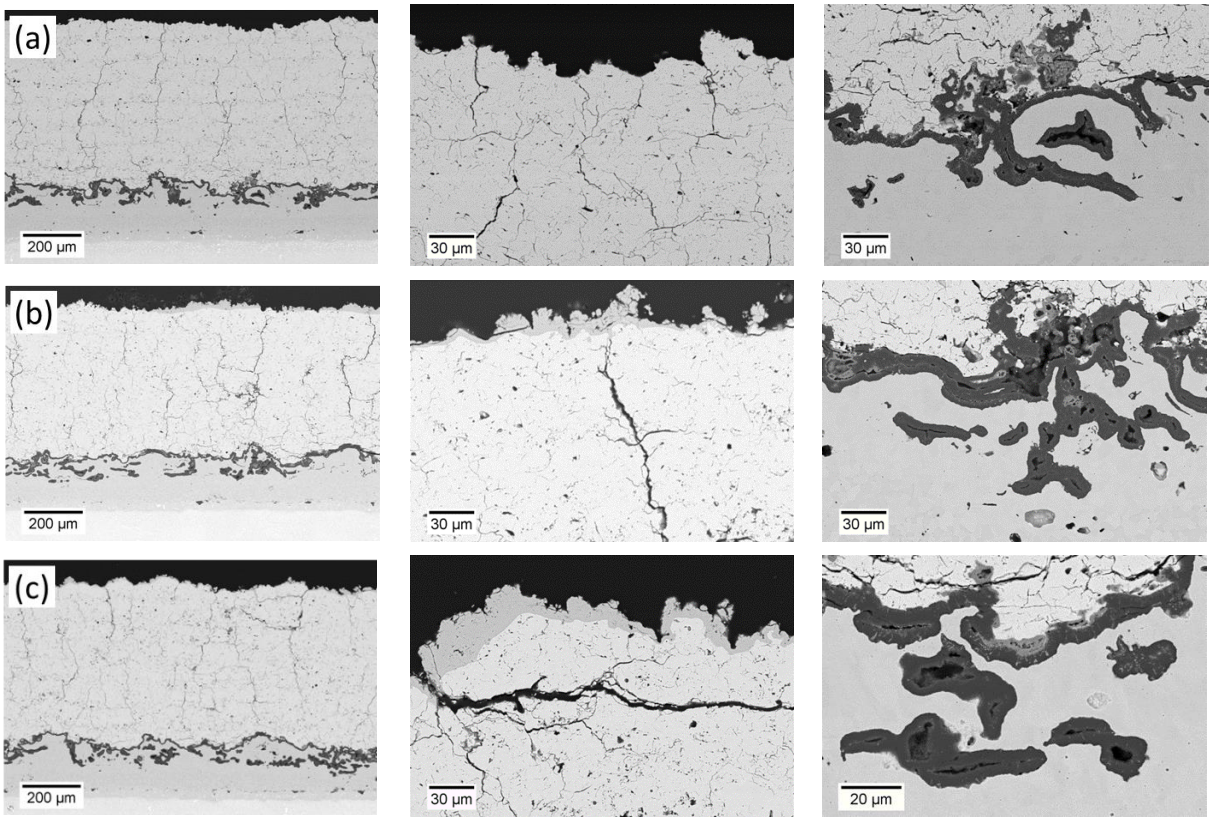

Figure 61: DVC TBC tested in cyclic bottom-loading furnace in lab air. After 200 cycles with (a) no deposit, (b) single application of CaO, and (c) re-application of CaO every 20 cycles.

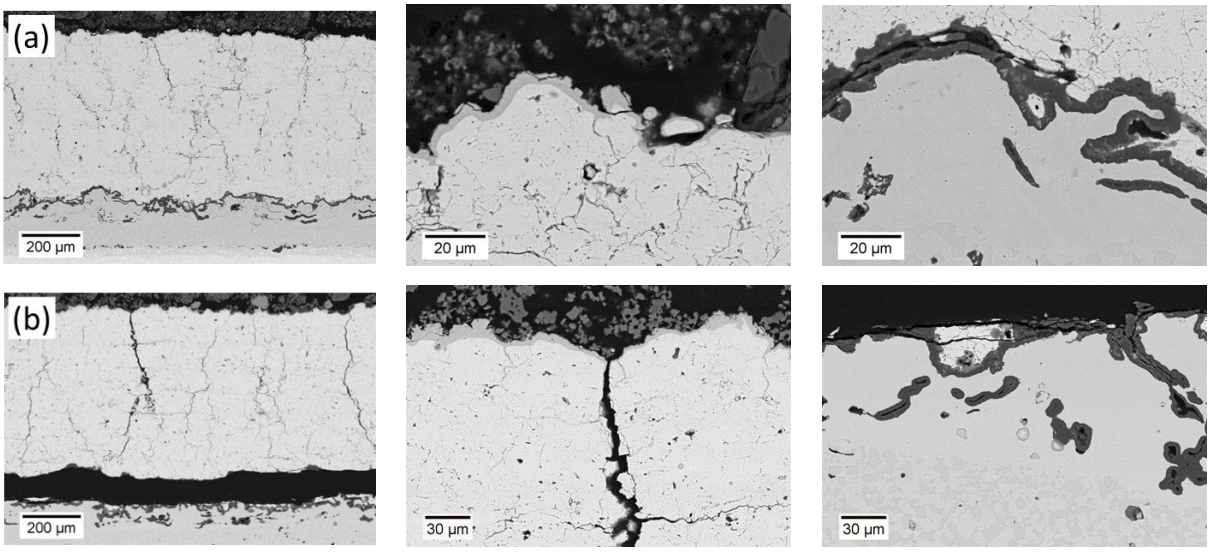

Figure 62: DVC TBCs tested in cyclic bottom loading furnace. (a) TBC intact after 140 cycles with high-CaO deposit without K_2SO_4, and (b) topcoat delamination after 140 cycles with the same high-CaO deposit including addition of K_2SO_4.

9.2 EFFECTS OF INTERNAL $CAZRO_3$ FORMATION ON MECHANICAL PROPERTIES OF YSZ

Deposit-induced degradation typically results from either chemical reaction with the YSZ topcoat or thermomechanical effects. The shortened cyclic lifetimes found with K_2SO_4-containing deposit did not appear to be the result of any chemical interaction with the YSZ top coat. There was no observable dissolution of the YSZ. The TGO remained a continuous, protective scale which did not appear to exhibit unusual levels of spinel formation. This suggests that the early failure was the result of changes in the mechanical properties of the YSZ caused by the deposit.

To explore thermomechanical effects of the deposit, the elastic modulus of free-standing YSZ samples which underwent internal $CaZrO_3$ formation was measured using a 3-point bend

test. The modulus was measured for six samples which had been heat treated for 72 hours in dry air at 1100°C. The high-CaO deposit was applied to half the samples before exposure. The results of the 3-point bend testing are summarized in Table 11. The modulus of the heat-treated samples without deposit was measured to be 30 GPa. The applied deposit, and subsequent formation of $CaZrO_3$ in YSZ cracks, resulted in an elastic modulus of 132 GPa. The measured increase in elastic modulus after internal $CaZrO_3$ formation represents the overall modulus of a "composite" YSZ-$CaZrO_3$ layer. The dramatic increase after internal $CaZrO_3$ formation is not surprising considering its modulus of E=224GPa [121] which is reported in the literature. This dramatic increase in overall coating stiffness would be expected to have detrimental effects on the residual stress in the TBC upon cooling in thermal cycling. The misfit stress caused by a thin film attached to a substrate of different CTE can be described by the equation [25]:

$$\sigma = E_{TBC}\frac{\Delta\alpha\Delta T}{1-\upsilon}. \tag{9-1}$$

Where σ is normal stress, E is elastic modulus of the YSZ, Δα is the difference in CTE between the YSZ and substrate, ΔT is the change in temperature, and υ is Poisson's ratio. This equation for stress assumes the surface layer (in this case the YSZ) is thin relative to the substrate, and also the value of υ is the same for the YSZ and metal substrate. The stress is developed as the YSZ/substrate system is cooled or heated; in the case of this study it was cooling from high temperature to a lower temperature. The CTE mismatch stress equation has been widely used to

calculate residual stress in oxides developed in high-temperature oxidation of metals. If one applies this equation to the YSZ/substrate system, then it is apparent that (for the same ΔT and α) the overall residual stress can be affected by changes in either E_{TBC} or the CTE difference between the YSZ and substrate (Δα). The internal $CaZrO_3$ formation caused by reaction of free-standing YSZ with high-CaO deposit dramatically increased E_{TBC} from 30 GPa to 132 GPa. This would cause a corresponding increase in residual stress in the YSZ, which would contribute to early TBC failure. The stored energy in the YSZ top coat would also increase with increasing elastic modulus. This will be discussed further in a subsequent section.

An additional stress would be produced by internal $CaZrO_3$ formation. The growth of $CaZrO_3$ in the YSZ was observed to progress inward into the YSZ from cracks. This resulted in the YSZ being replaced by $CaZrO_3$ (with some Y in solution). The molar volume of dense $CaZrO_3$ (40.2 cm^3/mol) is nearly twice that of dense ZrO_2 (21.7 cm3/mol). If one assumes that the molar volume of 7YSZ is close to that of ZrO_2, this dramatic increase in molar volume of the top coat material would add considerable stress in the top coat and contribute to early TBC failure in thermal cycling.

Table 11: Elastic modulus of free-standing YSZ measured from 3-point bend testing.

Sample	Elastic Modulus (GPa)
YSZ without internal $CaZrO_3$	30 ±3
YSZ with internal $CaZrO_3$	132 ±19

The thermal stress described by Equation 9-1 would also increase if the CTE difference between the YSZ and substrate increased. The CTE of YSZ (typically around 11-13x10^{-6} C^{-1}) is lower than that of the substrate (typically ~17x10^{-6} C^{-1}). If the internal $CaZrO_3$ formation resulted in a lowered CTE, then the increased $\Delta\alpha$ term would also contribute to increased thermal stress. The thermal expansion coefficient was also measured for samples which were heated for 72 hours in dry air at 1100°C. The high-CaO synthetic deposit was applied to half the samples before heat treatment in order to produce internal $CaZrO_3$ formation. Thermal expansion coefficient values obtained by dilatometry measurements done at Praxair Surface Technologies are shown in Figure 63. No significant difference in CTE was measured from the internal $CaZrO_3$ formation, which resulted from the high-CaO deposit. This result is not surprising; typical values for CTE of $CaZrO_3$ reported in literature are around 11.5x10^{-6} C^{-1} [122], which is similar to that of YSZ.

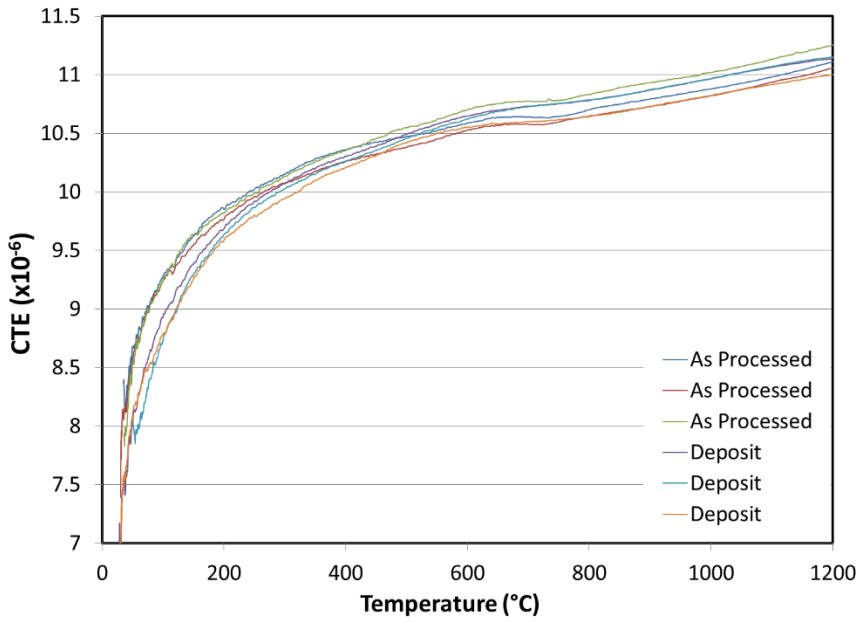

Figure 63: Dilatometry results showing no significant effect on thermal expansion coefficient caused by internal $CaZrO_3$ formation from high-CaO deposit.

9.3 EFFECTS OF INTERNAL $CAZRO_3$ FORMATION ON TBC CYCLIC LIFETIMES IN DRY AIR

Deposits containing high levels of CaO were able to cause formation of an internal reaction product in the YSZ at 1100°C, which resulted in dramatic changes in top coat stiffness. The effects of changes in mechanical properties of YSZ used as a top coat will affect TBC lifetime in thermal cycling. Similarly, liquid infiltration observed from high-SiO_2 deposits could detrimentally affect TBC lifetimes. Any liquid which fills open spaces in the YSZ at high temperatures can potentially affect the strain tolerance of the top coat upon cooling. The large open vertical cracks in DVC TBCs could be particularly sensitive to such infiltration, as they could provide more direct

pathways from the surface compared to the horizontal splat morphology of the more conventional HPLD TBCs. In order to study any such effects on lifetime, TBC failure in dry air was studied with and without these deposits in order to identify early failure mechanisms.

9.3.1 TBC Failure in Dry Air Without Deposit

Both types of TBC systems were thermally cycled in dry air according to the experimental setup described in chapter 4.3. Typical TBC failure is shown schematically in Figure 64. The delamination initiated at the sample edges during thermal cycling and then quickly extended across the entire sample. Partially delaminated samples were not available because complete delamination would always occur shortly after edge cracking was initiated. Delamination occurred along crests of the undulated interface through the TGO, leaving areas of TGO exposed. The delamination at the troughs of the undulations occurred further into the YSZ, which left some small pieces of YSZ attached to the bond coat. The micrographs of failed TBCs in dry air shown in Figure 65 and 67 for DVC and HPLD TBCs, respectively, represent typical failures. TBC failure was defined by 30% top coat spallation. However, as can be seen in the figures, both DVC and HPLD top coats exhibited complete delamination with cracks propagating along the TGO/YSZ interface. It is important to note that this location of delamination was the same for both DVC and HPLD TBCs without deposit.

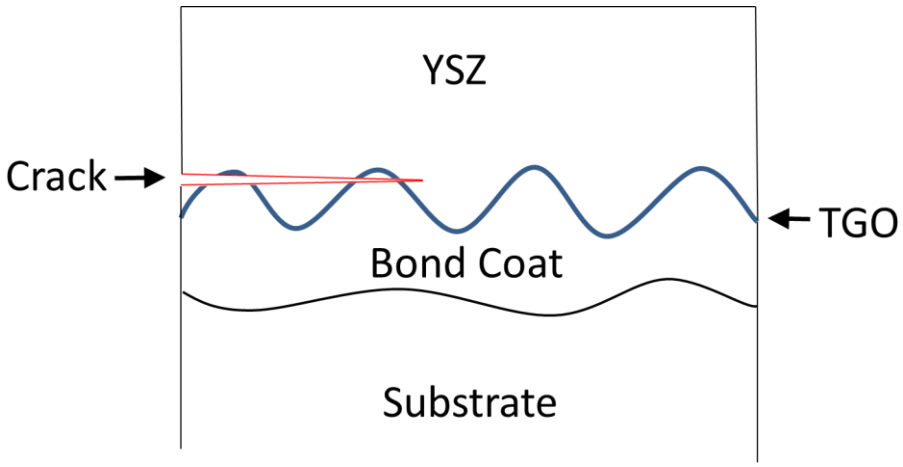

Figure 64: TBC failure caused by thermal cycling. Failure typically initiated at a TBC edge and then propagated across the tops of the undulated interface of the bond coat.

Oxidation behavior of the bond coat is represented in Figure 65(b) and 66(b). The thermally grown oxide, indicated as TGO in the micrographs, had formed a continuous layer along the bond-coat surface in both types of TBC. Some oxidation of interior pores was also observed in the bond coat. The TGO was determined by EDS analysis to consist predominantly of alumina. Some lighter regions inside the alumina represented mixed oxides of chromium and nickel. Overall, the bond coat oxidation was consistent with normal TBC performance [99]. There was no evidence that the bond-coat oxidation contributed significantly to the TBC failure, which would have been indicated by significant internal oxidation [59], formation of non-protective oxides [63, 123], dissolution of the TGO [32, 123], etc.

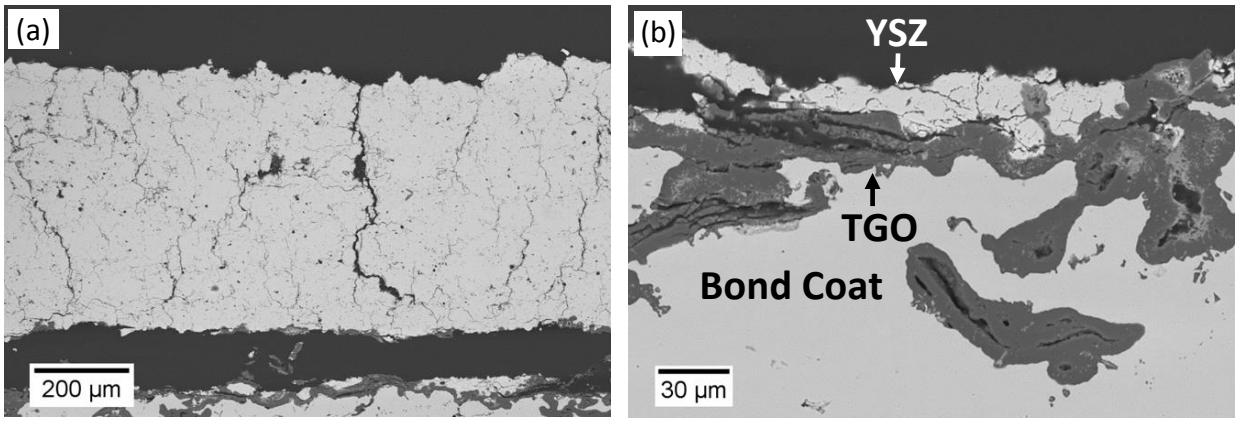

Figure 65: DVC TBC failure after 1214 cycles in dry air without deposit. (a) The top coat delaminated entirely from the substrate as a single intact coating, (b) failure occurred along the TGO/YSZ interface.

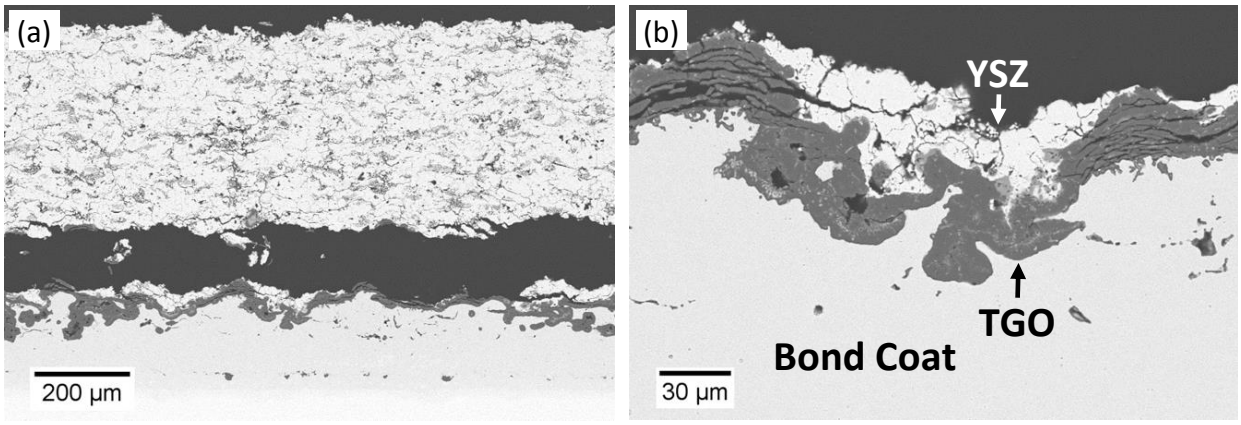

Figure 66: Conventional HPLD TBC failure after 1000 cycles without deposit was nearly identical to the DVC TBC failure. (a) The top coat delaminated completely from the substrate as a single intact coating, (b) delamination occurred at the TGO/YSZ interface.

9.3.2 Early DVC TBC Failure with Deposits

Cyclic failure of DVC TBCs was assessed after exposure in dry air and with several different deposits. A single application of a given deposit was applied to a TBC surface before thermal cycling. Deposit application was done using a dropper at a loading of 35 mg/cm^2 after mixing with ethanol to create a slurry. Figure 67 summarizes the effect on DVC TBC performance from three deposits: K_2SO_4, and the two synthetic ash deposits presented in Table 12. Three TBCs were tested to failure with each deposit. The high-SiO_2 and high-CaO deposits consisted of oxides and minor constituents (K_2SO_4, FeS) typically found in fly ash. Reduced TBC lifetimes were observed in the presence of all three deposits compared to cyclic performance without a deposit. The measured cyclic lifetime of 1200 cycles of the TBC without deposit was used to define a normal lifetime under the current cyclic exposures. Further, the nature of the failed TBC shown in Figure 65 was taken to represent a typical failure morphology. Failed TBCs with different deposits were then compared to this baseline to identify additional damage which contributed to the early failure.

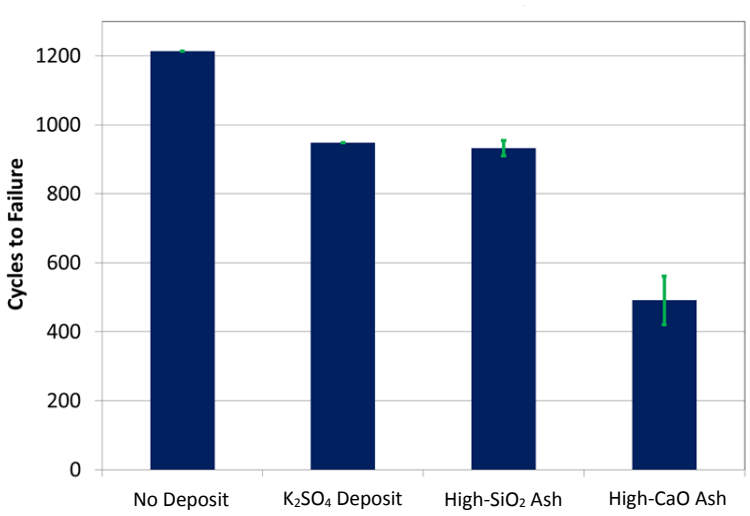

Figure 67: Cyclic failure of DVC TBCs in dry air with different deposits compared to failure without a deposit.

Table 12: Synthetic ash compositions (mol %) used in cyclic testing of TBCs.

	CaO	**SiO_2**	**Al_2O_3**	**MgO**	**Fe_2O_3**	**K_2SO_4**	**FeS**
High-SiO_2 Deposit	11	54	16	8	4	2	4
High-CaO Deposit	70	17	5	1	1	2	4

A representative failed DVC TBC with high-CaO deposit is shown in Figure 68. The location of failure was very similar to a typical TBC failure without deposit. Complete top coat delamination occurred at the TGO along the undulations of the bond coat surface. The spallation sheared through the TGO at the peaks of the undulations, which left some YSZ attached to the bond coat in the troughs. The TGO did not appear to be significantly altered by the presence of the deposit. A continuous Al_2O_3 layer was intact at the bond coat surface and there was no indication of TGO dissolution or a large amount of non-protective oxide formation.

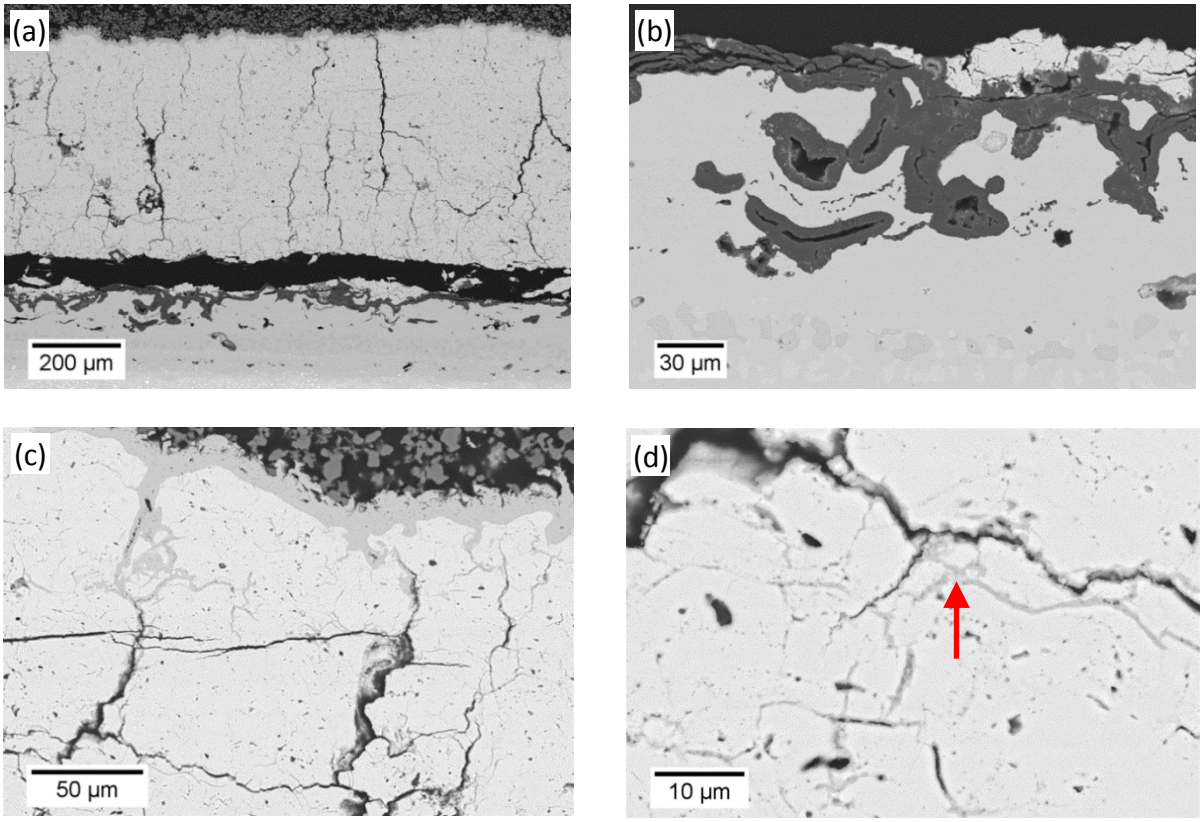

Figure 68: Failed DVC TBC after 630 cycles in dry air with high-CaO synthetic ash deposit. (a) Top coat delamination is similar to failure without deposit, (b) Alumina growth in the bond coat was not affected, (c) $CaZrO_3$ was observed as a surface layer, and (d) penetrated into the top coat as shown by arrow.

The high-CaO deposit did not significantly affect oxidation of the bond coat. There was, however, a reaction involving the YSZ top coat near the TBC surface. Figure 68c and 69d show a dense reaction product which had formed a continuous layer along the surface and also extended into the YSZ by filling many cracks and open pores in the top coat. This product, which was identified by EDS and XRD to be $CaZrO_3$, was observed to penetrate a significant distance (250-

300μm) from the YSZ surface. The nature of the internal $CaZrO_3$ formation, which occurred most significantly at the high temperature of the thermal cycling, was discussed in detail in chapter 5. The results shown here agree with the previously-discussed isothermal tests, which showed internal $CaZrO_3$ formation from a CaO-rich deposit at 1100°C.

The reduction in TBC lifetime after a single application of high-SiO_2 deposit was less severe than that of high-CaO deposit. The failure in the presence of high-SiO_2 deposit after 910 cycles is shown in Figure 69. The failure with the two deposits was very similar. No significant difference was observed at the TGO/bond coat interface: delamination occurred along the TGO along the crests of the undulated YSZ/bond coat interface. Furthermore, the high-SiO_2 deposit did not appear to contribute to any non-protective oxide formation or TGO dissolution. As in the case of the high-CaO deposit, there was no evidence to suggest that the early delamination of the top coat was related to the bond coat oxidation.

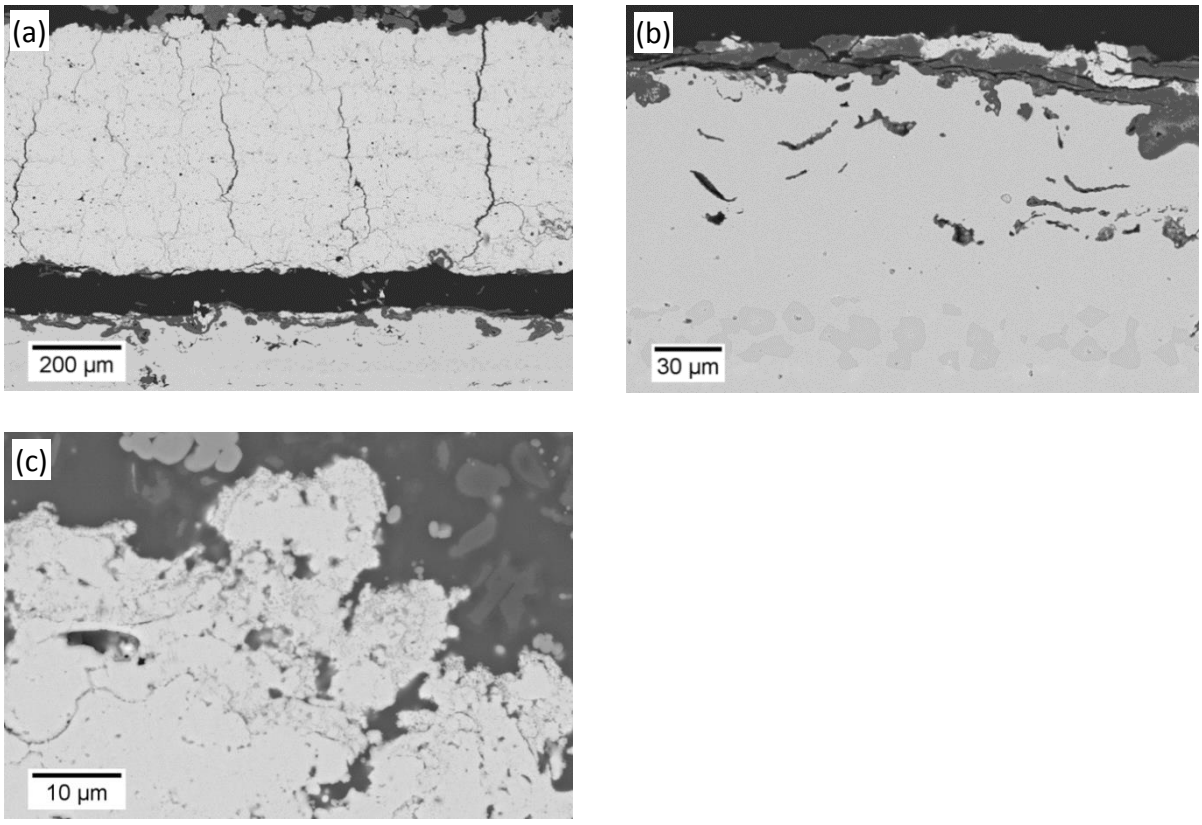

Figure 69: DVC TBC failure after 910 cycles in dry air with high-SiO_2 synthetic ash. (a) Complete top coat delamination, (b) typical bond coat oxidation expected after thermal cycling, and (c) change in microstructure at surface indicating some reaction between the ash and YSZ.

A magnified image of the top coat near the deposit indicated some change in morphology between the YSZ and the high-SiO_2 deposit. This reaction did not contain any measurable levels of $CaZrO_3$, which was found after exposure with high-CaO deposit. As discussed in chapter 6, the liquid infiltration from high-SiO_2 deposit was determined from EDS to contain potassium, silicon, and oxygen. This infiltration appeared to wet many of the YSZ cracks near the surface, which would indicate some liquid formation at 1100˚C during thermal cycling. The change in YSZ morphology shown in Figure 69 at the deposit/YSZ interface could have been the result of some

destabilization of the 7YSZ, similar to what has been reported in other studies with SiO_2-rich deposits [32]. Typically this occurs after dissolution-reprecipitation of YSZ [32]; although, here it appeared to have occurred only in very small areas at the surface of the YSZ. Overall, the silicate infiltration did not damage the TBC as severely as internal $CaZrO_3$ formation, as indicated by the longer lifetimes.

Cyclic testing with a K_2SO_4 deposit reduced TBC lifetimes to values similar to those measured with the high-SiO_2 synthetic ash deposit. The mode of failure with K_2SO_4 was also similar to that of exposure to the high-SiO_2 and high-CaO deposits. At failure, the YSZ delaminated along the TGO as a single intact coating. In contrast to other deposits, however, no penetration of YSZ cracks from liquid or reaction product formation near the surface of the top coat was observed with the K_2SO_4 deposit after failure. Figure 70 shows no indication of K_2SO_4 on the surface of the YSZ or inside cracks below the surface. This absence of K_2SO_4 after exposure was consistent with the high volatilization rate of K_2SO_4 at 1100˚C, which was verified experimentally. This was discussed in detail in section 6.5.

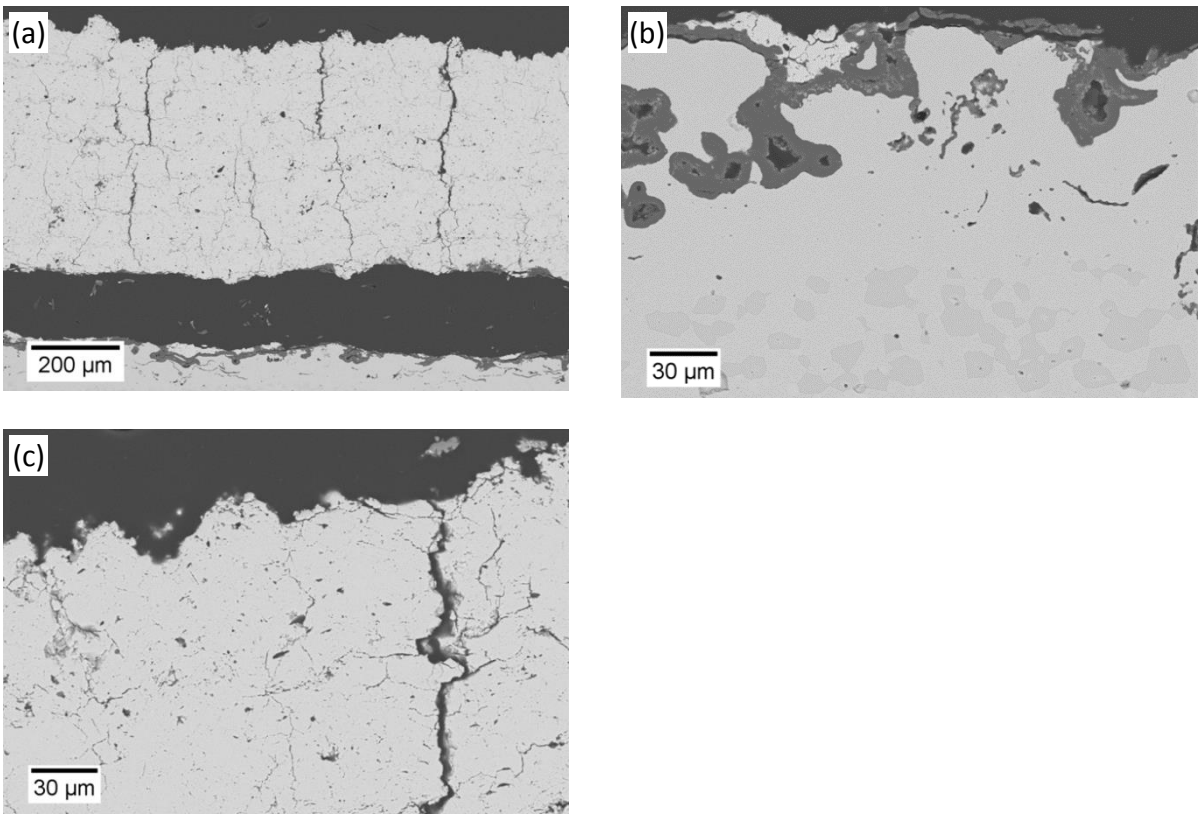

Figure 70: Failure of DVC TBC in dry air after 948 cycles with K_2SO_4 deposit. (a) Complete top coat delamination, (b) normal bond coat oxidation, and (c) no reaction with YSZ.

The effect on bond coat oxidation was different in the case of the K_2SO_4 deposit. Delamination of the TBC with a pure K_2SO_4 deposit, as shown in Figure 71, was a consequence of severe damage of the bond coat near the edge of the sample. Extensive internal oxidation was observed in the bond coat near the edge of the TBC coupon. The inter-linked intrusions were confirmed by EDS to be comprised predominantly of alumina, which would normally form as a continuous layer on the surface of the bond coat (as observed in previous cyclic testing). The areas of bond coat near to these regions were also completely depleted of beta phase, indicative

of extensive Al consumption, which is consistent with the observed internal oxidation. These observations are consistent with studies in sulfur-containing atmospheres, which report the promotion of internal oxidation in alloys which would normally form protective scales [48]. The areas of the TBC farther from the edge were protected by the YSZ top coat, and the detrimental effects on the TGO were only observed on the sample edges where the TGO was exposed to liquid K_2SO_4. This type of degradation mechanism is similar to what is expected in Type I hot corrosion involving Na_2SO_4 [124, 125]. As the bond coat is oxidized to form the TGO, oxygen potential in liquid sulfate decreases which causes sulfur potential to increase. In Type I hot corrosion, this causes sulfur penetration through the oxide layer and disruption in oxidation as internal sulfides are formed [124].

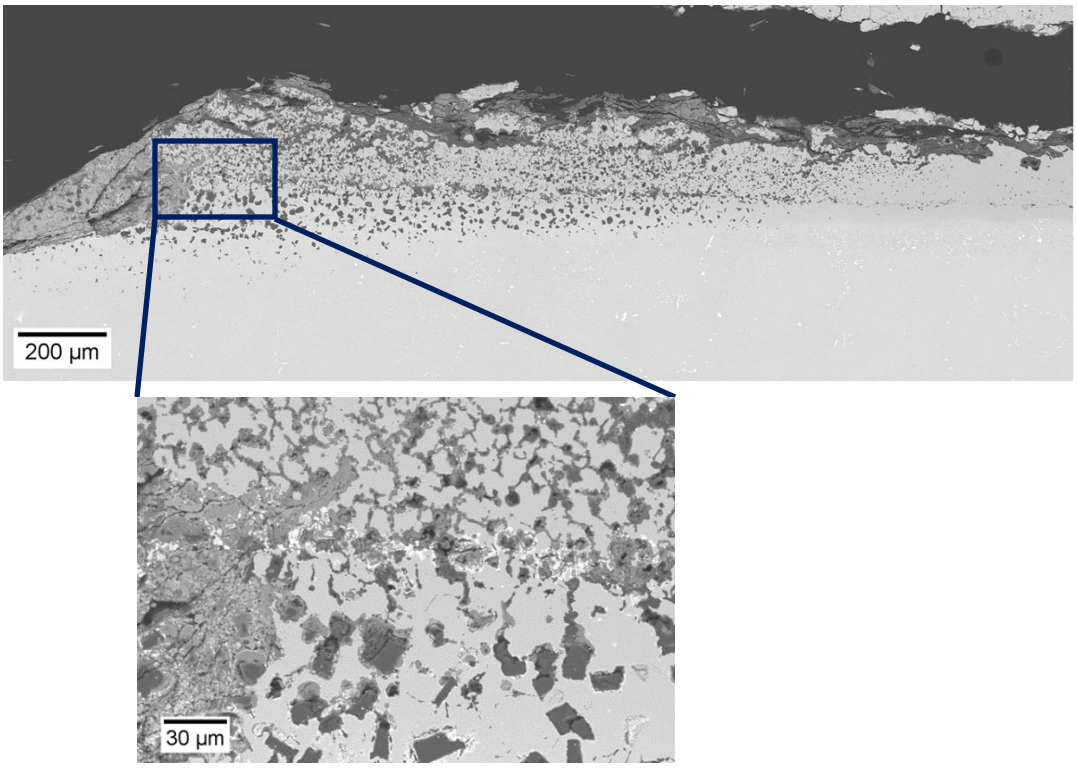

Figure 71: DVC TBC failure after 948 cycles in dry air with K_2SO_4 deposit. Internal oxidation of the bond coat is observed near the edge of the TBC after failure.

9.3.3 Effect of Top Coat Microstructure on Deposit Failure

Both HPLD and DVC TBCs were tested to failure in dry air with the high-CaO and high-SiO_2 deposits listed in Table 13. Lifetimes shown in Figure 72 are used as a relative comparison between top coat durability with the same deposits. The shorter lifetime for the DVC TBCs with the high-SiO_2 deposit compared to Figure 67 is attributed to the increased K_2SO_4 level in the deposit. The effect of varying K_2SO_4 levels will be examined in more detail in chapter 10. It is important to note that lifetimes of both top coats were comparable without deposits.

Table 13: Synthetic ash compositions (mol %) used for top coat comparison shown in Figure 72.

	CaO	SiO_2	Al_2O_3	MgO	Fe_2O_3	K_2SO_4	FeS
High-SiO_2 Deposit	12	55.5	16.5	8	4	4	
High-CaO Deposit	70	17	5	1	1	2	4

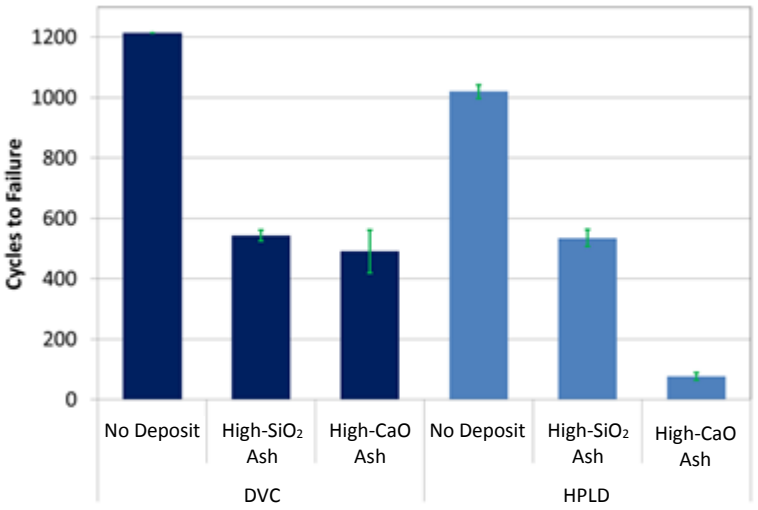

Figure 72: Failure of DVC and HPLD TBCs after 1-h cycles at 1100°C in dry air. Synthetic ash compositions are described in Table 13.

The cyclic lifetimes of TBCs with the high-SiO_2 deposit were similar for both DVC and HPLD TBCs. The high-CaO deposit, however, led to a much more dramatic decrease in HPLD TBC lifetime. The distinguishing feature of HPLD TBC failure shown in Figure 73 was that cracking and delamination occurred inside the top coat away from the TGO, as opposed to DVC top coats which remained intact until delamination. Regions in the TBC close to the surface shown in Figure

73 indicate $CaZrO_3$ formation similar to what was observed with DVC top coats. TBC cracking is observed below the infiltrated region.

Failure of HPLD TBCs from cracking deep in the top coat is similar to failure which was observed in a previous study [50]. In that study, the increased strain energy associated with a thicker top coat contributed to failure. The early failure observed in this work would result from a similarly increased strain energy caused the internal $CaZrO_3$ formation.

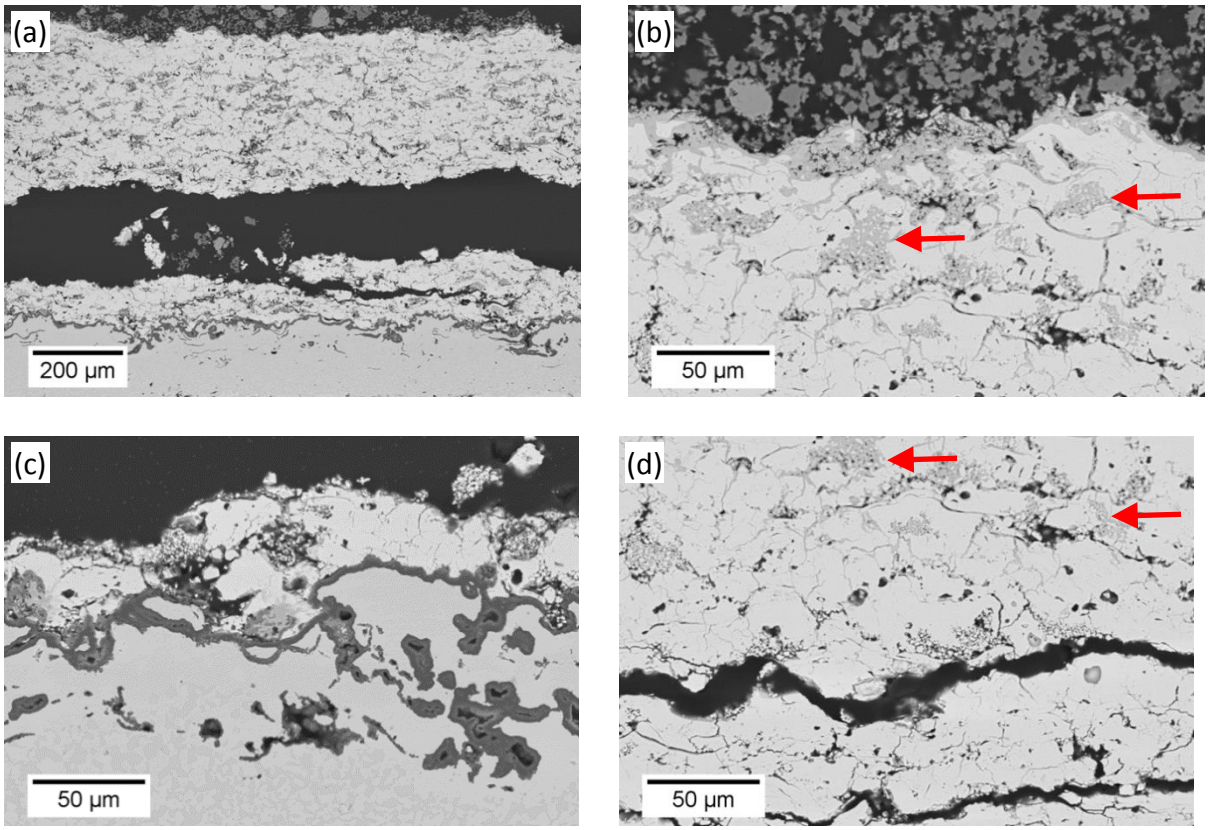

Figure 73: HPLD TBC failure in dry after 65 cycles with high-CaO deposit described in Table 13. (a) Complete top coat delamination is shown deep in the YSZ, away from the bond coat. (b) Internal $CaZrO_3$ formation in open pores of the YSZ is indicated by arrows near the YSZ surface where the deposit was applied. (c) Bond coat oxidation did not exhibit any abnormalities compared to cyclic exposures without deposit. (d) Internal $CaZrO_3$ formation is indicated by arrows in region above cracking in the YSZ.

No noticeable abnormalities were observed in bond coat oxidation that could be linked to the TBC failure. The β phase in the bond coat was not depleted from the bond coat more than what would be expected from cycling without a deposit. Furthermore, the alumina scale layer at the YSZ/bond coat interface was intact at failure. These observations indicate that early TBC failure was not related to problems with bond coat oxidation.

Failure of HPLD TBCs in the presence of a high-SiO_2 deposit shown in Figure 74 was not significantly different from the failure incurred with a high-CaO deposit. Some cracking was observed in the YSZ, however complete delamination of the top coat occurred in the YSZ near the TGO. The significant cracking shown in Figure 74 propagated along the crests of the undulated bond coat surface. The surface of the YSZ near the deposit experienced some infiltration of a liquid silicate during high temperature exposures, and some cracking was also observed near the infiltrated regions.

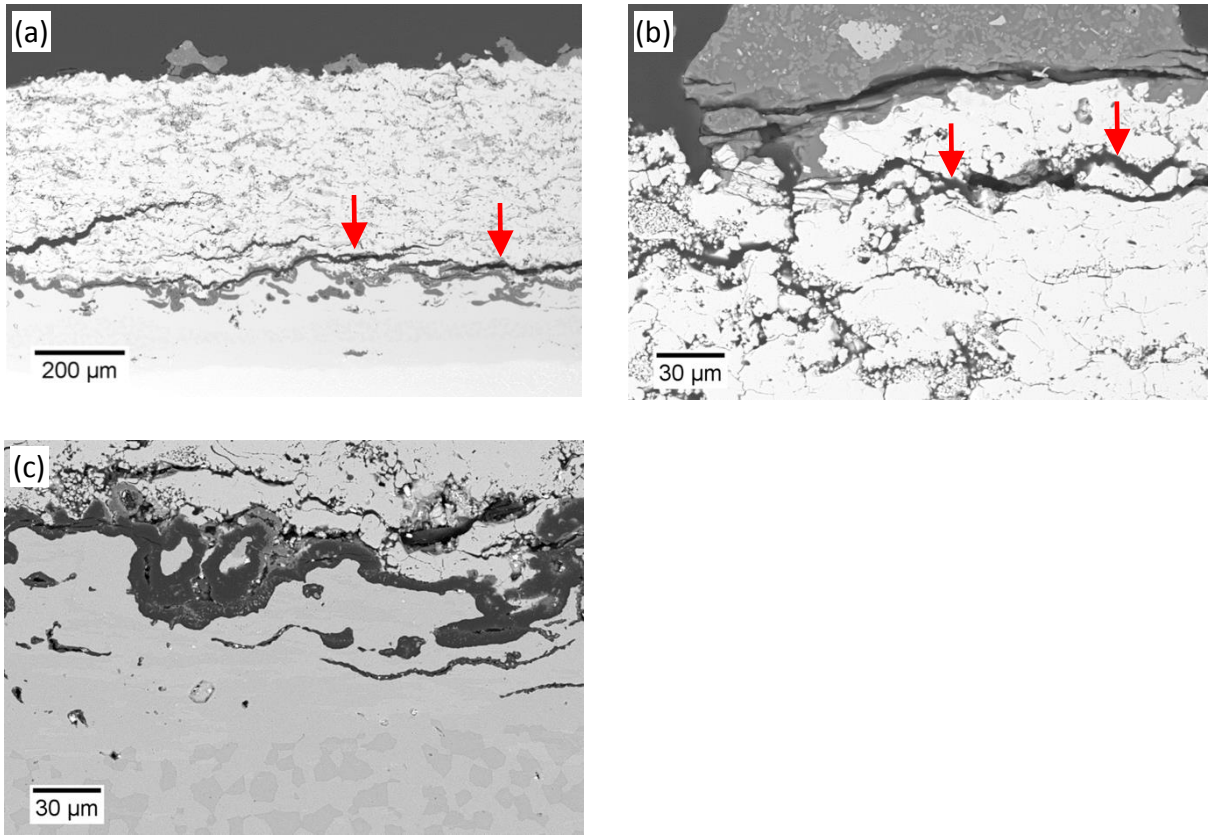

Figure 74: HPLD TBC failure in dry air after 575 cycles in dry air with high-SiO_2 deposit described in Table 13. (a) Significant cracking in the YSZ is indicated along the undulated interface with the bond coat. (b) Some infiltration in the YSZ at the surface where the deposit was applied. (c) Normal bond coat oxidation which would be expected from cycling without deposit.

9.4 DISCUSSION OF TBC FAILURE IN DRY AIR

The cyclic lifetimes of DVC TBCs reported in Figure 67 show the detrimental effects of surface deposits which include K_2SO_4. As shown in chapters 6 and 7, K_2SO_4 addition to deposits high in CaO and/or SiO_2 cause liquid infiltration in the YSZ top coat. The cyclic lifetimes presented

here indicate that this infiltration degrades the TBC top coat and leads to shortened cyclic lifetimes. Severe degradation has also been shown for HPLD TBCs.

A severely shortened DVC TBC lifetime was observed with the high-CaO deposit capable of producing the internal $CaZrO_3$ formation in the YSZ top coat. It was shown in section 0 that internal $CaZrO_3$ formation was capable of dramatically increasing the elastic modulus of the YSZ top coat. This increased stiffness led to greater stresses in thermal cycling which caused early failure. The stored energy per unit area, U, in the top coat can be modeled by the equation [44]

$$U \approx \frac{\sigma^2 h_{tbc}}{2E_{tbc}} \tag{9-2}$$

Where h_{tbc} and E_{tbc} are the thickness and elastic modulus of the top coat, respectively. The stress (σ) can be calculated using equation 9-1. TBC delamination should occur when the stored energy (U) exceeds the delamination toughness of the TBC (Γ≈50-100 J/m^2) [25, 44]. Stress and stored energy can be calculated with typical values for υ=0.2 and $\Delta\alpha=3\times10^{-6}$ and using measured values of E_{tbc}= 30 GPa and h_{tbc}=400µm for the YSZ used in this study. The calculated values (for ΔT=900°C) are σ=100 MPa and U= 80 J/m^2. This calculated stored energy is similar to the toughness of the TBC. Stress and stored energy for the same TBC which is degraded by internal $CaZrO_3$ formation (according to results discussed in section 9.2) would be

around σ=590 MPa and U= 534 J/m^2. The dramatically increased value for stored energy contributed to early TBC delamination in the presence of high-CaO deposits.

The detrimental effect of the high-SiO_2 deposit was less severe compared to the high-CaO deposit. Although it was shown in section 7.1 that the high-SiO_2 deposit was capable of producing a silicate infiltration, the resulting damage to the TBC was not as severe compared to the $CaZrO_3$ formation with the same level of K_2SO_4 in the deposit (as indicated by the lifetimes reported in Figure 67). The change in elastic modulus would not be the same for silicate infiltration and internal $CaZrO_3$ formation. The elastic modulus of silicate would be around that of a typical glass, ~90 GPa [45], whereas the elastic modulus of $CaZrO_3$ is ~224 GPa [121]. The DVC cyclic lifetimes presented in Figure 72 are similar to those for high-CaO and high-SiO_2 deposits because the level of K_2SO_4 addition was higher for those high-SiO_2 deposit compared to the high-CaO deposit. Higher levels of K_2SO_4 in the high-SiO_2 deposit resulted in more liquid silicate infiltration, and correspondingly shorter TBC lifetimes.

The increased strain tolerance provided by the vertical cracks in the DVC top coats make them less sensitive to differences in elastic modulus between silicate infiltration and $CaZrO_3$ formation, and similar lifetimes were reported in Figure 72 for high-CaO and high-SiO_2 deposits. HPLD TBCs, however, experienced degradation and early failure which was more severe with $CaZrO_3$ formation. The HPLD coating would be more sensitive to the increased stored energy because of the splat morphology. The horizontal splat edges would provide a lower-toughness boundary along which cracks would propagate more readily. This is apparent in the fact that extensive cracking occurred in HPLD TBC the top coat layer, relatively far away from the

TGO/bond coat boundary. This type of cracking has been reported for HPLD top coat failure as a result of liquid infiltration [95] in turbine blades pulled from service in desert environments. Although the splat morphology inhibits liquid infiltration compared to EB-PVD coatings, the lower toughness along these horizontal splat boundaries increases the damage from any liquid that does infiltrate the YSZ. The difference in this study, however, is the temperature at which the effect is observed. Other studies report that this type of damage from infiltration (typically caused by CMAS deposits) will not occur at temperatures lower than ~1200°C [32, 45].

10.0 ATMOSPHERIC EFFECTS ON HPLD TBC CYCLIC LIFETIME

The detrimental effects of deposits in dry air were shown in section 0. Actual turbine environments, however, contain significant levels of steam as well as some SO_2. Steam content in IGCC systems has been reported to be up to 14% at the turbine inlet, and 12-14% at the exhaust [7]. Sulfur content in IGCC systems can vary depending on the type of coal feed, but generally has been reported to be around 22ppm [7]. This is significantly lower than flue gases from conventional coal-fired power plants, however the effects of SO_2/SO_3 could contribute to TBC degradation after extended periods of turbine operation. Therefore, the effects of steam and SO_2 on deposit-induced TBC degradation were studied.

10.1 FAILURE OF HPLD TBCS IN DIFFERENT GAS ATMOSPHERES

Cyclic testing was done in three different gas atmospheres: dry air, air+20% steam, and 2%O_2-1000ppm SO_2-bal CO_2. These gas atmospheres were chosen to study possible effects from environments relevant to IGCC systems. The high-SiO_2 deposit was chosen because it more closely represents a typical IGCC fly ash composition. Figure 75 shows that cyclic lifetimes without

deposit were nearly identical in atmospheres of dry air and 2%O_2-1000ppmSO_2-bal CO_2. Early failure with high-SiO_2 deposit was slightly exacerbated in the SO_2-containing atmosphere (as indicated by slightly shorter lifetimes compared to deposit failure in the other atmospheres). This suggests that some combined effect of deposit and atmosphere may exist in the SO_2-containing environment. Failure time in the steam-containing atmosphere, however, was nearly identical to that of dry air with the high-SiO_2 deposit.

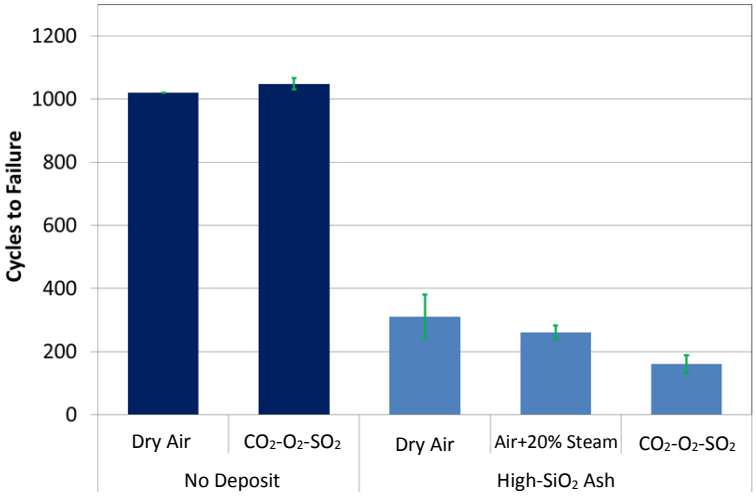

Figure 75: HPLD TBC failure in several gas atmospheres.

Failed TBCs in both the air+steam and CO_2-O_2-SO_2 atmospheres with the high-SiO_2 deposit are shown in Figure 77. In both atmospheres, the YSZ top coats experienced large-scale delamination along the TGO. This location of large-scale delamination was similar to what was observed dry air cyclic exposures. Overall failure in the air+steam atmosphere was

indistinguishable from the dry-air failure. The steam also did not noticeably affect infiltration from the silicate formation in the deposit.

The Raman scan shown in Figure 76 was obtained at an internal point 100 µm below the surface of a failed HPLD YSZ top coat after failure in the CO_2-O_2-SO_2 atmosphere. The existence of the characteristic peaks which correspond to the t' phase (and the absence of the peaks corresponding to the cubic and monoclinic phases) indicates that no detectable amounts of YSZ destabilization had occurred as a result of the SO_2-containing atmosphere. This result is consistent with the observation that TBC lifetimes in the two atmospheres were nearly identical. Early failure was thus attributed to damage from the deposit.

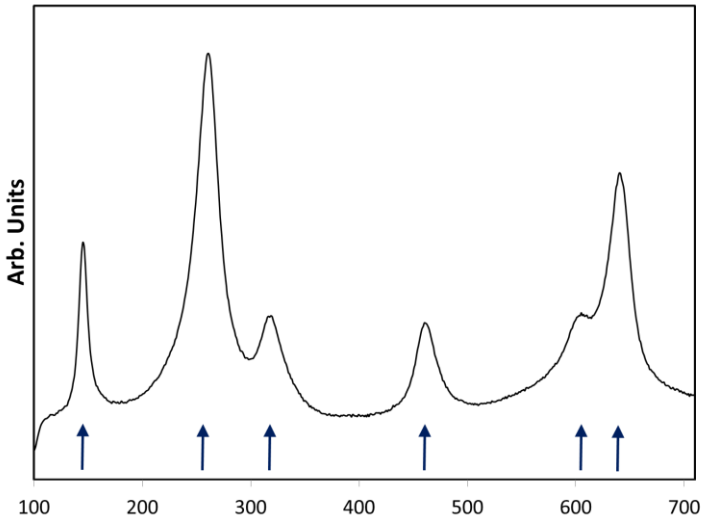

Figure 76: Raman scan of YSZ topcoat from failed HPLD TBC after 1000 cycles in 2%O_2-1000ppm SO_2-bal CO_2 atmosphere. The peaks indicated by the arrows correspond to those expected for the t' phase, indicating that the no destabilization occurred during cycling.

TBC failure from cyclic exposures with high-SiO_2 deposit in the CO_2-O_2-SO_2 atmosphere was accompanied by additional damage to the bond coat, as shown in Figure 78. Undulated regions of the bond coat surface occasionally exhibited internal oxidation indicated by alumina intrusions. Large numbers of the alumina intrusions occasionally linked together to cut off parts of the bond coat near the YSZ. These intrusions appeared with the combined presence of deposit and SO_2-containing atmosphere and (at the time of YSZ delamination) only occurred at the crests of the undulated surface.

Additional thermal cycling was done with a TBC which had failed with a high-SiO_2 deposit and exposed to an SO_2-containing atmosphere. After top-coat spallation, the high-SiO_2 deposit was applied directly to the exposed bond coat, which was then exposed to additional thermal cycling in the SO_2-containing atmosphere. The failed TBC is shown in Figure 78c after 20 cycles with direct bond coat exposure to the deposit. The extent of internal oxidation increased after the additional thermal cycles, and extended over larger regions of the bond coat. Alumina intrusions reached into the troughs of the undulated surface (rather than only the crests). Additionally, X-ray maps shown in Figure 78d and 79e indicate that the internal alumina was concurrent with the presence of sulfur near the bond coat surface.

TBC lifetimes in the CO_2-O_2-SO_2 atmosphere were comparable to those of dry air, and were only shortened when a deposit was applied prior to thermal cycling. Significant edge effects, however, were observed in the CO_2-O_2-SO_2 atmosphere without the deposit. Figure 79 shows damage to the bond coat near the edge of a TBC without deposit after 1048 cycles in the CO_2-O_2-SO_2 atmosphere. Although the damage near the edge was dramatic, it did not extend to the

center of the TBC. The fact that failure occurred at 1048 cycles also shows that the observed edge damage did not lead to early failure.

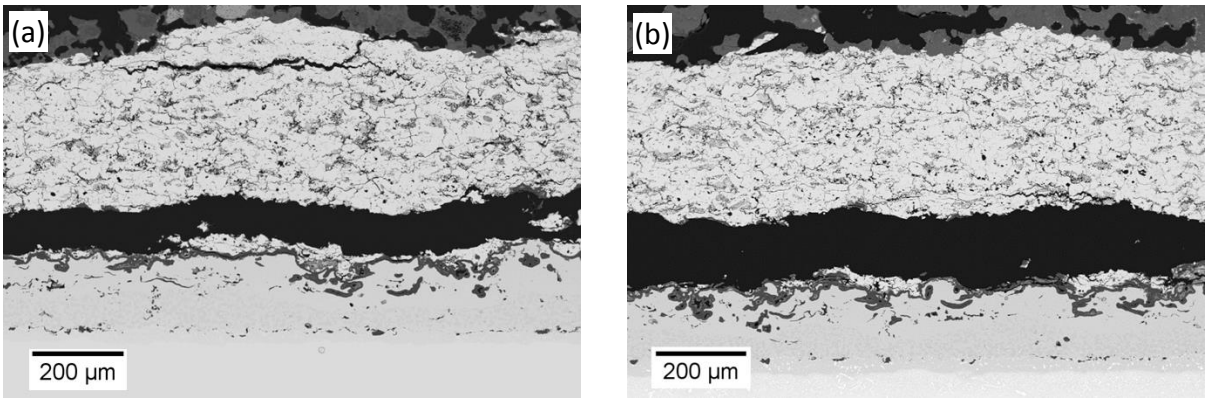

Figure 77: HPLD TBC failure from high-SiO_2 deposit (a) after 320 cycles in air+20%steam and (b) after 220 cycles in 2%O_2-1000ppm SO_2 atmosphere.

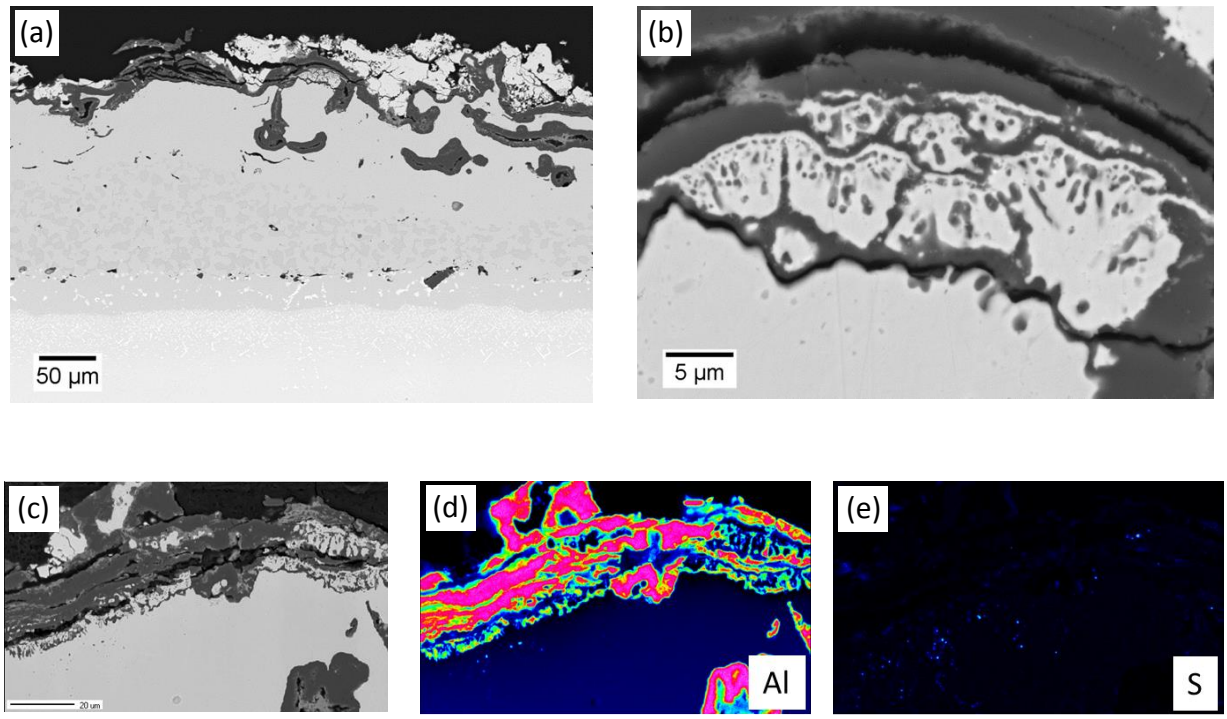

Figure 78: (a) Failure of HPLD TBC after 220 cycles with high-SiO_2 deposit in 2%O_2-1000ppm SO_2 atmosphere and (b) magnified image of alumina intrusion in bond coat. (c) Failed TBC experienced 20 additional cycles with deposit applied directly to exposed bond coat which caused an increase in the internal alumina formation. (d) EDS shows intrusions of alumina and (e) isolated areas of sulfur potentially indicating sulfides near the surface.

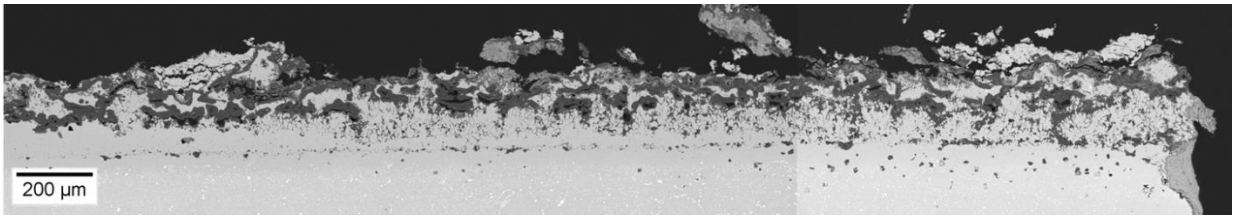

Figure 79: Severe degradation of bond coat near the edge of the TBC after 1048 cycles in 2%O_2-1000ppmSO_2–bal CO_2 atmosphere without deposit.

10.2 DISCUSSION OF EFFECT OF GAS ATMOSPHERE

TBC cyclic lifetimes without deposit were nearly identical in dry air and the O_2-SO_2-CO_2 atmosphere. Overall, cyclic lifetimes with the high-SiO_2 deposit were similar in all three gas atmospheres. The presence of steam or SO_2 did not appear to significantly alter the rate at which the liquid silicate infiltration from the high-SiO_2 deposit damaged the top coat and caused early failure.

The steam-containing atmosphere did not cause any apparent damage to the TBC similar to those discussed in section 0. No destabilization of the YSZ was identified after failure from low temperature degradation which has been known to occur in the presence of moisture [28, 62, 126]. Also, the comparable cyclic lifetime to the dry-air exposure indicates that alumina adhesion to the bond coat was not a factor, as has been reported in other studies [54, 58]. TBC spallation was identical to that which was observed in the dry air cyclic exposures. The absence of these moisture-related failure mechanisms in these experiments suggests that the thermal cycling was not sufficiently harsh to exacerbate TBC damage. Moisture-induced spallation has been observed in laboratory experiments at room temperature. The cold zone used in the cycling experiments in this work was 160°C. The current experimental setup did not accommodate monitoring actual TBC temperature in this cold zone, and it is unlikely that the TBCs actually achieved a temperature as low as 160°C. Shorter cyclic lifetimes could result from harsher thermal cycling. This is an area in which more study is required for further understanding.

Internal oxidation in the presence of a deposit and in an SO_2-containing atmosphere at this temperature is not reported in the literature. Hot corrosion studies typically report degradation from Na_2SO_4 and/or V_2O_5 at temperatures ≤1000°C. Degradation of an alumina TGO from thermal cycling in the presence of salts has been reported [123] in dry air at 1000°C in the presence of a Na_2SO_4+V_2O_5 deposit. The cause of the internal oxidation in that study was dissolution of the TGO resulting from a reaction with the salts. No evidence of TGO dissolution was observed in the present experiments. The observed sulfur near the TGO found with EDS mapping, as shown in Figure 78, indicates sulfide formation in the bond coat. This could result from K_2SO_4 contact with the TGO. This type of internal sulfide formation is similar to what is observed in Type I hot corrosion in dry air. The occurrence of such internal sulfidation in the middle of the TBC requires some K_2SO_4 to penetrate to the bond coat. The resulting internal attack should create additional stresses upon cooling in thermal cycling, which was manifested by a slightly reduced cyclic lifetime in TBCs where it was observed.

The combination of the high-SiO_2 deposit and the SO_2 environment caused some internal alumina formation farther from the edge, near the middle of the TBC. This likely contributed to the stresses associated with increased alumina formation and led to some additional reduction in TBC lifetime compared to the dry air cyclic exposures (as shown in Figure 75). It is important to note, however, that a significant lifetime reduction was the result of the deposit in all gas atmospheres tested, and the additional detrimental effect of deposit+SO_2 only added slightly to the overall reduction in lifetime. The majority of the damage was caused by the deposit (and resulting liquid infiltration). The effects of sulfur are known to create detrimental effects such as loss of oxide adhesion and sulfidation of the bond coat. The effects of the SO_2 atmosphere

combined with silicate infiltration were not studied any further in this work because they did not appear to contribute significantly to early failure, and they are left for a future study.

Deposit penetration down to the bond coat was not observed with SEM-EDS analysis, although some deposit constituents could have existed at levels too low to be detectable by the SEM. Deposit infiltration was observed in isothermal testing to penetrate several hundred microns from the surface. Some pockets of solidified K_2SO_4 (which did not react to form silicate) were also observed at those depths. This penetration depth would be enough to reach the TGO in the TBC systems.

Significant internal oxidation of the bond coat was observed near the edge of the TBC in the SO_2-containing atmosphere in the absence of a surface deposit. This edge damage in the SO_2 atmosphere, however, did not significantly decrease overall TBC cyclic lifetime. This result is important, because similar edge damage was also observed in dry air testing with K_2SO_4 deposit, as shown in Figure 71. In that test, however, TBC lifetime was reduced. The edge damage did not appear to be responsible for the early failure.

Testing was not done with high-CaO deposits in the SO_2-containing atmosphere. As shown in Figure 49, $CaSO_4$ would be stable in the O_2-SO_2-CO_2 atmosphere used in this study. The internal $CaZrO_3$ formation would also be expected with the presence of K_2SO_4-$CaSO_4$, as was shown in Figure 40. Correspondingly shortened TBC lifetimes should therefore result from $CaSO_4$ formation in a high-CaO deposit in the SO_2-containing atmosphere. The effects of the $CaZrO_3$ formation in the SO_2-containing atmosphere (and subsequent detrimental effects on TBC lifetimes) is a topic for future study.

11.0 EFFECT OF EXPERIMENTAL VARIABLES ON TBC LIFETIMES

The results presented in chapters 9 and 10 show that deposit accumulation on the surface of TBCs can affect their cyclic lifetimes in laboratory experiments. The purpose of the following work was to show that these detrimental effects were not limited to specific conditions. Experimental variables were changed to show what effect, if any, that they had on failure times.

11.1 EFFECT OF VARYING K_2SO_4 LEVEL

The presence of alkali metal species has been reported in fuels derived from coal and biomass [127]. Early TBC failure was observed in the presence of deposits containing a minor amount of K_2SO_4. Based on the results presented in chapters 5 and 6, the addition of K_2SO_4 should result in liquid formation at 1100°C, either as a result of the sulfate melting in its pure state or as a low-melting silicate formed by reaction with SiO_2. In both cases, a liquid infiltration involving K_2SO_4 could damage the YSZ top coat in the TBC at 1100°C. The amount of available K_2SO_4 in the deposit should directly affect the amount of infiltration, and therefore the severity of TBC damage. The thermal cycles to failure summarized in Figure 80 show that increased levels of

K_2SO_4 resulted in decreased TBC lifetime for both types of deposit (rich in SiO_2 and CaO). The deposit compositions with varying K_2SO_4 concentrations are shown in Table 14. This suggests a direct link between available K_2SO_4 in the deposit and severity of damage produced in the TBC.

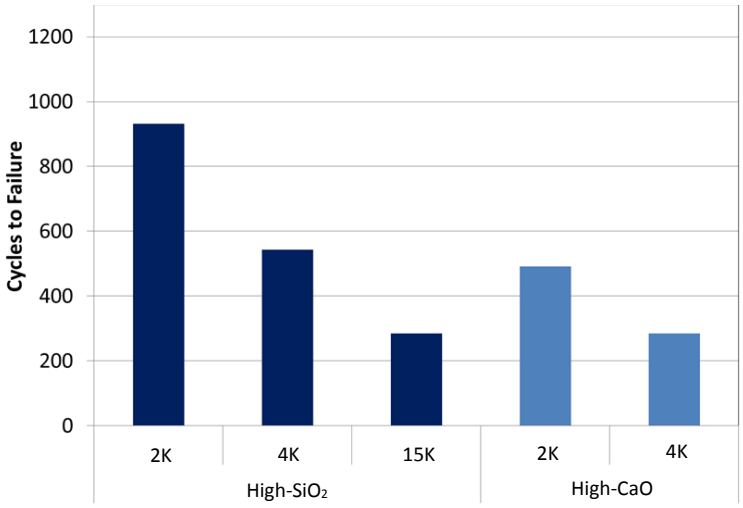

Figure 80: Cycles to failure are shown for SiO_2-rich deposits and CaO-rich deposits with varying levels of K_2SO_4 and FeS. Compositions of deposits are provided in Table 14. The same loading of 35 mg/cm^2 was applied in each case. Shortened lifetimes correspond to higher levels of K_2SO_4 addition to the deposits.

Table 14: Synthetic ash compositions (mol %) used to compare varying levels of K_2SO_4 and FeS on TBC lifetimes

Deposit		**K_2SO_4**	**FeS**	**CaO**	**SiO_2**	**Al_2O_3**	**MgO**	**Fe_2O_3**
SiO_2-Rich Deposit	2K	2	4	11	54	16	8	4
	4K	4		12	55.5	16.5	8	4
	15K	15	10	9	43	13	6	3
CaO-Rich Deposit	2K	2	4	70	17	5	1	1
	4K	4		72	17	5	1	1

11.2 EFFECTS OF ASH RE-DEPOSITION ON TBC LIFETIMES

The amount of liquid available for TBC degradation should also depend on the total amount of deposit applied to the sample during testing. TBC components in gas turbines may experience continuous deposition of fly ash. In some cases, fly ash could deposit on components after partial (or complete) top coat spallation. The added detrimental effects of multiple ash deposits on TBCs were therefore examined. HPLD TBCs were tested with high-SiO_2 synthetic ash with varying frequency of deposit application. The cycles to failure result of HPLD TBCs without deposit shown in Figure 81 is compared to failures from a single application of high-SiO_2 deposit before cycling. It is seen that the TBC lifetime was reduced even further by re-application of the deposit every 20 cycles during testing.

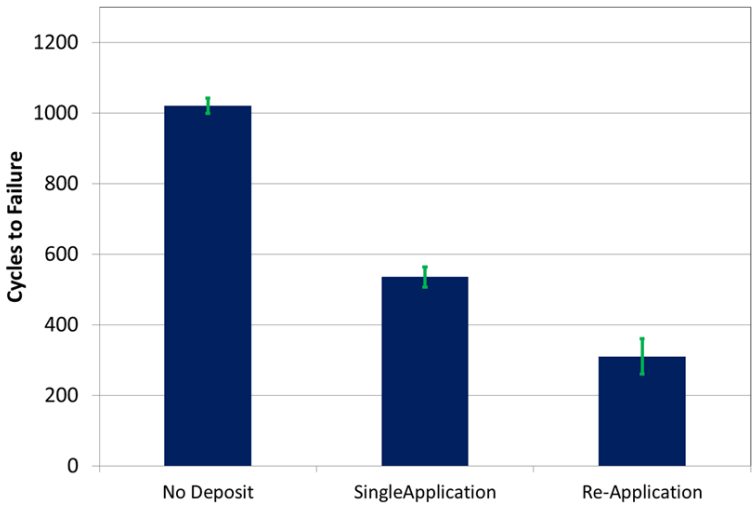

Figure 81: Effect of multiple applications of synthetic ash deposit on early cyclic failure. Cyclic failure without deposit is compared to that from a single application of deposit before cycling and re-application of deposit every 20 cycles during testing.

11.3 DISCUSSION OF EFFECTS OF EXPERIMENTAL VARIABLES

The TBC lifetime was directly affected by the amount of K_2SO_4 in the deposit, and an increased level of K_2SO_4 was shown to correlate with shorter lifetimes. This was the case for both the high-CaO deposit and the high-SiO_2 deposit. In both deposits, more K_2SO_4 would cause more liquid formation (and subsequent infiltration into the YSZ). Based on the result obtained, increased infiltration should cause more change in top coat stiffness, and shorter lifetimes.

The damage from high-SiO_2 and high-CaO deposits was directly compared with the same levels of K_2SO_4 and FeS. While both types of deposit were shown to damage TBC top coats, the high-CaO deposit was more detrimental to TBC lifetimes when minor constituents were kept the

same. This agrees with the results of chapter 0, which also showed that the internal $CaZrO_3$ formation from the high-CaO deposit was more detrimental to cyclic lifetime compared to the silicate infiltration from the high-SiO_2 deposit. Some comparisons in that section were made between the high-CaO and high-SiO_2 deposits which did not contain equivalent levels of K_2SO_4 and FeS. The data presented here adds clarification to those results, by showing that the level of K_2SO_4 in the deposit affects the failure times. The FeS was also not observed to react with any oxide constituents in the deposits. Furthermore, it was not identified to be involved in any liquid formation. Thus, varying levels of FeS in synthetic deposits did not appear to directly correlate to reduced TBC cyclic lifetimes.

The effects of ash re-deposition were shown with high-SiO_2 deposit. A dramatic decrease in TBC lifetime was experienced even with a single deposit before thermal cycling. Reapplications further reduced the lifetime, but the damage did not scale accordingly. The re-deposition of deposit every 20 cycles resulted in 15-20 deposits at the time of failure. The TBC lifetime, however, was only reduced by approximately a factor of two. This indicates that the bulk of the damage was done by the initial deposit. The re-deposition of high-CaO deposit would be expected to have less of an effect on lifetime reduction, because the $CaZrO_3$ surface layer would act as a barrier to further YSZ penetration (until spallation occurs.) Isothermal testing with free-standing YSZ verified that re-deposition of surface deposit did not measurably increase overall internal $CaZrO_3$ formation.

For the same level of K_2SO_4 addition to both (high-CaO and high-SiO_2) deposits, the high-CaO deposit resulted in shorter lifetimes. This showed that the overall damage from high-CaO was more aggressive compared to the high-SiO_2 deposit. However, the relative increase in K_2SO_4

corresponded to a similar shortening in TBC lifetime for both deposits. Figure 80 indicates that the lifetimes were approximately cut in half when the amount of K_2SO_4 was doubled. The fact that this same trend was observed for both types of deposits indicates that the cause of failure is essentially the same in both cases: increased stored strain energy in the top coat which results from a corresponding increase in elastic modulus. The effect is less severe for the high-SiO_2 deposit because the infiltrating product is a silicate which does not have as high an elastic modulus as the $CaZrO_3$ product which forms with the high-CaO deposit. However, in either case the importance of the level of K_2SO_4 in the deposit is clear. Increasing addition of K_2SO_4 (and corresponding increased liquid infiltration) corresponds to shorter TBC lifetimes.

12.0 CONCLUDING REMARKS

Gas turbine components which utilize TBCs for protection from hot gas atmospheres are susceptible to the accumulation of deposits. Representative deposits similar to those expected in IGCC systems were shown to severely degrade TBCs in laboratory cycling experiments. The reduced TBC lifetimes shown in this work indicate that both DVC and conventional HPLD TBCs can be damaged by deposits. One important observation in this study, however, is that the HPLD top coats were more severely affected by some deposit chemistries. Degradation of TBCs was attributed to increased stored strain energy in the YSZ top coat layer which resulted from infiltrating species form the deposit. The liquid infiltration, which occurred at 1100°C, damaged the top coat upon cooling.

Deposit-induced degradation studies of TBCs typically fall into one of two categories: hot corrosion from salts at temperatures around 700-900°C, or liquid infiltration from oxide deposits of CaO-MgO-Al_2O_3-SiO_2 (CMAS) at higher temperatures ≥1250°C. The failure shown in this study is significant because it represents a type of degradation which combines aspects of both, hot corrosion and CMAS damage, at a temperature which is typically not considered detrimental. At temperatures around 1100°C, the stability of the t'-YSZ combined with the absence of liquid

silicate formation from the CMAS deposit typically suggest the absence of significant degradation mechanisms.

Gas atmospheres containing steam and SO_2 (similar to what can be expected in IGCC systems) were used in cyclic TBC testing. While the steam did not produce measurable degradation of the TBC system, the presence of SO_2 did result in additional degradation near the TGO/bondcoat boundary. This additional effect caused some additional shortening of overall TBC lifetime. The additional damage, however, was not identified to be the primary cause of degradation. The primary cause of early failure was still attributed to the infiltration of deposit constituents into the YSZ; infiltration occurred in a dry air atmospheres as well as an SO_2-comtaining atmosphere. Therefore, the damage shown to occur in this work should contribute to early TBC failure at 1100°C regardless of atmosphere.

The TBC degradation identified in this work can be important in a wide range of deposits which can accumulate over long periods of time on components in land-based turbines which ingest large volumes of air. Trace amounts of sulfates and oxides similar to those studied here are commonly found in a variety of systems. The resulting TBC degradation shown in this work should be considered in many practical turbine systems.

13.0 SUGGESTED FUTURE WORK

The results presented in this study would be improved upon by additional laboratory testing. Future studies should include thermal gradient testing. The addition of a thermal gradient across the TBC system affects the overall cooling stresses as well as changing the compounds formed by reaction with the deposit. More testing should also be conducted in SO_2-containing atmospheres, and in particular with high-CaO deposits.

The reaction between CaO and the YSZ formed a continuous surface layer after a sufficient reaction time at 1100°C. This incubation period for continuous reaction layer formation could be studied further with additional exposure times during the incubation period (between 1h and 70h).

Further studies of deposits could benefit from more TEM characterization to identify phases at the reaction front, and also to further study the segregation of ash constituents in high-SiO_2 deposits at YSZ grain boundaries. Additionally, the deposits themselves could be characterized in more detail before reaction with the YSZ. The resources to accomplish this were not readily available for the current work, but could be included in future studies.

The wetting of the YSZ surface by molten K_2SO_4 should be studied further. Additional experiments should be conducted to observe the contact angle between the molten K_2SO_4 and

YSZ surface at 1100°C. This would add clarification to the extensive wetting of the YSZ which was observed in this study.

The observed diffusion of Ca^{2+} in K_2SO_4 was quite low. For the purpose of this work, the demonstration of minimal diffusion of Ca^{2+} into liquid K_2SO_4 served as evidence that the vehicle by which Ca entered the YSZ was primarily fast dissolution of Ca^{2+} which entered the cracks initially during wetting by molten K_2SO_4. The value of the diffusion coefficient, D, however was not accurately determined in this study. A more accurate determination of D would be necessary to further develop this mechanism of infiltration.

REFERENCES

[1] Pint BA. Jom 2013;65:1024.

[2] Administration USEI. Annual Energy Outlook 2016. 2016. p.256.

[3] Administration USE. Annual Energy Outlook 2016 Early Release. 2016.

[4] Ratafia-Brown JA, Manfredo LM, Hoffmann JW, Ramezan M, Stiegel GJ. An Environmental Assessment of IGCC Power Systems. Nineteenth Annual Pittsburgh Coal Conference 2002.

[5] Maurstad O. An Overview of Coal based Integrated Gasification Combined Cycle (IGCC) Technology. 2005.

[6] Padture NP, Gell M, Jordan EH. Science 2002;296:280.

[7] White BM, Ames RW, Burke P. Conditions in Advanced Turbines for IGCC Power Plants with Carbon Capture. ASME Turbo Expo. San Antonio, TX, 2013.

[8] Minchener AJ. Fuel 2005;84:2222.

[9] Bons JP, Crosby J, Wammack JE, Bentley BI, Fletcher TH. High Pressure Turbine Deposition in Land Based Gas Turbines From Various Synfuels. ASME Turbo Expo 2005: Power for Land, Sea and Air. Reno-Tahoe, Nevada, 2005.

[10] Brooker DD, Oh MS. Fuel Processing Technology 1995;44:181.

[11] Administration UEI. AEO 2014 Early Release Overview. 2014

[12] Hammond GP, Akwe SSO, Williams S. Energy 2011;36:975.

[13] Cormos C-C. Energy 2012;42:434.

[14] Jenkins S, G. B. A Comparison of PC, CFB, and IGCC Technologies for Basin Electric Power Cooperative's Dry Fork Station. 2007.

[15] Energy D. How IGCC Works. 2016.

[16] Jenkins BM, Baxter LL, Miles TR, Miles TR. Fuel Processing Technology 1998;54:17.

[17] Wang P, Massoudi M. Effect of Coal Properties and Operation Conditions on Flow Behavior on Coal Slag in Entrained Flow Gasifiers: A Brief Review. 2011.

[18] Wang P, Massoudi M. Energies 2013;6:784.

[19] Brooker D. Fuel 1993;72:665.

[20] Sims C, Stoloff N, Hagel W. Superaoolys II. New York: John Wiley and Sons, 1987.

[21] Clarke DR, Oechsner M, Padture NP. Mrs Bulletin 2012;37:891.

[22] Clarke DR, Levi CG. Ann. Rev. Mater. Res. 2003;33:383.

[23] Gleeson B. J. Propul. Power 2006;22:375.

[24] Darolia R. International Materials Reviews 2013;58:315.

[25] Evans AG, Mumm DR, Hutchinson JW, Meier GH, Pettit FS. Progress in Materials Science 2001;46:505.

[26] Taylor TA. Review of Thermally Sprayed Thermal Barrier Coatings. ASM International Surface Engineering Congress. Orlando, FL, 2004.

[27] Feuerstein A, Knapp J, Taylor T, Ashary A, Bolcavage A, Hitchman N. Journal of Thermal Spray Technology 2008;17:199.

[28] Chevalier J, Gremillard L, Virkar AV, Clarke DR. Journal of the American Ceramic Society 2009;92:1901.

[29] Reed R. The Superalloys: Fundamentals and Applications. Cambridge, 2006.

[30] Lipkin DM, Krogstad JA, Gao Y, Johnson CA, Nelson WA, Levi CG. Journal of the American Ceramic Society 2013;96:290.

[31] Krogstad JA, Krämer S, Lipkin DM, Johnson CA, Mitchell DRG, Cairney JM, Levi CG. Journal of the American Ceramic Society 2011;94:s168.

[32] Kramer S, Yang J, Levi CG, Johnson CA. Journal of the American Ceramic Society 2006;89:3167.

[33] Hannink RHJ, Kelly PM, Muddle BC. Journal of the American Ceramic Society 2000;83:461.

[34] Virkar AV, Matsumoto RLK. Journal of the American Ceramic Society 1986;69:C.

[35] Jones RL. Journal of Thermal Spray Technology 1997;6:77.

[36] Vasiliev AL, Padture NP. Acta Materialia 2006;54:4913.

[37] Vasiliev AL, Padture NP. Acta Materialia 2006;54:4921.

[38] Aygun A, Vasiliev AL, Padture NP, Ma X. Acta Materialia 2007;55:6734.

[39] Rabiei A, Evans AG. Acta Materialia 2000;48:3963.

[40] Peters M, Leyens C, Schulz U, Kaysser WA. Advanced Engineering Materials 2001;3:193.

[41] Fleck NA, Zisis T. Wear 2010;268:1214.

[42] Wellman RG, Nicholls JR. Tribology International 2008;41:657.

[43] Mohan P, Patterson T, Sohn YH, Desai VH. Degradation of Thermal Barrier Coatings by Molten CMAS (CaO-MgO-Al2O3-SiO2) Deposits. 47th AIAA Aerospace Sciences Meeting Including the New Horizons Forums and Aerospace Exposition. Orlando, FL, 2009.

[44] Evans AG, Clarke DR, Levi CG. Journal of the European Ceramic Society 2008;28:1405.

[45] Levi CG, Hutchinson JW, Vidal-Setif M-H, Johnson CA. Mrs Bulletin 2012;37:932.

[46] Wellman R, Whitman G, Nicholls JR. International Journal of Refractory Metals & Hard Materials 2010;28:124.

[47] He MY, Hutchinson JW, Evans AG. Materials Science and Engineering a-Structural Materials Properties Microstructure and Processing 2003;345:172.

[48] Birks N, Meier GH, Pettit FS. Introduction to the High-Temperature Oxidation of Metals: Cambridge University Press, 2006.

[49] Choi SR, Hutchinson JW, Evans AG. Mechanics of Materials 1999;31:431.

[50] Helminiak M. Failure of Thick, Low Density Air Plasma Sprayed Thermal Barrier Coatings. Mechanical Engineering and Materials Science, vol. Doctorate of Philosophy: University of Pittsburgh, 2013. p.274.

[51] Kraemer S, Faulhaber S, Chambers M, Clarke DR, Levi CG, Hutchinson JW, Evans AG. Materials Science and Engineering a-Structural Materials Properties Microstructure and Processing 2008;490:26.

[52] Evans HE, Taylor MP. Oxidation of Metals 2001;55:17.

[53] Yanar NM, Pettit FS, Meier GH. Metallurgical and Materials Transactions a-Physical Metallurgy and Materials Science 2006;37A:1563.

[54] Deneux V, Cadoret Y, Hervier S, Monceau D. Oxidation of Metals 2010;73:83.

[55] Smialek JL, Zhu D, Cuy MD. Scripta Materialia 2008;59:67.

[56] Rudolphi M, Renusch D, Zschau HE, Schuetze M. Materials at High Temperatures 2009;26:325.

[57] Smialek JL. Jom 2006;58:29.

[58] Smialek JL. Surface and Coatings Technology 2011;206:1577.

[59] Maris-Sida MC, Meier GH, Pettit FS. Metallurgical and Materials Transactions a-Physical Metallurgy and Materials Science 2003;34A:2609.

[60] Janakiraman R, Meier GH, Pettit FS. Metallurgical and Materials Transactions a-Physical Metallurgy and Materials Science 1999;30:2905.

[61] Guo X. Journal of Physics and Chemistry of Solids 1999;60:539.

[62] Guo X. Solid State Ionics 1998;112:113.

[63] Leyens C, Wright IG, Pint BA. Oxidation of Metals 2000;54:401.

[64] Mercer C, Faulhaber S, Evans AG, Darolia R. Acta Materialia 2005;53:1029.

[65] Mohan P, Patterson T, Yao B, Sohn Y. Journal of Thermal Spray Technology 2010;19:156.

[66] Gledhill AD, Reddy KM, Drexler JM, Shinoda K, Sampath S, Padture NP. Materials Science and Engineering a-Structural Materials Properties Microstructure and Processing 2011;528:7214.

[67] Grant KM, Kraemer S, Seward GGE, Levi CG. Journal of the American Ceramic Society 2010;93:3504.

[68] Kamal S, Jayaganthan R, Prakash S. ASM International 2010;20:1068.

[69] Batista C, Portinha A, Ribeiro RM, Teixeira V, Oliveira CR. Surface & Coatings Technology 2006;200:6783.

[70] Yoshiba M, Abe K, Aranami T, Harada Y. Journal of Thermal Spray Technology 1996;5:259.

[71] Loghman-Estarki MR, Nejati M, Edris H, Razavi RS, Jamali H, Pakseresht AH. Journal of the European Ceramic Society 2015;35:693.

[72] Park SY, Kim JH, Kim MC, Song HS, Park CG. Surface & Coatings Technology 2005;190:357.

[73] Gurrappa I. Journal of Materials Science Letters 1998;17:1267.

[74] Jones RL, Williams CE. Surface and Coatings Technology 1987;32:349.

[75] Barkalow RH, Pettit FS. Mechanisms of Hot Corrosion Attack of Ceramic Coating Materials. 1st Conf. Advanced Materials for Alternative Fuel Capable Directly Fired Heat Engines: J.W. Fairbanks and J. Stringer, 1979. p.704.

[76] Nagelberg AS. Journal of the Electrochemical Society 1985;132:2502.

[77] Huang H, Liu C, Ni L, Zhou C. Corrosion Science 2011;53:1369.

[78] Lee CH, Kim HK, Choi HS, Ahn HS. Surface & Coatings Technology 2000;124:1.

[79] Li L, Hitchman N, Knapp J. Journal of Thermal Spray Technology 2010;19:148.

[80] Chen X. Surface and Coatings Technology 2006;200:3418.

[81] Wu J, Guo H-b, Gao Y-z, Gong S-k. Journal of the European Ceramic Society 2011;31:1881.

[82] al Le. Phase Diagrams for Ceramists, 1964.

[83] Eriksson G, Pelton AD. Metallurgical Transactions B-Process Metallurgy 1993;24:807.

[84] Hallstedt B. Journal of the American Ceramic Society 1992;75:1497.

[85] Aramaki S, Roy R. Journal of the American Ceramic Society 1962;45:229.

[86] Drexler JM, Shinoda K, Ortiz AL, Li D, Vasiliev AL, Gledhill AD, Sampath S, Padture NP. Acta Materialia 2010;58:6835.

[87] Krause AR, Senturk BS, Garces HF, Dwivedi G, Ortiz AL, Sampath S, Padture NP. Journal of the American Ceramic Society 2014;97:3943.

[88] Beckett JR. Geochimica et Cosmochimica Acta 2002;66:93.

[89] Duffy JA. Geochimica et Cosmochimica Acta 1993;57:3961.

[90] Braue W, Mechnich P, Peters PWM. Materials at High Temperatures 2011;28:315.

[91] Braue W, Mechnich P. Journal of the American Ceramic Society 2011;94:4483.

[92] Braue W. Journal of Materials Science 2009;44:1664.

[93] Mechnich P, Braue W. Journal of the American Ceramic Society 2015;98:296.

[94] Bons JP, Crosby J, Wammack JE, Bentley BI, Fletcher TH. Journal of Engineering for Gas Turbines and Power-Transactions of the Asme 2007;129:135.

[95] Borom MP, Johnson CA, Peluso LA. Surface and Coatings Technology 1996;86–87, Part 1:116.

[96] Font O, Querol X, Izquierdo M, Alvarez E, Moreno N, Diez S, Alvarez-Rodriguez R, Clemente-Jul C, Coca P, Garcia-Pena F. Fuel 2010;89:3250.

[97] Font O, Querol X, Huggins FE, Chimenos JM, Fernandez AI, Burgos S, Pena FG. Fuel 2005;84:1364.

[98] Gledhill AD, Reddy KM, Drexler JM, Shinoda K, Sampath S. Materials Science and Engineering A 2011;528:7214.

[99] Helminiak MA, Yanar NM, Pettit FS, Taylor TA, Meier GH. Surface & Coatings Technology 2009;204:793.

[100] Vaßen R, Czech N, Malléner W, Stamm W, Stöver D. Surface and Coatings Technology 2001;141:135.

[101] Jackson RW, Zaleski EM, Poerschke DL, Hazel BT, Begley MR, Levi CG. Acta Materialia 2015;89:396.

[102] Grant KM, Kramer S, Lofvander JPA, Levi CG. Surface & Coatings Technology 2007;202:653.

[103] Van Dyk JC, Benson SA, Laumb ML, Waanders B. Fuel 2009;88:1057.

[104] Barin I. Thermochemical data of pure substances. Weinheim, Federal Republic of Germany;New York;: VCH, 1993.

[105] Pliegocuervo YB, Glasser FP. Cement and Concrete Research 1977;7:477.

[106] Murday JS, Cotts RM. The Journal of Chemical Physics 1968;48:4938.

[107] Eliezer I, Howald RA. Journal of Chemical Physics 1976;65:3053.

[108] Armatys K, Miller M, Matraszek A, Wolter A. Materials Science-Poland 2011;29:77.

[109] Zaleski EM, Ensslen C, Levi CG. Journal of the American Ceramic Society 2015;98:1642.

[110] Tsoga A, Nikolopoulos P. Journal of Materials Science 1996;31:5409.

[111] Janz GJ. Journal of Physical and Chemical Reference Data 1988;17.

[112] Chapter 4 Surface energies. In: Nicolas Eustathopoulus MGN, Béatrice D, editors. Pergamon Materials Series, vol. Volume 3. Pergamon, 1999. p.148.

[113] Chapter 1 Fundamental equations of wetting. In: Nicolas Eustathopoulus MGN, Béatrice D, editors. Pergamon Materials Series, vol. Volume 3. Pergamon, 1999. p.1.

[114] Jackowski J, Suchora-Kozakiewicz M. Assessment Of Usability Of Molten Salt Mixtures In Metallurgy Of Aluminum Alloys And Recycling Of Composite Materials Based On The Matrix Of Al Alloys. Archives of Metallurgy and Materials, vol. 60, 2015. p.1731.

[115] Freudig B, Hogekamp S, Schubert H. Chemical Engineering and Processing: Process Intensification 1999;38:525.

[116] Wu, Eriksson, Pelton. Journal of the American Ceramic Society 1993;76:2059.

[117] Aoki M, Chiang Y-M, Kosacki I, Lee LJ-R, Tuller H, Liu Y. Journal of the American Ceramic Society 1996;79:1169.

[118] K. B, G. L. American Mineralogist 1989;74:224.

[119] Levin EM, Robbins CR, McMurdie HF. Phase Diagrams for Ceramists. Columbus, OH: The American Ceramic Society, 1964.

[120] Martin MC, Mecartney ML. Solid State Ionics 2003;161:67.

[121] Yang H, Ohishi Y, Kurosaki K, Muta H, Yamanaka S. Journal of Alloys and Compounds 2010;504:201.

[122] Nadler MR, Fitzsimmons ES. Journal of the American Ceramic Society 1955;38:214.

[123] Ramachandran CS, Balasubramanian V, Ananthapadmanabhan PV. Vacuum 2013;97:81.

[124] Gheno T, Gleeson B. Oxidation of Metals 2015;84:567.

[125] Rapp RA, Otsuka N. ECS Transactions 2009;16:271.

[126] Chevalier J, Gremillard L, Deville S. Low-temperature degradation of Zirconia and implications for biomedical implants. Annual Review of Materials Research, vol. 37. 2007. p.1.

[127] Knudsen JN, Jensen PA, Lin W, Frandsen FJ, Dam-Johansen K. Energy & Fuels 2004;18:810.